Complex Systems for Quantum Technologies

Sibylle Braungardt

Universitat Politècnica de Catalunya

Institut de Ciències Fotòniques

Chapter 1

Introduction

This thesis summarizes my work on complex systems for quantum technologies at the Quantum Optics Theory group at ICFO. It contains the results published in the references [Braungardt et al., 2011b, Braungardt et al., 2011a, Braungardt et al., 2008,Braungardt et al., 2007,Pons et al., 2007] along with some unpublished results. This chapter introduces the general context and summarizes our main results.

1.1 General Context

Historically, the great majority of computers are based on the von Neumann architecture, in which explicit instructions are processed one at a time. However, alternative computing paradigms, more suitable to tackle certain classes of problems, are receiving increasing attention.

One alternative approach to computation has evolved from efforts to model the storage and processing of information in biological systems and resulted in artificial neural network science. In a neural network, the information is encoded in the stable states of a complex system, composed of a large number of simple interacting units. Complex systems typically exhibit properties that emerge from the interactions of the units, and that are not inherent to the individual components themselves. In neural networks, a typical way to attain robustness to noise in the manipulation of data is to store the information in a distributed way in

the stable states of the system. Neural networks have been shown to be capable of recognizing even distorted patterns and process information with a high level of noise.

Another novel approach to information processing is quantum computation, which makes use of quantum superpositions and entanglement of states to improve the computing efficiency in certain classes of problems. The implementation of a quantum computer requires a controlled engineering of the quantum states involved. In particular, the preparation, manipulation and detection of the states have to be achieved with high fidelity. Despite the great achievements that have been made towards experimental realization of a quantum computer, one of the major challenges is the noise management in the devices.

The aim of this thesis is to explore the possibility of using some of the features of classical neural networks to attain a higher level of noise resistance for the storage and processing of quantum information. Inspired by classical neural networks, where the existence of stable states that behave as attractors is essential, we study quantum mechanical many-body systems with long range interactions, which typically can have many stable (or metastable) states.

The first part of the thesis presents our proposal for an implementation of a neural-network-like system for quantum information processing realized in a chain of trapped ions. Trapped ions are highly controllable quantum systems, where individual ions can be addressed by laser fields. Long range interactions can be achieved through the coupling of the ions via the vibrational modes of the trap. In principle, the implementation of distributed quantum information in an ion trap allows for the preparation and manipulation of quantum information with high error resistance. However, to date, the system's size is limited to relatively small numbers of ions, and decoherence is a major problem.

Optical lattices, in contrast, allow to build up very large systems with relatively long decoherence times. It has been theoretically predicted, that a rich energy landscape with a large number of metastable states can be achieved with dipolar atoms or molecules in optical lattices. Despite the great progress that is being made, the experimental control of the long-range interactions and the detection of the states is still challenging. Any application based on complex quantum systems realized in optical lattices requires a high fidelity read-out of the state of the system.

The second part of the thesis focuses on the detection of various many-body quantum systems, that could be used for distributed quantum information processing, by analyzing their counting distributions. We are particularly interested in studying the detection of complex quantum many-body systems with metastable states as well as systems that exhibit emergent behavior like phase transitions, which can involve entanglement at the many-particle level. In quantum optics, photon counting is of major importance for the detection of different quantum states of light. Analogously, atom counting provides insight into the quantum properties of systems of ultracold atoms.

1.2 Main Results

Chapter 3, presents our proposal [Pons et al., 2007, Braungardt et al., 2007] for an implementation of a device for distributed processing of classical and quantum information in a chain of trapped ions. The distributed information encoding leads to a high robustness against noise. We conclude that:

- Quantum states can be prepared and manipulated with high fidelity.
- A universal set of quantum gates can be implemented through adiabatic passage of external fields.
- The system is resistant to errors, both local and global ones.

In **Chapter 4**, we review the theory of photon- and atom-counting and extend it to time- and space dependent fields. The quantum theory of photon counting was initiated with the Glauber-Mandel formula, which gives a full quantum description of the interaction between the incoming light and the detector for short detection times. Longer detection times are treated perturbatively, such that the absorption at the detector in one time interval does not depend on the previous ones. For a single-mode field, a formula that does include the backaction of the detector on the field has been derived. We discuss the validity and limits of the existing approaches of particle counting for given experimental setups. We conclude that experimental situations with time- and space-dependence, in general, cannot be treated within the existing formalism. We present a derivation of a formula for the counting distribution for time-dependent systems that are

registered at spatially confined detectors. Our derivation is based on the master equation that models the interaction between the system and the detector, and includes the effects of absorption of particles during detection. Our main results are the following.

- We derive a formula which is formally equivalent to the Glauber-Mandel formula, where the intensity is written in terms of modified field operators that include the absorption at the detector.
- The modified field operators follow the Schrödinger equation with an imaginary potential.
- In the limit where the dynamics of the system are slow compared to the detection process, the formalism simplifies and reduces to the formalism discussed in the literature.

Chapter 5 contains our work in [Braungardt et al., 2008] and [Braungardt et al., 2011a], where we illustrate the power of the method of particle counting by studying a paradigmatic model of a system of strongly correlated fermions that exhibits rich behavior such as a quantum phase transition and fermion pair formation. The system is equivalent to the anisotropic quantum XY-model via the Jordan Wigner transform. We show that the many-body features of the system can be characterized by particle counting. We address the issue of thermal noise by considering the system in thermal equilibrium at different temperatures. This is of fundamental importance, as quantum phase transitions are defined only at zero temperature, whereas in real experimental situations effects of temperature are unavoidable. We study the traces of the quantum effects that are visible at finite temperature. Furthermore, we analyze the thermalization of the system when coupled to a heat bath. Here, the dynamics are much slower that the detection, such it is not necessary to use the full time-dependent formula. Our main results are:

- The quantum phase transition of the model is clearly visible in the first cumulants of the counting distribution.
- For high detection efficiencies, the formation of fermionic pairs is reflected in the full counting distribution. For lower efficiencies it is no longer visible.

- The overall behavior of the system does not depend strongly on the anisotropy parameter. This is expected as the systems are in the Ising universitality class.

- The signatures of the quantum crossover are visible in the cumulants of the counting distribution for low temperatures and disappear as the temperature is of the order of the system energies.

- The breaking of fermionic pairs by thermal noise is reflected in the counting distribution. The temperature at which the pairs are broken is proportional to the binding energy.

- The thermalization of the system due to an exchange of quasi-particle excitations with a heat bath can be monitored through particle counting.

- The coupling of the quasi-particle excitations in the thermalization is non-local. We show that the non-local coupling translates to a local coupling of the particles of the system.

Chapter 6, exposes our findings in [Braungardt et al., 2011b], where we study the counting statistics of a system of atoms that are released from an optical lattice and fall in the gravitational field. We analyze the effect of the expansion of the atoms on the counting statistics. As the particles expand, the initial modes interfere and the correlations are, in principle, accessible by particle counting. We consider a momentary detection process, in which the dynamics of the system are slow compared to the detector opening time. This formalism is valid for most experimental situations. We find that:

- The Mott insulator phase is distinguished from the superfluid phase in the counting distribution of the expanded atoms.

- In the Mott phase, the counting events at two detectors are correlated. As the distance between the two detectors increases, the correlations are no longer visible.

- For appropriately chosen detector geometries, the correlations between different sites can be inferred from the counting distribution after the expansion. In principle, this allows for distinguishing different metastable states

within the insulating regime. In order to use such states for distributed quantum information processing, the detection is essential.

Chapter 7 illustrates the effect of the absorption at the detector for the detection of an expanding Bose-Einstein condensate (BEC). Here, the timescale of the system dynamics and the counting process coincide. We thus apply the full time- and space- dependent formalism derived in Chapter 4. Furthermore, we consider a solution obtained through the Born approximation, which includes the backaction of the detector on the field up to second order. We compare our formalism to the second-order approximation and the Glauber-Mandel formula and discuss the limits of the two approaches. In summary:

- Our formalism correctly describes the situation even for long detection times, whereas the Glauber-Mandel formula is limited to short detection times.
- The Born approximation gives valid results for low detector efficiencies. For high efficiencies, both for the Born approximation and for the Glauber-Mandel formula, the particle number is overestimated.

Chapter 2

Background

The field of Quantum information has attracted much attention in the last decades, and remarkable experimental advances towards the implementation of a quantum computer have been achieved. However, whereas the control of systems of a small number of qubits has been demonstrated, the scalability to larger systems is challenging. In this context, one of the main challenges is the susceptibility of quantum states to errors.

Complex systems, in particular neural network models, play an important role for the processing of classical information. The network consists of a large number of interconnected neurons. In neural networks, the information processing takes place on the level of the whole network. A high level of error resistance is achieved by storing the information distributed over all nodes.

The goal of our work is to transfer some of the features that lead to robustness in classical neural networks to quantum systems. We therefore study complex quantum systems consisting of strongly correlated quantum particles. We consider two main approaches to the realization of such systems: 1) Ions in a trap, where long range interactions are mediated by the vibrational modes. 2) Atoms or molecules in optical lattices, where long range interactions can be achieved through dipole-dipole interactions. In Fig. 2.1, we illustrate the analogy between the systems.

In order to implement a quantum computing device, it is essential to prepare, manipulate and detect the quantum information in the system. In Sect. 2.1, we

recall some basic facts about quantum computation. In Sect. 2.2, we shortly review the Hopfield neural network model and discuss some of the emergent global properties of classical neural networks and their use for the processing and storage of classical information. Sect. 2.3 deals with the possible physical systems that could be used to implement some of the advantageous features of complex systems for the manipulation of quantum information. In particular, we consider systems with long-range interactions implemented in trapped ions and bosons, fermions and spins in optical lattices. In Sect. 2.4, we review methods for the detection of strongly correlated atomic systems.

2.1 Quantum Information Processing

The idea behind the quantum computer is to design a computational device based on quantum mechanics. It is somewhat natural to wonder about the role of quantum physics in computation, as the size of circuitry placed on computer chips rapidly decreases. Once the size of individual elements reach a certain critical level, their behavior and properties are no longer governed by classical physics, but rather by quantum mechanics. Another motivation was put forward by Richard P. Feynman [Feynman, 1982], who was among the first to explore the idea of computation based on quantum mechanics. He observed that the only way to effectively model a quantum mechanical system would be by using another quantum mechanical system. Since then, quantum simulators have been studied with great success both theoretically and experimentally and may become a reality in the near future, for a review see [Lewenstein et al., 2007, Buluta and Nori, 2009].

The first quantum algorithm, that outperforms any classical computational device for a given task, was devised by Deutsch [Deutsch, 1985] and generalized in [Deutsch and Jozsa, 1992]. The major breakthrough of quantum computation was Peter Shor's discovery of a quantum algorithm for factoring large integers into its prime factors [Shor, 1997]. The algorithm is significant, because most cryptography schemes rely on the difficulty of finding the prime factors of large numbers. On classical computers, the time of factorization increases exponentially as the number grows large. In contrast, Shor's algorithm can factor numbers, and thus crack the cryptography system, in polynomial time. Another quantum algorithm

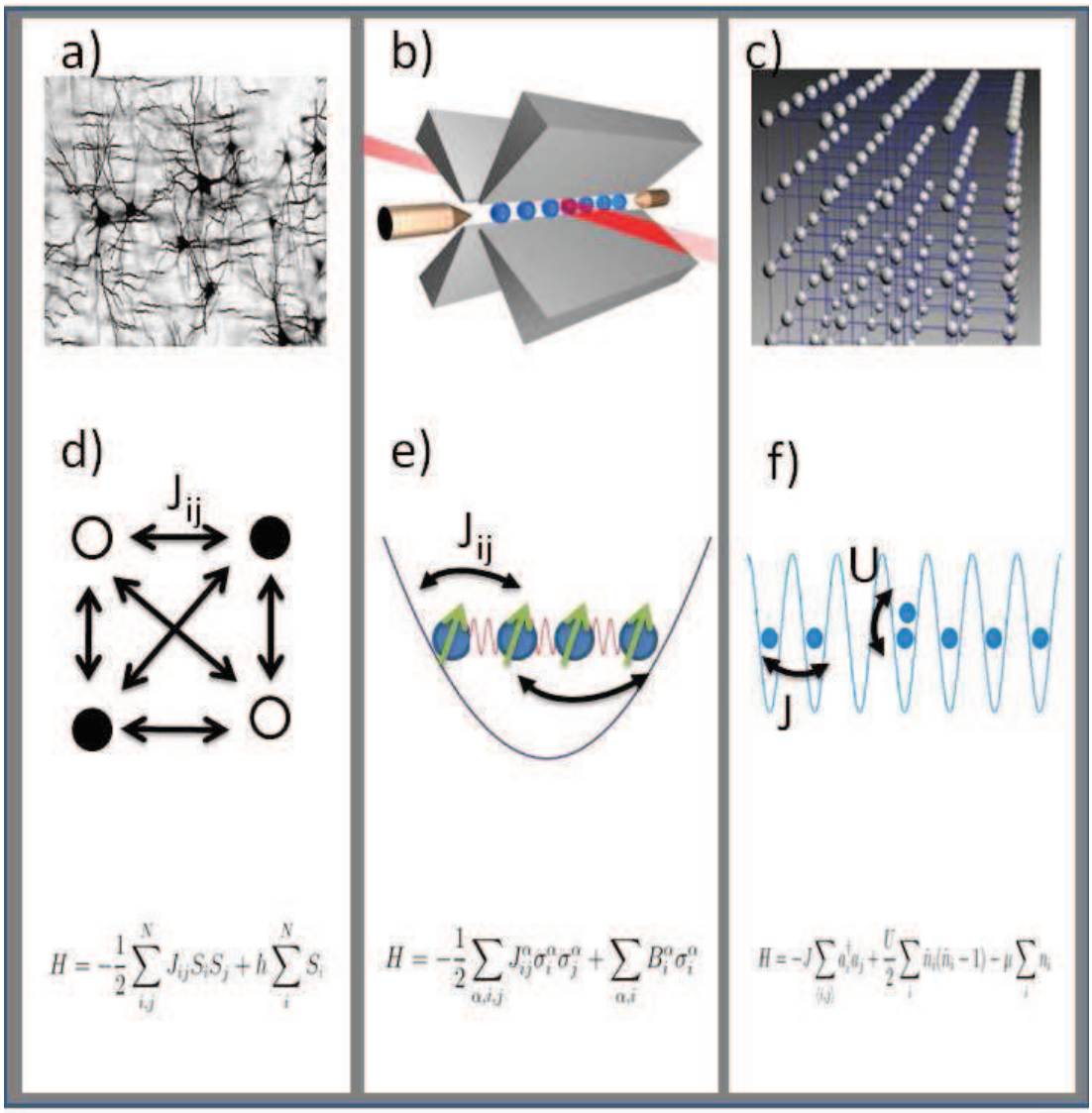

Figure 2.1: We explore the possibility of exploiting some characteristics of classical neural networks for quantum information tasks in complex quantum systems. Therefore, we compare the system properties of a simple model of a neural network (first column) to a chain of trapped ions with long range interactions (second column) and atoms in optical lattices (third column). Fig. a)-c) show the respective physical implementations. Fig. d) depicts a toy model of four neurons, which are connected by the synaptic efficacies J_{ij}. Fig. e) displays a schematic view of ions in a trap, which realize an effective spin-model with long-range interactions mediated by the vibrational modes of the string of ions. Fig. f) illustrates a system of atoms in an optical lattice, where the interactions are determined by the hopping J of particles between neighboring sites and the on-site interactions U. The respective Hamiltonians are depicted in the lower part of the figure. Source: Fig. b): R. Blatt group. Fig. c): I. Bloch group

with potential applications was invented by Lov Grover in 1996 [Grover, 1997]. Grover's algorithm searches an unsorted database with quadratic speed up with respect to any classical method.

In this section, we briefly review some of the characteristics of quantum information processing and highlight the differences to classical computation. In Sect. 2.1.1, we consider the qubit as the basic unit of quantum information. Following the rules of quantum mechanics, the qubit manipulation is achieved through quantum gates that are composed of unitary operations. In Sect. 2.1.2, we review a set of one- and two-qubit gates that allow for universal quantum computing. As opposed to classical computation, one of the main challenges in quantum computation are errors. In Sect. 2.1.3, we resume the main differences between classical and quantum error correction.

2.1.1 The Qubit

The indivisible unit of classical information is the *bit*: an object that can take either one of two values: 0 or 1. The corresponding unit of quantum information is the quantum bit or *qubit* represented by any two level quantum system. One of the differences between bits and qubits is that a qubit can be in a *superposition* of states, i.e. a linear combination $|\Psi\rangle = \alpha\,|0\rangle + \beta\,|1\rangle$, where α and β are complex numbers with $|\alpha|^2 + |\beta|^2 = 1$.

Another difference between classical and quantum bits is related to the *readout* of information. For a classical bit, we can determine if it is in the state 0 or 1 from just a single copy. However, even for a pure quantum state $\alpha\,|0\rangle + \beta\,|1\rangle$, the values of α and β cannot be determined if only a single copy is available. Quantum mechanics only allows for acquiring much more restricted information: When measuring a qubit in the computational basis $\{|0\rangle, |1\rangle\}$, one gets either the result $|0\rangle$, with probability $|\alpha|^2$, or the result $|1\rangle$, with probability $|\beta|^2$.

In classical computation, a two bit system can have four possible states, 00, 01, 10 and 11. Correspondingly, a two qubit system has four computational basis states $|00\rangle$, $|01\rangle$, $|10\rangle$ and $|11\rangle$. The state of the two qubit system is given by a superposition of these four states, $|\Psi\rangle = \alpha_{00}\,|00\rangle + \alpha_{01}\,|01\rangle + \alpha_{10}\,|10\rangle + \alpha_{11}\,|11\rangle$ with $|\alpha_{00}|^2 + |\alpha_{01}|^2 + |\alpha_{10}|^2 + |\alpha_{11}|^2 = 1$. Similar to the case for a single qubit, the measurement result $|xy\rangle$ occurs with probability $|\alpha_{xy}|^2$, where x, y can take

the values 0 or 1.

Experimentally, a qubit is realized by a two-level quantum system, such as the two spin states of an electron, two perpendicular polarizations of a photon or two different energy levels of an atom. In our work, we consider systems of trapped ions and atoms in optical lattices. In trapped ions, qubits are commonly realized either using two hyperfine or Zeeman sublevels in the electronic ground state, or a ground state and an excited level. For neutral atoms in optical lattices, the qubit can be realized in two hyperfine states of the atoms.

2.1.2 Quantum Gates

In classical computers, the information is manipulated through logic gates. Similarly, in most schemes for quantum information processing, the manipulation of information is performed by quantum gates, which are realized by unitary transformations. As in classical information, all qubit operations can be composed of one-qubit and two-qubit gates. In the following, we recall the most important examples of classical and quantum gates.

The only non-trivial example of a classical single bit gate is the NOT gate, which takes $0 \rightarrow 1$ and $1 \rightarrow 0$. Its quantum counterpart clearly takes $|0\rangle \rightarrow |1\rangle$ and $|1\rangle \rightarrow |0\rangle$. There are, however, two important differences between classical and quantum single qubit gates:

Firstly, quantum gates can not only operate on the basis states $|0\rangle$ and $|1\rangle$ but also on superposition states $\alpha|0\rangle + \beta|1\rangle$. As the quantum mechanical evolution is linear, the quantum NOT gate acts linearly on the superposition state: $\alpha|0\rangle + \beta|1\rangle \rightarrow \alpha|1\rangle + \beta|0\rangle$.

Secondly, the NOT gate is not the only that gate can be constructed. Any unitary matrix specifies a valid quantum gate.

An important example for such a single qubit gate is the Hadamard gate, which maps the qubit-basis states $|0\rangle$ and $|1\rangle$ to two superposition states, with equal weight:

$$|0\rangle \rightarrow |+\rangle \equiv \frac{|0\rangle + |1\rangle}{\sqrt{2}}, \quad |1\rangle \rightarrow |-\rangle \equiv \frac{|0\rangle - |1\rangle}{\sqrt{2}}.. \tag{2.1}$$

Many quantum algorithms use the Hadamard transform as an initial step, since

it maps N qubits initialized to $|0\rangle$ to a superposition of all 2^N orthogonal states that can be formed by combinations of $|0\rangle$, $|1\rangle$, with equal weight. The resulting state allows the parallel manipulation of all the superposed states. This so called quantum parallelism is vital for almost all quantum algorithms.

Let us now focus on two qubit gates, i.e. gates that act on two input states. In classical computation, the AND, OR and XOR gates are examples of two bit logical gates. In the classical case, the two-bit gates take two input bits and produce one output bit. Any function on bits can be obtained from the composition of the NOT gate and the AND gate: the gates form a universal set of classical gates.

For the two qubit gates, the generalization to the quantum case is not quite as straightforward as for the case of the NOT gate. The reason is that unitary quantum gates are *always* reversible, since the inverse of a unitary matrix is also a unitary matrix, and thus any quantum gate can always be inverted by another quantum gate. The classical gates, on the other hand, are *not* reversible. An example for a quantum two qubit gate is the CNOT gate that takes one of the input qubits as a control qubit and the other one as a target qubit. If the value of the control qubit is 0, the target qubit is not changed. If the control qubit is set to 1, the target qubit is flipped: $|00\rangle \rightarrow |00\rangle\,; |01\rangle \rightarrow |01\rangle\,; |10\rangle \rightarrow |11\rangle\,; |11\rangle \rightarrow |10\rangle$.

In Chapter 3, we will consider another example of a two qubit gate: the so called Bell gate, which acts as

$$\begin{aligned} |00\rangle \rightarrow \frac{|00\rangle + |11\rangle}{\sqrt{2}}, \quad |11\rangle \rightarrow -\frac{|00\rangle - |11\rangle}{\sqrt{2}}, \\ |01\rangle \rightarrow \frac{|01\rangle + |10\rangle}{\sqrt{2}}, \quad |10\rangle \rightarrow -\frac{|01\rangle - |10\rangle}{\sqrt{2}}. \end{aligned} \tag{2.2}$$

A universal set of quantum gates can be constructed from a two qubit gate, such as the CNOT gate or the Bell gate, along with single qubit gates [Deutsch et al., 1995, DiVincenzo, 1995]. Any multiple qubit logic gate may be realized by combinations of these gates.

2.1.3 Quantum Memory and Error Correction

For classical information, storing devices such as CDs are susceptible to bit flip errors. That means that single bits of information can change their value. A

simple error correction scheme to protect the information is given by redundant information encoding, for example $0 \rightarrow 000$ and $1 \rightarrow 111$. If one bit is flipped, this can clearly be detected when looking at the three bits, and the erroneous bit can be flipped back. Encoding the information in more than three copies saves the information from more than one bit flips.

In the context of error resistance, the no-cloning theorem [Wootters and Zurek, 1982] implicates an important difference between classical and quantum computation. Whereas in classical computation the information can easily be copied, it is impossible to generate a copy of an unknown quantum state. The no-cloning theorem is of fundamental importance for the robustness to errors both in the storage and the processing of quantum information.

We illustrate the main differences between the treatment of errors in classical and quantum computation using the simple (and by far not the most efficient) example of classical error correction mentioned above.

- Classical error correction uses copies of the bit for redundant encoding. In contrast, quantum information cannot be copied (no cloning theorem)

- Even if quantum information could be redundantly encoded, measuring a quantum state causes its disturbance. A simple classical error correction scheme measures the bits in the code to detect and correct the errors, which is not possible for qubits.

- Quantum information has more possibilities to become faulty than classical information. In addition to bit flip errors described above, which in the quantum case are given by $|0\rangle \rightarrow |1\rangle \quad |1\rangle \rightarrow |0\rangle$, there can also be phase errors, $|0\rangle \rightarrow |0\rangle \quad |1\rangle \rightarrow -|1\rangle$, which have serious impacts on the information, as they can transform a state $\frac{1}{\sqrt{2}}[|0\rangle + |1\rangle]$ to the orthogonal state $\frac{1}{\sqrt{2}}[|0\rangle - |1\rangle]$.

- Quantum information evolves ideally by unitary transformation and is continuous. If a qubit is intended to be in the state $a|0\rangle + b|1\rangle$; an error might change a and b by an amount of order ε, and these small errors can accumulate over time. The classical method is only designed to correct large (bit flip) errors.

In order to achieve reliable results in quantum computing, tools to correct errors and to perform computation that can handle a certain level of errors are needed. Several approaches to quantum error correction and fault tolerant quantum computation have been proposed. There are two conceptually different approaches to confront the problem: additional error correction and intrinsic noise resistance.

The first approach includes protocols for quantum error correction [Shor, 1995], [Steane, 1996]. They are somewhat similar to the classical case in that the error correction is performed by additional operations. Fault tolerant quantum computation has been introduced by Peter Shor [Shor, 1996]; a review is given in [Gottesman, 1997]. The protocols make reliable quantum information processing possible *in principle*. Yet, depending on the complexity of the calculation, a huge overhead of computation time and resources arises.

The second approach relies on an *intrinsic* resistance to errors inherent to the physical hardware. As an example, Kitaev proposed a model for fault-tolerant quantum computation using topological features [Kitaev, 1997]. In Chapter 3, we propose an implementation of a universal set of quantum gates in a trapped ion chain. In our approach, a high resistance to errors is achieved intrinsically by encoding the information in a distributed way.

2.2 Classical Neural Networks

Neural Network science grew out of attempts to mimic biological neural systems by modeling the structure of the human or animal brain. The first Artificial Neural Networks is dated back to 1943, when Warren McCulloch and Walter Pitts constructed a simple neural network with electrical circuits. During the following years, research effort within the field was directed towards an artificial modeling of the human brain. As the ambiguous goal could not be achieved, Neural Network science experienced a regression that lasted until the 1980s. In 1982, John Hopfield gave new impulses to Artificial Neural Network science, focusing on the development of *useful* devices based on Neural Networks [Hopfield, 1982, Amit, 1989]. Instead of attempting to model the full human brain, he introduced a model of a physical system which exhibits some of the properties of the classical information processing in the brain. Before discussing the Hopfield model of neural networks, we review a few basic characteristics of the brain.

2.2.1 Neurophysiological Background

The brain is principally composed of a very large number of massively interconnected neurons. Each neuron is a specialized cell which can propagate an electrochemical signal. The neuron has a branching input structure (the dendrites), a cell body, and a branching output structure (the axon). The axons of one cell connect to the dendrites of another via a synapse. When a neuron is *activated*, it fires an electrochemical signal along the axon. This signal crosses the synapses to other neurons, which may in turn fire. The neurons can thus interchange signals even between distant parts of the brain. A neuron is activated, if the total signal received at the cell body from the dendrites exceeds a certain level determined by the firing threshold. The strength of the signal received by a neuron depends on the *efficacy* of the synapses. The efficacy characterizes the connection between the neurons. If one neuron is activated and thus fires a signal, the synaptic efficacies determine how much of it will be received by every connected neuron. Even though the real brain is highly complicated, even with simple models one can recover some of the features of the information processing and storage.

2.2.2 Modeling of the Brain

Among the various models in neural network science, an important group are attractive networks, where the network has stable states that are attractors. When the system is in such a stable state, it dissipates back into the state after an outer disturbance. A pattern is recalled, if under the influence of a stimulus the Artificial Neural Network drifts rapidly into an attractor such as a fixed point. When the network reaches a fixed point, it remains in the same state in every cycle. The neurons go on firing, but the synaptic efficacies reproduce the same list of active and inactive neurons. The rapid arrival at the fixed point can be identified as a recall from memory of the pattern corresponding to the state which is fixed. This state is recalled by its similarity to the external stimulus. The fixed point is the simplest kind of attractor. It "attracts", in the sense that the dynamics cause the trajectories from many initial points to flow into it. An attractor state can be illustrated by means of the motion of a ball in a landscape (see Fig. 2.2). In this analogy, the recognition pattern is identified with the

Figure 2.2: The pattern recognition in an associative memory can be visualized by an energy landscape: The local minima illustrate the stored patterns. In the picture, the ball is placed on a slope, which corresponds to a not yet recognized pattern. The arrow indicates the recognition process, in which the ball is pulled into the closest valley.

location of each bottom of the valleys, whereas the not yet recognized patterns are visualized as the position of a ball on slope or the top of a hill. During the recognition process, the ball is pulled into the closest valley.

A physical system can be used as associative memory if any prescribed set of states can be turned into stable states of the system. In the analogy of the landscape picture, the requirement translates to the possibility of shaping the landscape. All significant cognitive events, such a retrieval from memory and recognition, take place on the level of the network. Summarizing, there are three conditions for an associative memory: 1) The system has stable states that model a memory. 2) The stable states are attractors, which models the capacity of recognition. 3) The "energy landscape" of network states can be modified, which models the process of learning in the sense of building up new memories. In the following section, we discuss how these requirements are implemented in the Hopfield model of neural networks.

2.2.3 The Hopfield Neural Network model

John Hopfield proposed a model for information processing on a network of a large number of simple equivalent components [Hopfield, 1982]. The Hopfield Neural Network is constructed from identical neurons which can be in either one of the two possible states: *firing*, or *not firing*, described by the variable $S = \pm 1$, where $S = +1$ stands for a firing neuron, and $S = -1$ for a resting one. The firing state is activated if the action potential in the neuron reaches a given threshold. The state

of a neuron i changes in time depending on the incoming potential, which depends on all incoming signals. In order to calculate the potential that reaches neuron i, one has to consider two facts: Firstly, which ones of the connected neurons are active and thus fire an electrochemical potential. Secondly, the synaptic efficacy of the connection that determine what fraction of the signal reaches each connected neuron. The synaptic efficacy is described by the parameter J_{ij}, which determines the amount of post-synaptic potential that would be added to the neuron i if channel j were activated. In Fig. 2.1 d, we show a schematic view of a Hopfield network consisting of four neurons. The black and white dots represent the neurons that are in one of the two possible states. The connection between the neurons is described by J_{ij}.

In a given time slice, it can be registered which neuron is carrying an action potential and is thus in its firing state and which is not. The distribution of firing neurons at any moment determines the synapses which will receive a signal. The list of synaptic efficacies determines how much of the signal every neuron receives. This is the essential information needed by a neuron in order to compute its next state - either firing or not firing - which is what keeps information processing going.

The Hopfield model assumes symmetric efficacies, $J_{ij} = J_{ji}$ and the absence of self-interaction, $J_{ii} = 0$. An energy function H is introduced as

$$H = -\frac{1}{2}\sum_{i,j}^{N} J_{ij} S_i S_j + h \sum_{i}^{N} S_i, \tag{2.3}$$

where the first term describes the dynamics of the system and the second term represents external inputs. The function is called "energy", as the network state keeps changing until a local minimum of the energy function is reached.

The learning, or storage of information in the system is achieved, if the stored states are stable under the dynamics and correspond to a so called attractor state. The stored patterns are N-bit words, denoted by $\{\xi_i^\mu\} = \pm 1$.

We illustrate some possible patterns for a toy system of four neurons. Again, the black and white dots represent the state of the neuron.

In total, there are 2^N different combinations $\{\xi_i^\mu\}$. The storage prescription in the Hopfield network is based on the so called Hebb rule [Hebb, 1949] and is given by (see e.g. [Amit et al., 1985])

$$J_{ij} = \frac{1}{N} \sum_{\mu=1}^{p} \xi_i^\mu \xi_j^\mu. \tag{2.4}$$

The Hopfield network with the Hebb rule has a maximum storage capacity of $p = 0.14N$ [Amit et al., 1985]. It is probably the simplest example of a binary model which describes some of the characteristic properties of neural networks, such as attractor states and finite storage capacity.

In this thesis, we explore the possibility of taking advantage of some of these features for quantum information tasks. We study mechanisms to encode information and quantum fluctuations in many-body quantum systems that exhibit global emergent behavior. For this purpose, we study systems with long range interactions.

2.3 Complex Quantum Systems

One of the characteristic properties of the couplings given by the Hebb rule in Eq. 2.4 is their long-range nature. Indeed, the existence of many metastable states in the Hopfield neural network is a consequence of the long-range couplings. Let us therefore discuss two different approaches for the realization of many-body quantum systems with long range interactions: A chain of ions in a trap and atoms or molecules in an optical lattice. Furthermore, we study other complex quantum systems with no long-range interactions that exhibit paradigm behavior

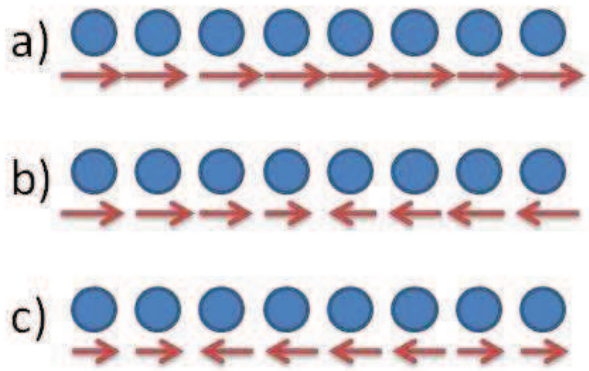

Figure 2.3: First vibrational modes for a chain of eight ions in a linear trap: a) Center of mass mode, b) breathing mode, c) Egyptian mode. The arrows indicate the motion of the ions. In the center of mass mode, the ions oscillate collectively around their equilibrium position. In the breathing mode, the left half of the ions moves in the directions contrary to the right half. In the Egyptian mode, the outer four ions move in the opposite direction of the central ones.

such as quantum phase transitions.

2.3.1 Trapped Ion Chain

Trapped ions play an important role in the experimental realization of quantum computers [Häffner et al., 2008] and quantum simulators [Porras and Cirac, 2004b, Porras and Cirac, 2004a, Friedenauer et al., 2008, Hauke et al., 2010]. Typically, the ions are trapped in a linear trap, where the trapping potential along one of the three trap axes is much weaker then along the other two, such that the ions arrange in a string. In Fig. 2.1 e, we give a schematic view of a trapped ion chain. The ions are subject to two main forces: the trapping potential and the Coulomb repulsion. The competition between harmonic squeezing and Coulomb repulsion results in oscillations of ions around its equilibrium positions. In Fig. 2.3 we illustrate the three lowest vibrational modes: The center of mass mode, the breathing mode, and the so called Egyptian mode.

Trapped ions allow for a high level of control of individual ions. The states of the

ions can be initialized with nearly perfect fidelity in a particular electronic state via optical pumping techniques. The detection of individual ions is performed with high fidelity by shining an appropriately tuned laser beam on the ion and detecting the fluorescence signal.

In our work, we are interested in spin systems with long range interaction and metastable states. Two internal states of a trapped ion can realize an effective spin 1/2 system, and the vibrational motion provides a coupling between the different spins. A realization of an effective spin-system with long range interactions in a chain of trapped ions has been proposed [Mintert and Wunderlich, 2001, Wunderlich, 2002, Porras and Cirac, 2004b, Deng et al., 2004] and experimentally demonstrated [Friedenauer et al., 2008].

The internal states of the ions are coupled to the motion by placing the ions in an off-resonant standing wave, such that they experience a state-dependent a.c. Stark shift. As a result, the system can realize an effective spin-spin Hamiltonian with long range interactions mediated by the collective motion of the ions,

$$H = -\frac{1}{2}\sum_{\alpha,i,j} J_{ij}^{\alpha}\sigma_i^{\alpha}\sigma_j^{\alpha} + \sum_{\alpha,i} B_i^{\alpha}\sigma_i^{\alpha}\,, \tag{2.5}$$

Here, the coefficient $\alpha = x, y$ and z denote the spatial directions, i, j label the ions and σ are the Pauli matrices. The coefficients J_{ij}^{α} depend on the forces between the atoms, the mass of the ion and the amplitude and frequency of the vibrational mode.

The interactions J_{ij}^{α} in Eq. (2.5) are given by

$$J_{ij}^{\alpha} = \frac{(F_{ij}^{\alpha})^2}{m}\sum_{n}\frac{M_{i,n}^{\alpha}M_{j,n}^{\alpha}}{\omega_{\alpha,n}^2}\,, \tag{2.6}$$

with $\alpha = x, y$ and z being the spatial directions, i, j labeling the ions, F_{ij}^{α} the forces in the α direction with which the j-th atom acts on the i-th one, m the ion mass, and $\omega_{\alpha,n}$ the angular frequency of the nth vibrational mode. $M_{i,n}^{\alpha}$ are the unitary matrices that diagonalize the vibrational Hamiltonian:

$$M_{i,n}^{\alpha}\kappa_{i,j}^{\alpha}M_{j,m}^{\alpha} = \omega_{\alpha,n}^2\delta_{nm}, \tag{2.7}$$

where $\kappa_{i,j}^{\alpha}$ are the elastic constants of the chain. The coefficient $M_{i,n}^{\alpha}$ gives the scaled amplitude of the local oscillations of ion i around its equilibrium position

when the collective vibrational mode n is excited. Thus, the eigenvectors of M describe each ion's contribution to a given vibrational mode, while the eigenvalues provide the oscillation frequencies, $\omega_{\alpha,n}$, of the collective modes (see Fig. 2.3).

The formal similarity of the Hamiltonian in eq. (2.5) to the Hopfield Hamiltonian eq. (2.3) is evident. In Chapter 3, we propose the implementation of a classical error resistant memory in the spirit of the Hopfield net in a trapped ion chain. Furthermore, we consider a modification of the system of trapped ions that allows for the manipulation of quantum states. We show that a set of quantum gates can be realized, where the information is distributed over the whole system.

2.3.2 Bosons in Optical Lattices

In the previous section, we have discussed a trapped ion chain as an implementation of a many-body quantum system that can be used for the storage and processing of quantum information in a global, distributed way. Another approach to the experimental realization of controllable quantum many-body systems are atoms in optical lattices. Optical lattices are realized by the interference patterns of laser beams propagating in different directions. The atoms are trapped by optical dipole forces and, depending on the detuning, are confined to the regions with maximum or minimum laser intensity of the standing wave. That way, one obtains a highly regular and controllable crystal of atoms. In Fig. 2.1 f, we depict a schematic view of a system of atoms in an optical lattice.

Optical lattices are of interest for a wide range of applications, such as the study of many-body effects in condensed matter physics or the implementation of devices for quantum computing. For our purposes, dipolar atoms or molecules are of particular interest, as long-range interactions can be achieved by dipole-dipole forces. It has been demonstrated theoretically that such systems with long range interactions have a great variety of metastable states. These systems could work as quantum multimode memory when mapping the fluctuation of light on the atoms via the Faraday effect.

In comparison to the system of ions, optical lattices have the advantage that very large systems can be created relatively easily [Bloch, 2008]. The control and manipulation of single atoms within the system is challenging, however, the detection of single atoms has been achieved recently [Bakr et al., 2010, Sherson

et al., 2010]. In the second part of the thesis, Chapters 4-7, we consider the detection and characterization of strongly correlated quantum systems by particle counting. In the remaining part of this section, we recall some of the properties of particles in optical lattices.

The Bose-Hubbard Model

We describe the Bose-Hubbard model as a paradigmatic model for the study of strongly correlated systems in optical lattices. Fermionic particles in an optical lattice can be described in a similar way. The dynamics of the atoms in the lattice are determined by the tunneling rate between two sites and the on-site interaction energy. The system is described by the Bose-Hubbard Hamiltonian,

$$H = -J \sum_{\langle i,j \rangle} a_i^\dagger a_j + \frac{U}{2} \sum_i \hat{n}_i(\hat{n}_i - 1) - \mu \sum_i n_i. \tag{2.8}$$

Here, $a_i^\dagger$ and a_i are the bosonic creation and annihilation operators at site i, n_i is the associated number operator, μ is the uniform chemical potential and $\langle i,j \rangle$ stands for the nearest neighbor pairs. The strength of the tunneling term is characterized by the hopping amplitude J. The interaction between two atoms on a single site is described by the the on-site interaction U.

For shallow lattice potentials, i.e. in the limit $J \geq U$, where the tunneling term dominates the Hamiltonian, the system is in a superfluid (SF) phase. The ground-state energy is minimized if the single-particle wavefunctions are spread out over the entire lattice. The many-body ground state is then given by

$$|\Psi_{SF}\rangle \propto \left(\sum_{i=1}^{M} a_i^\dagger \right)^N |0\rangle, \tag{2.9}$$

where N is the number of atoms and M is the number of lattice sites. This state is characterized by a long-range phase coherence throughout the lattice.

For deep lattice potentials, i.e. in the limit $U \gg J$, where the on-site interactions dominate, the system is in a Mott-insulating (MI) phase. The ground state consists of localized atomic wave functions with a fixed number of atoms per site. The many-body ground state is a product of local Fock states, given by

$$|\Psi_{MI}\rangle = \prod_i |n_i\rangle .$$

Here, $|n\rangle$ is the n-particle Fock state, defined as

$$|n\rangle = \frac{1}{\sqrt{n!}}(a^\dagger)^n|0\rangle. \tag{2.10}$$

As the ratio U/J between the on-site interactions and the tunneling rate changes, the system undergoes a quantum phase transition from the SF to the MI phase [Fisher et al., 1989, Jaksch et al., 1998]. Experimentally, it was observed for the first time by analyzing the interference pattern after an expansion of the atoms released from the lattice [Greiner et al., 2002].

Metastable States

In the Bose-Hubbard-Hamiltonian in eq. (2.8), only interactions between neighboring sites are considered. It was observed that when introducing long range interactions between the atoms, new phases appear, both in the SF [Batrouni and Scalettar, 2000, Sengupta et al., 2005] and MI [Kovrizhin et al., 2005, Góral et al., 2002] region of the phase diagram. Such long-range interactions can be induced by dipole-dipole interactions U_{dd}. This is true because the dipole-dipole potential decays as $U_{dd} \propto 1/r^3$, whereas the van der Waals potential is proportional to $1/r^6$. In [Menotti et al., 2007, Trefzger et al., 2008] it was shown that for dipolar atoms or molecules in a two dimensional optical lattice, the long range interactions induced by the permanent dipole moment of the atoms provide the system with a rich phase diagram with a large number of metastable states that are local energy minima. These metastable states typically consist of localized atoms following a specific pattern, where the average number of atoms per site in general is not integer. An example is the so-called checkerboard phase, where the sites are alternately empty and occupied.

In order to make use of the characteristic features of such systems, it is essential to develop methods to experimentally prepare and detect these metastable states. In [Trefzger et al., 2008] it was shown, that the states with the desired configuration can be prepared by using superlattices, where the dipole-dipole interactions allow for a stable configuration even after removing the superlattice. Furthermore, the transfer from one metastable configuration to another can be achieved in a quantum controlled process using superlattices. For a review over the recent experimental and theoretical advances, see [Lahaye et al., 2009].

The detection of the different metastable states can be achieved by analyzing the spatial noise correlations in the time of flight images (see Sect. 2.4.1). This method in principle allows for the characterization of the geometry of the density pattern in the lattice as well as the presence of defects in the pattern. However, the required signal to noise ratio for the detection of defects is beyond present experimental possibilities. In our work, we explore the possibility of detecting the metastable states by particle counting (see Chapter 6).

The recent development of the quantum gas microscope technique allows for the detection of atoms at single sites [Bakr et al., 2009, Sherson et al., 2010]. This technique could, in principle, be used to observed the density distributions of different metastable states.

2.3.3 Anisotropic Quantum xy-Model

Apart from systems with long-range interactions and metastable states, we consider other systems that present paradigm models in many-body quantum mechanics. Spin models play an important role in a variety of research fields of physics. They are of fundamental interest to describe phenomena in condensed matter physics [Schollwöck et al., 2004], and are of great importance for quantum information science. The connection between entanglement and dynamic many-body properties like quantum phase transitions (QPTs) has attracted much interest [Osterloh et al., 2002, Plenio and Virmani, 2007], and a wide range of proposals for quantum computing concern spin models (see e.g. [Briegel et al., 2009, Micheli et al., 2006]).

In Chapter 5, we consider the anisotropic XY spin model [Katsura, 1962, Pfeuty, 1970, Barouch et al., 1970, Barouch and McCoy, 1971a, Barouch and McCoy, 1971b] as a paradigmatic model for a many-body quantum system that exhibits a quantum phase transition. In particular, we are interested in the detection of the many-body properties of the system by spin counting. The Hamiltonian is given by

$$H_{xy} = -J \sum_{j=1}^{N} \left[(1+\gamma) S_j^x S_{j+1}^x + (1-\gamma) S_j^y S_{j+1}^y + g S_j^z \right], \tag{2.11}$$

where S_j^α are the spin 1/2 operators at site j, J is the coupling strength, $0 < \gamma < 1$ is the anisotropy parameter, and g is the parameter of the transverse field. The

case $\gamma = 1$ corresponds to the Ising model in a transverse field. For $\gamma = 0$, the system corresponds to the isotropic XY-model or XX-model. It is well known that the system exhibits a quantum phase transition driven by the transverse magnetic field g [Sachdev, 2001]. The extreme cases $g = 0$ and $g = \infty$, correspond to systems with no external field and with no interactions, respectively. The phase transition between the states with different orientations of the magnetization takes place at $g = 1$. For small transverse fields, $g < 1$, the ground state has magnetic long-range order and the excitations correspond to kinks in domain walls. For high transverse fields, $g > 1$, the system is in a quantum paramagnetic state.

The special cases $\gamma = 0$ and $\gamma = \pm 1$ can be realized with single species bosons in the hard core (i.e. strongly repulsive) bosons limit [Sachdev, 2001, Lewenstein et al., 2007]. Another possibility is to use a chain of double-well sites filled with bosons interacting via weak dipolar forces [Dorner et al., 2003]. In general, one should use a two-component Bose-Bose or Fermi-Fermi mixture in the strong coupling limit, and in the Mott insulator state with one atom per site. The two components provide then the two components of (pseudo) spin-1/2. Spin-spin interactions are induced by exchange mechanism via virtual tunnelings of atoms [Auerbach, 1994, Anderlini et al., 2007, Trotzky et al., 2008]. The system is then described by an asymmetric (XXZ) Heisenberg model (see e.g. [Lewenstein et al., 2007, Wehr et al., 2006]) in the Z-oriented field. By appropriate tuning of the scattering lengths via Feshbach resonances, one can set the $S^z_{j+1}S^z_j$ coupling to zero, i.e. achieve the XX model in the transverse field. In order to achieve the asymmetry γ, one should additionally introduce tunneling assisted with a laser or microwave induced double spin flip. For this aim, one should make use of the resonance between the virtual on-site two atom "up-up" and "down-down" states, without disturbing "up-down" configurations.

The anisotropic XY model eq. (2.11) can be transformed to a system of non-interacting fermions by the Jordan-Wigner transformation [Jordan and Wigner, 1928, Sachdev, 2001], followed by Fourier and Bogoliubov transformations. Let us outline the basic steps. First, the spin operators are written as

$$S^x_j = \frac{1}{2}(b^\dagger_j + b_j), \;\; S^y_j = \frac{1}{2i}(b^\dagger_j - b_j), \;\; S^z_j = (b^\dagger_j b_j - \frac{1}{2}),$$

where the operators b_i are defined in terms of the Fermi operators $(c_i, c^\dagger_i)$ in the

following way:

$$b_j = \exp(-\pi i \sum_{k=1}^{j-1} c_k^\dagger c_k) c_j, \;\; b_j^\dagger = c_j^\dagger \exp(\pi i \sum_{k=1}^{j-1} c_k^\dagger c_k). \tag{2.12}$$

Let us note that the Jordan-Wigner transformation works for open chains, and in particular for an infinite chain. We will nevertheless assume periodic boundary conditions. For large N, this procedure gives the right leading behavior.

Inserting eqs. (2.12) and (2.12) into eq. (2.11), we obtain the fermionic Hamiltonian

$$\hat{H} = -J \sum_{j=1}^{N} (\hat{c}_j^\dagger \hat{c}_{j+1} + \gamma \hat{c}_j^\dagger \hat{c}_{j+1}^\dagger + h.c. - 2g \hat{c}_j^\dagger \hat{c}_j + g). \tag{2.13}$$

Here, $\hat{c}_j^\dagger$ denotes the creation of a fermion on site j, N is the number of sites, J is the energy associated to fermion tunneling to nearest-neighbor lattice sites, g is proportional to the chemical potential of the system and γ accounts for the formation of pairs between consecutive sites.

Performing a Fourier transform,

$$\hat{c}_k^\dagger = \frac{1}{\sqrt{N}} \sum_{j=1}^{N} \exp(ij\Phi_k) \hat{c}_j^\dagger, \tag{2.14}$$

the Hamiltonian eq. (2.13) reads

$$H = \frac{J}{2} \sum_k 2(g - \cos(\Phi_k) c_k^\dagger c_k) - i\gamma \sin(\Phi_k)(c_{-k}^\dagger c_k^\dagger + c_{-k} c_k), \tag{2.15}$$

where $\Phi_k = 2\pi k/N$. Finally, eq. (2.15) is diagonalized by a Bogoliubov transformation. The Hamiltonian reduces, up to a zero energy shift, to the noninteracting fermionic Hamiltonian

$$\hat{H} = \sum_{k=1}^{N/2} \hat{H}_k = \sum_{k=1}^{N/2} E_k \hat{n}_k^d, \tag{2.16}$$

where

$$\hat{n}_k^d = \hat{d}_k^\dagger \hat{d}_k + \hat{d}_{-k}^\dagger \hat{d}_{-k} \tag{2.17}$$

$$\hat{d}_k = u_k \hat{c}_k - i v_k \hat{c}_{-k}^\dagger, \quad d_k^\dagger = u_k \hat{c}_k^\dagger + i v_k \hat{c}_{-k}, \tag{2.18}$$

$$u_k = \cos\tfrac{\theta_k}{2}, \quad v_k = \sin\tfrac{\theta_k}{2}, \tag{2.19}$$

$$E_k = J\sqrt{(\cos\Phi_k - g)^2 + \gamma^2 \sin^2\Phi_k}, \tag{2.20}$$

$$\tan\theta_k = \tfrac{\gamma \sin\Phi_k}{\cos\Phi_k - g}, \tag{2.21}$$

In order to recover the Hamiltonian (2.13), for $(\cos\Phi_k - g) < 0$ the solution of eq. (2.21) is taken from the $(\frac{\pi}{2}, \frac{3\pi}{2})$-branch of the tangent, whereas for $(\cos\Phi_k - g) < 0$ it is taken from the $(-\frac{\pi}{2}, \frac{\pi}{2})$-branch.

It can be seen from eq. (2.19) that the coefficients u_k^2 and v_k^2 change their roles at the phase transition such that on one side of the critical point, the number operator of the quasiparticles $\hat{d}_k^\dagger \hat{d}_k$ corresponds to $\hat{c}_k^\dagger \hat{c}_k$, whereas on the other side it corresponds to $\hat{c}_k \hat{c}_k^\dagger$.

From eqs. (2.12)-(2.12) it is clear that, up to a constant, the spin operator S_j^z corresponds to the number operator for the fermions $c_j^\dagger c_j$. This allows us to use the formalism for fermion counting to study the spin counting statistics. In Chapter 5, we show that the quantum phase transition is visible in the mean and variance of the spin counting distribution of S_j^z.

2.3.4 Fermions in Optical Lattices

In the previous section, we considered the Jordan Wigner transform, which describes a mapping between spins and fermions. The anisotropic XY model is mapped onto a system of strongly correlated fermions described by the Hamiltonian eq. (2.13). The study of strongly correlated fermions in optical lattices is of great interest, as they provide highly controllable systems that resemble correlated electron systems in condensed matter.

Quantum degenerate fermionic atoms trapped in optical lattices [Jördens et al., 2008] may become superfluid if there are attractive interactions between atoms trapped in two different hyperfine states [Chin et al., 2006]. Attractive fermions form pairs analogous to Cooper pairs in superconductors. A one component system of fermions trapped in the same hyperfine state may also become superfluid though not in s-wave configurations. Such a system, in the 1D case, can be described by the Hamiltonian eq. (2.13), where the term proportional to γ describes the pairing of particles.

One way to realize such Hamiltonians with ultracold atoms is to use a Fermi-Bose mixture in the strong coupling limit. In this limit, the low energy physics is well described by fermionic composites theory [Lewenstein et al., 2004], in which fermions form composite objects with a certain number of bosons, or bosonic

holes repectively. The fermionic composites undergo tunneling and interact via nearest neighbor interactions, which may be repulsive or attractive, weak or strong, depending on the original parameters of the system, such as scattering lengths, etc. In the case of weak attractive interactions, the system undergoes, at zero temperature, a transition into a "p-wave" superfluid, described well by the Bardeen-Cooper-Schrieffer (BCS) theory [Leggett, 2006], corresponding exactly to the Hamiltonian (2.13).

In Chapter 5, we study the quantum many-body properties of the fermionic system eq. (2.13) by fermion counting. In particular, we are interested in the effect of temperature. We show that the phase transition is visible when the temperature is small compared to the system energy. Furthermore, we show that the breaking of fermionic pairs as temperature increases is reflected in the counting distribution.

2.4 Detection of Quantum Many-Body Systems

In this Section, we review some of the main methods for the detection of quantum many-body systems.

We first discuss the time of flight (TOF) absorption imaging, which gives access to the first-order correlation functions. The detection of strongly-correlated systems requires the measurement of second or higher order correlation functions, which can be experimentally accessed through noise interferometry. Further methods for the detection of strongly correlated systems are modulation- and Bragg spectroscopy. Finally, we discuss experimental techniques for particle counting.

In Chapter 4-7, analyze the detection of various cold atomic systems by particle counting. As a well known example, photon counting has been a key element for the characterization of the quantum properties of light. As for the case of photons, interesting quantum properties of atomic systems can be detected by particle counting. In particular, the counting statistics give insight into the characteristic many-body behavior of strongly correlated systems.

2.4.1 Time of Flight Absorption Imaging

The TOF absorption imaging is used routinely in experiments with cold atoms. The atomic cloud is imaged after a free ballistic expansion. The spatial density distribution of the cloud is measured by illuminating it with resonant laser light, which is absorbed by the cloud and the shadow can be measured with a charge coupled device (CCD) camera. Properties of the system which are related to phase correlations appear as spatial structures after the TOF expansion and can usually be measured very well with this kind of imaging technique [Fölling, 2008]. The TOF absorption imaging gives access to phase correlations between lattice sites. In the Mott Insulator regime, where particles at different lattice sites are uncorrelated, the TOF distribution is determined by the on-site properties of the atoms in the lattice. All atoms from each site are released fully independently of all other sites, and the image is a featureless Gaussian. However, each single shot image exhibits significant fluctuations around the average value. In the SF, the fourier transform of the zero momentum distribution is reflected in the TOF absorption image.

2.4.2 Noise Interferometry

The analysis of the image noise can reveal higher order interference patterns originating from the spatial ordering in quantum systems. Noise interferometry was proposed in [Altman et al., 2004] as a means to study the properties of strongly correlated systems of ultracold atoms. A well known example for the spatial correlations of atoms after a TOF period is the Hanbury Brown-Twiss (HBT) effect [Hanbury-Brown and Twiss, 1956a, Hanbury-Brown and Twiss, 1956b]. In their original work, Hanbury Brown and Twiss observed photons emitted from a star using two detectors. They found that when a photon was detected on one of the detectors, it was highly likely that at the same time a photon would be detected at the other one. This 'bunching' is characteristic for all bosonic particles, whereas for fermions an 'antibunching' is observed.

In optical lattices, the second order correlations reflect the spatial distribution of the atoms inside the lattice and have been experimentally measured for the first time in the atom shot noise of the two dimensional density distribution measured by TOF absorption imaging in [Greiner et al., 2002]. In [Rom et al.,

2006], the antibunching of free neutral fermionic atoms was demonstrated using noise interferometry for a degenerate single component Fermi gas released from a three dimensional optical lattice potential. The detection of the metastable states of systems with dipolar atoms or molecules in optical lattices using noise interferometry was proposed in [Trefzger et al., 2008].

2.4.3 Modulation- and Bragg Spectroscopy

Bragg spectroscopy has been proposed and applied as a method for probing many-body quantum systems. The method can be considered as an analog to inelastic neutron scattering for solids. In [Rey et al., 2005] and [van Oosten et al., 2005], Bragg spectroscopy of ultracold atoms is proposed for probing the excitation spectrum in the Mott-insulator phase in a one-dimensional (1D) optical lattice. It is shown that Bragg spectroscopy is an experimental technique with the potential to thoroughly characterize the Mott phase. In the experiment in [Ernst et al., 2010], see also [Moritz, 2010], the evolution of the quasiparticle spectrum for a superfluid system is monitored as the system is tuned from the weakly to the strongly interacting regime, where they achieve access to the whole excitation spectrum by momentum-resolved Bragg spectroscopy. The recent advances show, that Bragg spectroscopy can contribute to the understanding of strongly correlated quantum systems.

Using modulation spectroscopy [Kollath et al., 2006, Jördens et al., 2008], the system is probed by applying a periodic modulation of the lattice potential. The thereby induced double occupancies are used to infer the state of the system.

2.4.4 Atom Counting

Particle counting gives access to high order quantum correlations. The counting technique has been applied extensively to characterize different quantum states of light, and recent experimental advances open new possibilities to access the counting statistics of massive particles. As for the case of photons, the counting statistics can reveal the quantum properties of many-body systems and can be applied as a further method for detecting strongly correlated systems. The counting of many-body systems can be performed in-situ inside the lattice, or

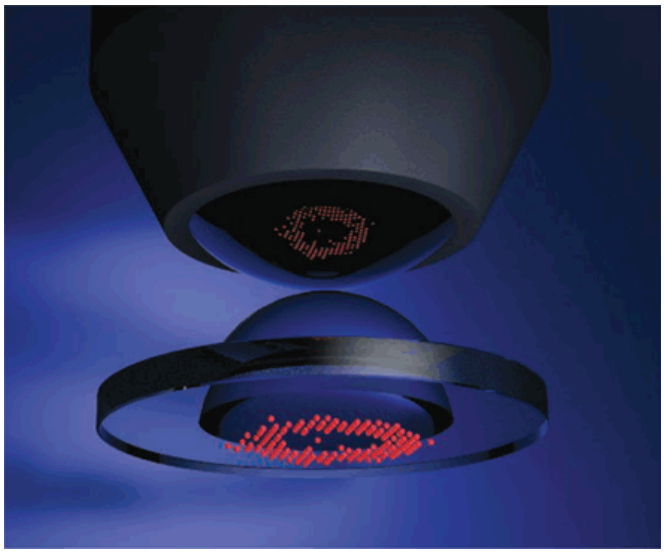

Figure 2.4: Sketch of the experimental setup used in the experiment by Bakr et al. At the bottom, atoms (shown in red) are trapped in a lattice. The atoms are imaged in situ in the lattice by a high-resolution imaging system. Source: M. Greiner Lab.

after opening the potential and letting the particles fall onto a detector, such as a micro-channel plate.

The in-situ detection of individual atoms in optical lattices has recently become available [Sherson et al., 2010, Bakr et al., 2010]. Single-site resolution is achieved by fluorescence imaging using a high-resolution objective functioning as a microscope (Fig. 2.4). With these techniques provide direct access to the counting statistics of the atoms in the lattice. In the experiment of [Sherson et al., 2010], high resolution imaging of strongly interacting bosonic Mott insulators in an optical lattice with single-atom and single-site resolution is achieved. In the experiment of [Bakr et al., 2010], single atom and single lattice site imaging is applied to investigate the Bose-Hubbard model on a microscopic level. A space- and time-resolved characterization of the number statistics across the superfluid-Mott insulator quantum phase transition is obtained. The experiment of [Gericke et al., 2008] provided the first experimental demonstration of single-site addressability in a sub-micrometre optical lattice. In [Gemelke et al., 2009], the density profiles of a of a two-dimensional ultracold atomic gas that crosses the superfluid to Mott insulator transition are obtained by direct in-situ imaging. In [Campbell et al., 2006] the SF-MI transition was probed by using microwave spectroscopy.

Sites with different occupation numbers are distinguished and are directly imaged for occupation numbers from one to five. In [Cheinet et al., 2008], the atom number distribution of an ultracold degenerate cloud of ^{87}Rb in the superfluid or strongly interacting regime of a Mott Insulator is fully determined by observing the interaction blockade-induced tunneling resonances.

The first precise detection experiments were performed in an expanding cloud of metastable atoms that fall onto a micro-channel plate. The experimental progress was stimulated by the observation of a Bose-Einstein condensate in a dilute gas of metastable Helium [Pereira Dos Santos et al., 2001]. In the experiment in [Schellekens et al., 2005], the Hanbury Brown Twiss effect is observed for a thermal cloud of ultracold bosons after a free expansion. In the experiment in [Jeltes et al., 2007] (see also [Lewenstein, 2007]), the Hanbury Brown-Twiss effect for bosons (^{4}He) and fermions (^{3}He) is compared in the same apparatus. In their experiment, a cold cloud of metastable helium atoms is released from a magnetic trap. The cloud expands and falls under the effect of gravity onto a time-resolved and position-sensitive detector (micro-channel plate and delay-line anode) that detects single atoms (See Fig. 2.5). In principle, the experimental data allows for the reconstruction of the complete counting distribution of the atoms.

In [Öttl et al., 2005], the full counting statistics of single atoms extracted from a weakly interacting Bose-Einstein condensate of ^{87}Rb atoms is measured. The detection takes place in a high-finesse optical cavity, where single atom transits are identified (See Fig. 2.6). In that way, the bosonic counting statistics and the bosonic Hanbury Brown Twiss effect are measured.

2.4.5 Spin counting

Furthermore, we are interested in the counting statistics of the total spin for atoms with spin or pseudospin degrees of freedom. The spin counting can be achieved via quantum nondemolition polarization spectroscopy (QNDPS). The idea relies on the coupling between the z-component of the total atomic spin, S_z , and the z-component J_z of the Stokes vector of the light (see e.g. [Julsgaard, 2003]). The coupling is based on the quantum Faraday effect: a polarized light beam that passes through the atomic sample undergoes a polarization rotation. The atomic

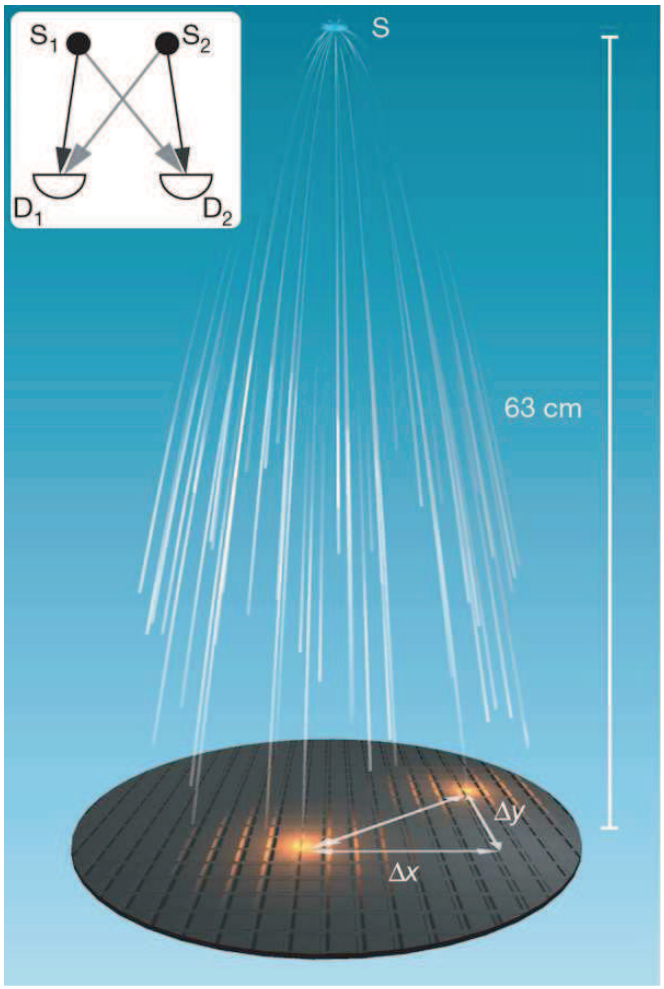

Figure 2.5: Sketch of the experiment by Jeltes et al. A cold cloud of metastable helium atoms is released from a magnetic trap. The cloud expands and falls in the gravitational field onto a microchannel plate and delay-line anode that detects single atoms. The inset illustrates the interference between the two 2-particle amplitudes that lead to bunching or antibunching. Source: [Jeltes et al., 2007]

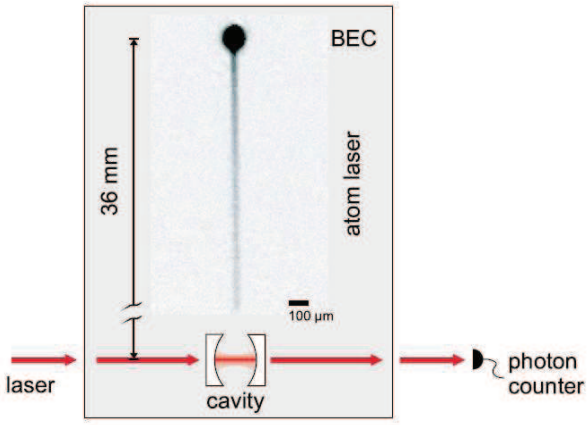

Figure 2.6: Sketch of the experimental setup by Öttl et al. A weak continuous atom laser beam is released from a Bose- Einstein condensate and enters a high-finesse optical cavity, where single atoms in the beam are detected. Source: [Öttl et al., 2005]

fluctuations thus leave a measurable imprint on the quantum fluctuations of the light, and vice versa. The idea has been experimental demonstrated in [Sørensen et al., 1998]. The method works also for degenerate atomic gases [Eckert et al., 2007] and allows for spatial resolution, when standing laser beams are employed [Eckert et al., 2008] (See Fig. 2.7).

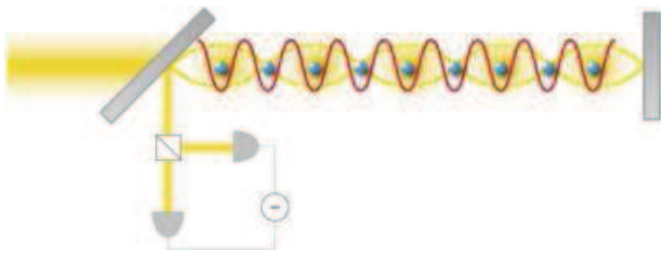

Figure 2.7: Sketch of the proposal of Eckert et al. The spins are trapped in an optical lattice (red) and are detected in situ in the lattice using a standing wave (yellow). The polarization of the light rotates due to the coupling to the atomic spins. The polarization rotation, proportional to the atomic spin, is measured using a homodyne detector. Source: [Eckert et al., 2008]

Chapter 3

Neural Network Models in a Trapped Ion Chain: Manipulation of Classical and Quantum Information

In this chapter, we propose to make use of the many-body features of a trapped ion chain for the error resistant storage and processing of information - both classical and quantum.

In Sect. 3.1, we focus on the implementation of a classical neural network in a trapped ion chain. We study the error resistance of the model and show that different patterns of the spin system can be stored with high fidelity.

In Sect. 3.2, we propose the implementation of a device for quantum computing in a chain of trapped ions. We discuss the implementation of the system and show that one-qubit and two-qubit gates can be performed. Furthermore, we study the effects of noise on the system and show that the gate protocols are resistant to high levels of noise.

3.1 Classical Neural Network in Trapped Ion Chain

Ions in a trap allow for the implementation of a pseudo spin-1/2 system with long range interactions (see Sect. 2.3.1). In this section, we propose an implementation of a neural-network like system for the storage of classical information and show that the system is resistant to a high level of noise.

3.1.1 Implementation

Our aim is to realize the Hopfield Hamiltonian eq. (2.3) with a trapped ion chain. We consider a system of the form of eq. (2.5), where we choose a confining potential that is much weaker in one of the three directions, $\omega_{x,1} = \omega_{y,1} \gg \omega_{z,1}$, such that the ions crystalize in a linear chain in z-direction. We consider external forces that act only on the z-axis and assume zero magnetic fields $B_i = 0$. Furthermore, the Pauli matrices are substituted by classical Ising spins $S = \pm 1$, where the effective spin corresponds to the internal state of the ion. The system Hamiltonian thus reads

$$H = -\frac{1}{2}\sum_{i,j} J_{ij} S_i S_j, \quad \text{where} \quad J_{ij} = \frac{(F_{ij})^2}{m} \sum_n \frac{M_{i,n} M_{j,n}}{\omega_n^2} \tag{3.1}$$

and $M_{i,n}$ denotes the scaled amplitude of the local oscillations of ion i around its equilibrium position when the collective vibrational mode n is excited. Eq. (2.3) with the interactions given by eq. (2.4) and (3.1) are of the same form and the possibility to implement a classical neural network using a linear chain of ions arises. We analyze the possibility of storing certain spin patterns as stable states in the system.

The initial spin configuration is fixed by mimicking the signs of a given vibrational mode. As illustrated by the arrows in Fig. 2.3, in the center of mass mode the ions all move in the same direction. We thus chose an initial spin pattern in which all the spins point in the same direction, $|\uparrow\uparrow ... \uparrow\rangle$ and $|\downarrow\downarrow ... \downarrow\rangle$. For the breathing mode, the right half of the ions move in a direction opposite to the left half, such that the spin patterns are given by $|\uparrow\uparrow ... \uparrow\downarrow\downarrow ... \downarrow\rangle$ and $|\downarrow\downarrow ... \downarrow\uparrow\uparrow ... \uparrow\rangle$ The patterns to be stored must have large basins of attraction, i.e. they should

correspond to sufficiently different configurations of spins, so that each configuration is dynamically recovered even if several spins are randomly flipped.

Before discussing the error resistance of the stored patterns, we point out some important differences between the interactions J_{ij} in the Hopfield model eq. (2.4), and the spin model eq. (3.1). Let us recall that in the Hopfield model, the interactions are determined by the patterns to be stored, $\{\xi_i^\mu\} = \pm 1$, where each pattern μ is an N-bit word with entries -1 and 1. In contrast, in the trapped ion chain, the interactions are fixed by the vibrational modes and are not necessarily equal to ± 1. Furthermore, for the Hopfield network, the number p of stored patterns in eq. (2.4) is bounded from above by $p = 0.14N$ [Amit, 1989]. In the ion chain model, the sum in the term J_{ij} in Eq. (3.1) extends over all N vibrational modes.

Another important difference is given by the fact, that in the Hopfield model all the patterns have the same weight, while in the ion chain each vibrational mode is weighted by $1/\omega_n^2$. In [Pons et al., 2007] we show that the model depends crucially on ratio of the frequencies of the vibrational modes.

The spectrum of the vibrational modes can be modified by changing the trapping potential. For the harmonic trapping potential, the ratio between the first vibrational mode (center of mass mode) and the second vibrational mode (breathing mode) is given by $\omega_2/\omega_1 = \sqrt{3}$ [James, 1998], such that the requirement of degeneracy is not met. However, for the first two vibrational modes, the requirement can be fulfilled using a modified trapping potential of the form $V \propto \mid x \mid^\gamma$. In Fig. 3.1 a) we plot the ratio between the frequencies of the second and the first mode, ω_2/ω_1, as a function of γ for the case of 20 ions. For $N \geq 20$, this ratio does not depend on the number of ions. For $\gamma < 0.8$, the ratio is close to one, such that we choose the exemplary value of $\gamma = 0.5$ to implement the Hopfield neural network on the chain or trapped ions.

3.1.2 Error Resistance of the Model

We probe the stability of the system by analyzing its response to external perturbations, such as spin flips. We first calculate the phonon spectrum, impose the learning rule, and then probe the correlation between the dynamically stable configurations and the stored ones.

The first step consists in finding the equilibrium positions of the ions and calculating the vibrational modes and frequencies by using a standard diagonalization procedure. Once the complete vibrational spectrum of the system is known, the interactions among spins J_{ij} are calculated, and the energy of the system is evaluated. The dynamical thermalization of the system is simulated using standard Monte Carlo techniques.

Starting with the initial spin configuration, r spins are randomly flipped and the system then evolves towards the equilibrium situation assuming a noiseless scenario. If the system recovers the initial configuration, the configuration is stable under the flip of r spins. The number of initial spin flips determines the initial overlap, defined as $m_i = (N - r)/N$. After dynamical evolution, the final overlap is given by $m_j = (N-s)/N$ where s is the number of spins that differ from the initial configuration. This process is repeated over M initial different random r spin flips to evaluate statistically the final overlap with the initial configuration: $m_f = (\sum_{j=1}^{N} m_j n_j)/M$, n_j being the number of times that the system reaches the m_j configuration. The value of the initial overlap for which significant decrease of the final overlap occurs, is a good measure of the size of the basin of attraction of the corresponding pattern. In Fig. 3.1 b), we plot the final overlap m_f as a function of the initial overlap m_i for a system of $N = 40$ spins. We consider the patterns corresponding to the first two vibrational modes. We show that the fidelity is close to unity up to $m_i \simeq 0.8$, which corresponds to eight spin flips. The system does not always recover the initial pattern but instead sometimes reaches a slightly deformed configuration, which differs only in one spin flip from the original one.

3.2 The Quantum Neural Network Model

Let us now study a model of a Quantum Neural Network (QNN), which is based on the classical neural network model discussed in the previous section. We show that such a system could be used for the manipulation of quantum data. Just like in classical neural networks, where the classical information is encoded in distributed metastable minima of the whole network, the quantum information is encoded in the patterns of the spin system. We are particularly interested in the robustness to noise that results from the distributed information encoding.

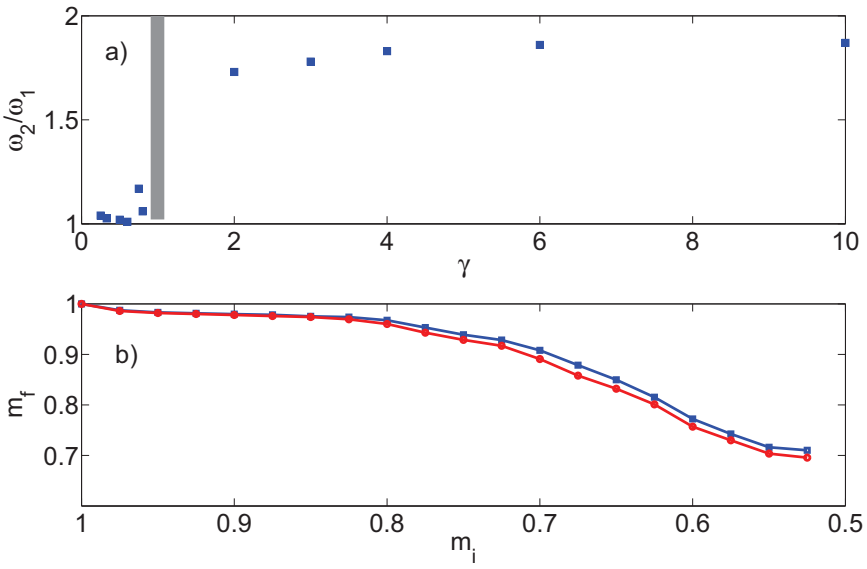

Figure 3.1: a) The ratio between the frequencies of the second and first vibrational modes of the chain of trapped ions is determined by the exponent of the trapping potential. In order to reproduce the Hopfield Neural Network model, the ratio is required to be close to one. For a system of 20 Ca^+ ions, the requirement is fulfilled for $\omega_2/\omega_1 < 0.8$. The grey bar at $\gamma = 1$ marks the region where ω_2/ω_1 is not well defined since the second mode does not exist because of the constant character of the force produced by the external potential. b) The associative memory implemented in a trapped ion chain is probed by determining the rate of recovery of the stored states from initially distorted states. For a system of 40 ions in a potential $V = \rho|x|^{0.5}$ with $\rho = 6.6 \times 10^{-20} J/m^{1/2}$, we plot the final overlap averaged over 500 initial configurations as a function of the initial overlap, for the spin pattern where all spins point in the same direction (blue squares) and where the right half of the spins point in the opposite direction of the left half (red circles). Up to a value of $m_i \simeq 0.8$, which corresponds to eight spin flips, the state is recovered with near unit fidelity.

The qubit operations are implemented by adiabatically changing magnetic fields. Below, it will be shown that quantum computing in a system described by the QNN Hamiltonian is resistant to a high level of noise. The noise resistance is achieved by encoding the quantum information distributed in the eigenstates of the whole system.

Before discussing the implementation of the quantum neural network model, let us note that adiabaticity has been proposed for quantum information processing in the context of "adiabatic quantum computation" (see [Farhi and Gutmann, 1998,Farhi et al., 2000,van Dam et al., 2001,Aharonov et al., 2007] and references therein). However, the main difference between the above mentioned works and our approach is that adiabatic quantum computation typically considers a certain quantum algorithm, and depending on the algorithm, a certain Hamiltonian is chosen. In our work, there is one single quantum Hamiltonian, that will be shown below to be enough for all quantum algorithms, as the Hamiltonian implements universal gates, which can be applied to simulate arbitrary quantum algorithms.

Let us now turn the discussion to our QNN model. Firstly, we describe the system and define the qubit encoding. Secondly, we describe the gate implementations and finally, we consider the robustness to noise.

3.2.1 The Quantum Neural Network Hamiltonian

We consider a system consisting of eight spin-1/2 particles with long range interactions, that are subject to slowly changing external magnetic fields. As discussed in Sect. 2.3.1, such a system can be implemented with ions in a trap, where two internal states of each ion serve as the "up" and "down" states of the spin-1/2 particles, see [Mintert and Wunderlich, 2001,Wunderlich, 2002,Porras and Cirac, 2004b,Deng et al., 2004]. As in the classical case discussed in the previous section, we assume $F_{ij}^x = F_{ij}^y = 0$ in eq. (2.6). The Hamiltonian then describes an Ising interaction, which, in principle, can be long-range. The fields B_i^α in eq. (2.5) remain as external parameters that can be manipulated by the experimenter. Here, we consider two time dependent fields: One in z-direction and one in x-direction. We expand the system in the vibrational modes and keep the first three terms

(see Fig. 2.3). The Hamiltonian reads

$$H(t) = -\lambda\Big[r_1\left(\sum_{i=1}^{8}\sigma_i^z\right)^2 + r_2\left(\sum_{i=1}^{4}\sigma_i^z - \sum_{i=5}^{8}\sigma_i^z\right)^2 + r_3\left(\sum_{i=1}^{2}\sigma_i^z - \sum_{i=3}^{6}\sigma_i^z + \sum_{i=6}^{8}\sigma_i^z\right)^2 + A(t)(\sum_{i=1}^{8}\sigma_i^x) + B_1(t)(\sum_{i=1}^{4}\sigma_i^z) + B_2(t)(\sum_{i=5}^{8}\sigma_i^z)\Big], \tag{3.2}$$

where the term proportional to r_i corresponds to the ith vibrational mode and the $\pm$ signs indicate the movement of the particles with respect to each other, see Fig. 2.3. The overall factor λ has the units of energy and makes the rest of the parameters in the Hamiltonian dimensionless. The parameters $A(t)$, $B_1(t)$ and $B_2(t)$ correspond to the external magnetic fields. For the gate transformations we consider below, the external fields are depicted in Fig. 3.2 a).

The time evolution of the system is given by the time dependent Schrödinger equation,

$$i\hbar\frac{d}{dt}\left|\Psi(t)\right\rangle = H(t)\left|\Psi(t)\right\rangle, \tag{3.3}$$

The evolution is considered adiabatic, if the change of the Hamiltonian is small compared to the gap $g(s)$ between the energy levels, where we introduce the scale factor $s = \frac{t}{T}$. More precisely, the adiabatic condition is given by

$$T \gg \hbar\frac{\parallel \frac{d}{ds}H(s) \parallel}{g(s)^2}, \tag{3.4}$$

where $\parallel A \parallel$ is the operator norm of A, defined as the square root of the maximal eigenvalue of $A^\dagger A$. For the fields depicted in Fig 3.2 a) the dynamics of the five lowest energy eigenvalues are shown in 3.2 b) for the indicated values of r_1, r_2 and r_3. The energy gap $g(s)$ is defined as the minimum distance between neighboring energy levels.

As discussed in Sect. (3.1), the Hamiltonian of the system depends crucially on the geometry of the external trapping potential. For the case of a harmonic trap, r_1 is typically much greater than r_2 and r_3 and the terms corresponding to r_i for $i > 3$ are even smaller. However, for trap potentials of the form $|x|^\gamma$, with $\gamma \approx 0.5$, one obtains a situation when $r_1 \approx r_2 \gg r_3$. This latter case can be used for implementing both one qubit and two qubit gates, as will be shown in the following sections.

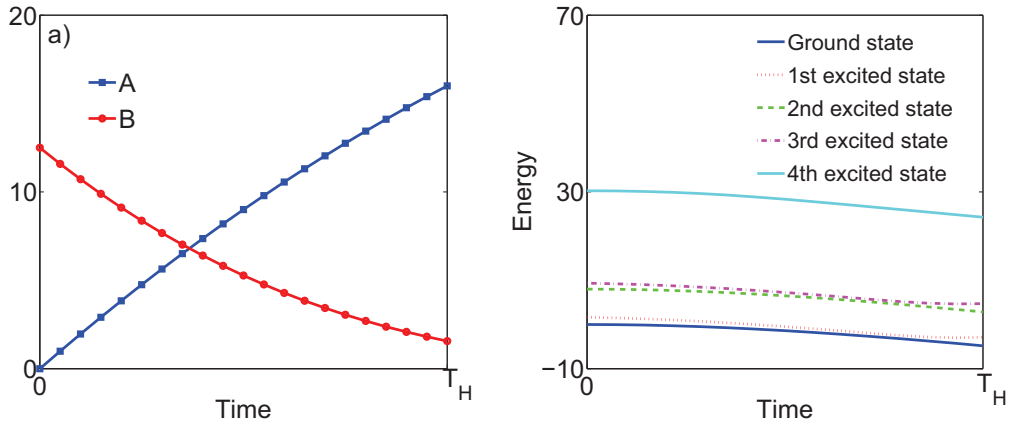

Figure 3.2: a) The one-qubit $\mathcal{H}$ gate and the two qubit Bell gate are implemented by an adiabatic change of the external fields in the Hamiltonian Eq. (3.2). We plot the fields $A(t)$, $B_1(t) = 10^{-5}B(t)$ and $B_2(t)\lambda = 10^{-6}B(t)$ in units of $1/\lambda$. T_H corresponds to the time at which the fidelity of the $\mathcal{H}$ gate reaches its maximum when the parameter $r_3 = 0$ in Eq. (3.2). The adiabaticity condition requires $T_H \gg 7 \times 10^6 \hbar/\lambda$. b) Distribution of the five lowest energy levels of the Hamiltonian Eq. (3.2) for the time evolution given in Fig. a). Note that in the figure, the energy gap between the ground state and the first excited state, as well as that for the second excited and third excited state, are scaled up by a factor of 300 for better visibility.

We implement the qubits as patterns of the spin system, where we define the $|0\rangle$ as the configuration for all spins 'up', and det 1 as all spins 'down',

$$|0\rangle = |\uparrow ... \uparrow\rangle \quad |1\rangle = |\downarrow ... \downarrow\rangle\,, \tag{3.5}$$

Initially, we fix the parameters of the external fields in such a way, that the four lowest energy levels at $t = 0$ are given by

$$\begin{aligned} |G(0)\rangle &= |\uparrow\uparrow\uparrow\uparrow\uparrow\uparrow\uparrow\uparrow\rangle\,, \quad |E_1(0)\rangle = |\downarrow\downarrow\downarrow\downarrow\downarrow\downarrow\downarrow\downarrow\rangle\,, \\ |E_2(0)\rangle &= |\uparrow\uparrow\uparrow\uparrow\downarrow\downarrow\downarrow\downarrow\rangle\,, \quad |E_3(0)\rangle = |\downarrow\downarrow\downarrow\downarrow\uparrow\uparrow\uparrow\uparrow\rangle\,, \end{aligned} \tag{3.6}$$

where G denotes the ground state and E_1, E_2 and E_3 the first, second and third excited state. Starting from the initial configuration given in eq. (3.6), the qubit gates are performed by adiabatically changing the external fields.

3.2.2 Gate implementations

The gates are implemented through an adiabatic evolution of the system Hamiltonian. The quantum adiabatic theorem [Born and Fock, 1928, Messiah, 1958] states, that a physical system that is initially in one of its nondegenerate eigenstates will remain in the corresponding instantaneous eigenstate, provided that the Hamiltonian is varied sufficiently slowly. Likewise, a superposition of different eigentstates results in a superposition of the adiabatically transferred states. The adiabatic transfer gives rise to a phase Φ, that is composed of the dynamical and the Berry phase [Pancharatnam, 1956, Berry, 1984, Shapere and Wilczek, 1998, Messiah, 1958], such that

$$|G(0)\rangle \to e^{i\Phi_0}\,|G(T)\rangle \quad |E_1(0)\rangle \to e^{i\Phi_1}\,|E_1(T)\rangle \quad ... \tag{3.7}$$

Here, $\to$ denotes the adiabatic time evolution. The phases Φ_i are given by the sum of the dynamical and Berry phases for the corresponding eigenstates. The eigenvectors of the Hamiltonian that are relevant in our gate transformations are all real in at least one basis. Consequently, the corresponding Berry phases vanish. Therefore, the total phase is given by the dynamical phase:

$$\Phi_i = -\int_0^T E_i(t)dt, \quad i = 0, 1, 2, \ldots. \tag{3.8}$$

The gate transformations are performed by adiabatic passage from an initial state $|\Psi(0)\rangle$ to a final state at $|\Psi(T)\rangle$, where the time evolution is given by the time

dependent Schrödinger equation 3.3. The input state of the gate is determined by the initial spin patterns at $t = 0$, whereas the output of the gate is determined by the spin patterns at the time $t = T$.

One-qubit gate:
We implement a one-qubit gate which is, up to a phase, equal to the Hadamard gate eq. 2.1 and which we denote by $\mathcal{H}$. The gate transformation reads

$$|0\rangle \rightarrow |+\rangle\,, \quad |1\rangle \rightarrow -\,|-\rangle \tag{3.9}$$

To demonstrate the gate transformation for the $\mathcal{H}$-gate defined in eq. (3.9), we use a qubit encoding in which each qubit consists of eight spins:

$$|0\rangle = |G(0)\rangle = |\uparrow\uparrow\uparrow\uparrow\uparrow\uparrow\uparrow\uparrow\rangle \quad |1\rangle = |E_1(0)\rangle = |\downarrow\downarrow\downarrow\downarrow\downarrow\downarrow\downarrow\downarrow\rangle \tag{3.10}$$

To implement the $\mathcal{H}$ gate, a qubit that is initially in the state $|\Psi(0)\rangle = a_0\,|0\rangle + a_1\,|1\rangle$ should evolve into the $\mathcal{H}$ rotated state

$$|\Psi_{\mathcal{H}}\rangle = a_0\frac{|G(0)\rangle + |E_1(0)\rangle}{\sqrt{2}} - a_1\frac{|G(0)\rangle - |E_1(0)\rangle}{\sqrt{2}}, \tag{3.11}$$

where a_0 and a_1 are complex numbers, with $|a_0|^2 + |a_1|^2 = 1$. Using the encoding in Eq. (3.10) for the input state, the adiabatic time evolution is given by

$$|\Psi(0)\rangle = a_0\,|G(0)\rangle + a_1\,|E_1(0)\rangle \rightarrow |\Psi(T)\rangle = a_0 e^{i\Phi_0}\,|G(T)\rangle + a_1 e^{i\Phi_1}\,|E_1(T)\rangle\,. \tag{3.12}$$

Our aim is to change the fields in such a way, that the time evolved state $|\Psi(T)\rangle = a_0 e^{i\Phi_0}\,|G(T)\rangle + a_1 e^{i\Phi_1}\,|E_1(T)\rangle$ is "as close as possible" to the $\mathcal{H}$ rotated state $|\Psi_{\mathcal{H}}\rangle$ given by eq. 3.11.

The measure of closeness is the fidelity of the gate, defined as the overlap between the required output state of the gate and the time evolved state, averaged over the Hilbert space of input states $|\phi\rangle$. For the $\mathcal{H}$-gate, the fidelity is given by

$$f_{\mathcal{H}} = \int d\,(|\phi\rangle)\,|\,\langle\Psi(T)|\Psi_{\mathcal{H}}\rangle\,|^2. \tag{3.13}$$

Two-qubit gate:
We implement the two-qubit Bell gate introduced in eq. (2.2). To demonstrate the implementation of the Bell gate, the encoding is given by

$$\begin{aligned} |00\rangle = |G(0)\rangle = |\uparrow\uparrow\uparrow\uparrow\uparrow\uparrow\uparrow\uparrow\rangle \quad |11\rangle = |E_1(0)\rangle = |\downarrow\downarrow\downarrow\downarrow\downarrow\downarrow\downarrow\downarrow\rangle \\ |01\rangle = |E_2(0)\rangle = |\uparrow\uparrow\uparrow\uparrow\downarrow\downarrow\downarrow\downarrow\rangle \quad |10\rangle = |E_3(0)\rangle = |\downarrow\downarrow\downarrow\downarrow\uparrow\uparrow\uparrow\uparrow\rangle \end{aligned} \tag{3.14}$$

The gate transformation is performed by adiabatic passage, where the initial state $|\Psi(0)\rangle = a_{00}|00\rangle + a_{11}|11\rangle + a_{01}|01\rangle + a_{10}|10\rangle$ should evolve into the Bell rotated state

$$|\Psi_{\text{Bell}}\rangle = a_{00}\frac{|G(0)\rangle + |E_1(0)\rangle}{\sqrt{2}} - a_{11}\frac{|G(0)\rangle - |E_1(0)\rangle}{\sqrt{2}} + a_{01}\frac{|E_2(0)\rangle + |E_3(0)\rangle}{\sqrt{2}} - a_{10}\frac{|E_2(0)\rangle + |E_3(0)\rangle}{\sqrt{2}}. \tag{3.15}$$

Using the encoding in Eq. (3.14), the adiabatic evolution is given by

$$\begin{aligned} |\Psi(0)\rangle = a_{00}|G(0)\rangle + a_{11}|E_1(0)\rangle + a_{01}|E_2(0)\rangle + a_{10}|E_3(0)\rangle \rightarrow \\ |\Psi(T)\rangle = a_{00}e^{i\Phi_0}|G(T)\rangle + a_{11}e^{i\Phi_1}|E_1(T)\rangle + a_{01}e^{i\Phi_2}|E_2(T)\rangle \\ + a_{10}e^{i\Phi_3}|E_3(T)\rangle . \end{aligned} \tag{3.16}$$

As for the $\mathcal{H}$-gate, the fidelity of the Bell gate is defined as the overlap between the time evolved state at $t = T$ and the Bell rotated state,

The fidelity thus reads

$$f_{\text{Bell}} = \int d\left(|\phi\rangle\right) |\langle\Psi(T)|\Psi_{\text{Bell}}\rangle|^2. \tag{3.17}$$

The integration is performed numerically using Monte Carlo methods. We compare the fidelity to the "classical" fidelity, which can be understood in the following context: Suppose that a quantum gate takes d level quantum systems at its input. Consider a situation where, instead of using the quantum gate, one uses the strategy of measuring the input (thus making the information in the quantum input as classical), and then preparing an output from the information obtained from the measurement on the input. The maximal fidelity that is obtainable in this way is said to be the classical fidelity of the gate. Note that the only parameter of the quantum gate that is used here is the dimension of the input space of the gate. The classical fidelity of a quantum gate that takes d level systems as its input is (see e.g. [Horodecki et al., 1999])

$$\frac{2}{d+1}.$$

Let us now consider the time evolution of the system.

3.2.3 Noise Resistance of the QNN

We study various noise models to demonstrate that our QNN model shows a high robustness to noise.

We first consider a model for distributed noise, i.e. noise that arises globally in the system. Second, we will discuss a "local noise", i.e. noise that acts as local perturbations.

In order to define the distributed noise, let us recall that the terms proportional to r_1, r_2, and r_3 in the quantum neural network Hamiltonian $H(t)$ eq. (3.2) stem from the first, second, and third vibrational modes of the trapped ion chain. For the case where $r_1 \approx r_2 \gg r_3$, one can consider the r_3 term as distributed noise in the system. This noise model is motivated by taking into account the following points:

(i) Increasing the effect of the third vibrational mode, which in the undisturbed case is much smaller than the first and second ones, covers inaccuracies in the trapping potential.

(ii) Moreover, decreasing the eigenfrequency of the third vibrational mode (i.e. increasing r_3) introduces a disturbance in the motion of the ions.

(iii) In addition, this introduces noise in the spin, as it is the phonon modes that are the carriers of interaction between the effective spins.

In Fig. 3.3, we plot the fidelity of the $\mathcal{H}$-gate (Fig. 3.3 a) and the Bell gate (3.3 b) as a function of time. Let us recall that the gates are implemented by adiabatically changing the system Hamiltonian. As time evolves, the initial state of the system is transformed towards the required output state of the gate. We consider the influence of distributed noise and show that even substantial increases in the noise level do not change the fidelity very much.

Let us now consider our model of local noise, which accounts for local perturbations to the state of the system. We study imperfections to the initial state of the system by superposing it with the states where one spin is flipped. Let us illustrate this for the "all down" state, $|\downarrow\downarrow\downarrow\downarrow\downarrow\downarrow\downarrow\downarrow\rangle$, where we consider the transformation

$$|\downarrow\downarrow\downarrow\downarrow\downarrow\downarrow\downarrow\downarrow\rangle \rightarrow |\downarrow\downarrow\downarrow\downarrow\downarrow\downarrow\downarrow\downarrow\rangle + \varepsilon\,|W_8\rangle\,, \tag{3.18}$$

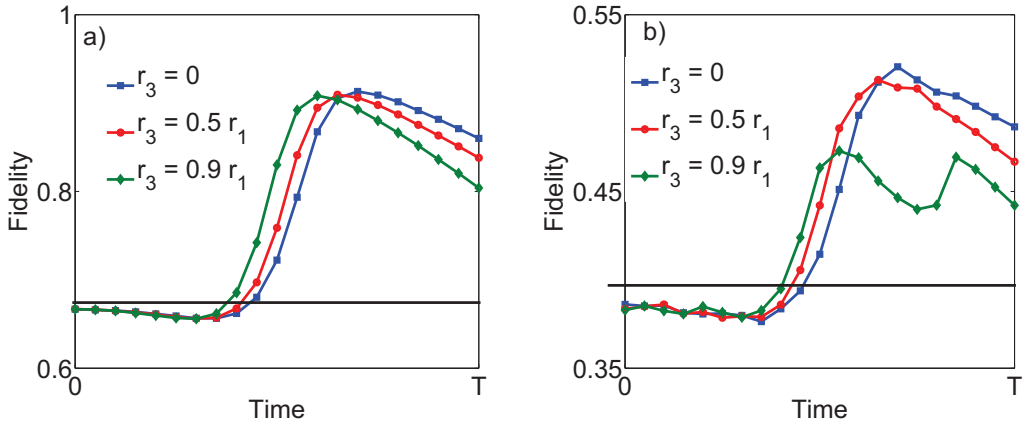

Figure 3.3: Fidelity of the one qubit $\mathcal{H}$ gate (a) and the two qubit Bell gate (b), implemented in a chain of trapped ions, as a function of time. The fidelities are shown for the indicated values of the global noise parameter r_3. The fidelity does not change appreciably with the increase of the distributed noise level r_3 up to $r_3 = 0.5r_1$ for the Bell gate (b) and $r_3 = 0.9r_1$ for the $\mathcal{H}$ gate (a). We use the parameters $r_1 = 10$, and $r_2 = 9.5$, and the (parallel and transverse) fields for which the calculations are performed are depicted in Fig. 3.2 a. The maximal fidelities are obtained shortly after $t = T/2$. T is a time that satisfies the adiabaticity condition Eq. (3.4), which with our chosen parameters means $T \gg 7 \times 10^6 \hbar/\lambda$. The dip in the fidelity curve for the Bell gate (b) around $t = 3T/4$ for the very high noise ($r_3 = 0.9r_1$) case, is due to the fact that the energy gap between the 1st excited state and the 2nd excited state becomes comparable to that between the 3rd and the 4th. The horizontal lines at 2/3 and 2/5 denote the limit above which the gate fidelity is quantum.

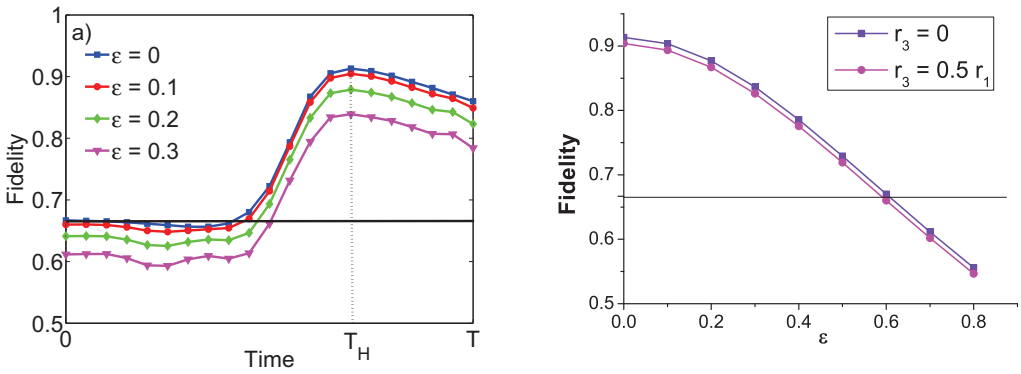

Figure 3.4: Fidelity of the one qubit $\mathcal{H}$ gate, as a function of time: a) Effect of local noise. The fidelities are calculated for $r_1 = 10$, $r_2 = 9.5$, and $r_3 = 0$, for the indicated values of the local noise parameter ε. The maximal fidelities are obtained a little after $t = T/2$, where T is a time that satisfies the adiabaticity condition Eq. (3.4), which with our chosen parameters mean $T \gg 7 \times 10^6 \hbar/\lambda$. The fidelity does not decrease dramatically as the level of local noise ε increases. b) Combined effect of distributed and local noise. We plot the maximal fidelity at T_H of the $\mathcal{H}$ gate as a function of the local noise parameter ε for the indicated values of the parameter of distributed noise r_3. The horizontal line at 2/3 denotes the limit above which the gate fidelity is quantum.

as a model of noise. Here $|W_8\rangle$ is the eight spin W-state, defined as the normalized symmetric superposition of all states with one spin up and the rest spins down [Dür et al., 2000]. The parameter ε is the strength of the perturbation.

In Fig. 3.4 a, we show the fidelity of the $\mathcal{H}$ gate for different levels of local noise. Again, we observe a high level of error resistance. Moreover, there is a large region of the time axis where the fidelity is larger than the classical limit $2/3 \approx 0.667$. In Fig. 3.4 b, we consider the two sources of noise simultaneously. We show that even substantially increasing both the noise levels does not affect the fidelity in a dramatic way.

In all the above figures, the curves for the fidelities have small curvatures at and around the positions of maximum fidelities. This implies that in an implementation of the presented protocols, small errors in the time of measurement do not affect the gate fidelities appreciably.

Let us note that the gate fidelities as shown in Figs. 3.3 and 3.4 are for the case

when $r_1 \approx r_2 \gg r_3$. This requirement cannot be met in a harmonic confinement of the ions. However, many experimental setups use harmonic confinement, in which case one has $r_1 \gg r_2, r_3$. Let us note that one can implement a noise resistant $\mathcal{H}$ gate in such a trap, whereas the implementation of two qubit gates is not possible [Pons et al., 2007, Braungardt et al., 2007].

The time at which the maximal gate fidelity is reached is denoted by T_H: The maximal fidelities of both the gates are attained approximately at the same point of time. The avoided crossing is approximately at $3T_H/4$. Adiabaticity demands that

$$T_H \gg 7 \times 10^6 \frac{\hbar}{\lambda}. \tag{3.19}$$

3.3 Summary and Outlook

In this chapter, we have proposed the implementation of a neural-network-like device for the manipulation of classical and quantum information, where we make use of the many-body properties of a chain of trapped ions. The trapped ions allow for the realization of an effective spin 1/2 system with long-range interactions mediated by the vibrational modes.

We have shown that a Hopfield-like classical neural network can be implemented, where certain spin patterns can be stored with high robustness to spin flips.

Furthermore, we have analyzed a neural-network-like system for the processing of quantum information. The qubits are encoded in the low energy levels of the whole system. The realizations of one and two qubit quantum gates occurs via adiabatic passage of the system from a set of energy eigenstates to another set of corresponding eigenstates. The adiabatic transfer is effected by a slow change of parallel and transverse fields.

We have shown that the system is robust to a high level of local noise as well as globally distributed noise. We have thus achieved an error resistance that is intrinsic to the system.

However, the scalability to larger systems is typically challenging for ions in a trap. One way towards scalable quantum neural network models would be to increase the number of ions in the trap. In this context, segmented trap

designs [Kielpinski et al., 2002] or microtrap arrays [Chiaverini and Lybarger, Jr., 2008,Schmied et al., 2009] could be potential candidates. Another way to achieve scalable complex quantum systems with metastable states useful for quantum information processing could be to design implementations with atoms in optical lattices.

It has been shown [Menotti et al., 2007, Trefzger et al., 2008] that using dipolar atoms or molecules in optical lattices, a large number of metastable states can be achieved. A controlled transfer between different states can be achieved by going to the superfluid region of the phase diagram. Such systems are therefore promising candidates for distributed quantum information processing, where the information could be stored in the metastable states, and simple quantum gates could be performed by transferring between different states.

Chapter 4

Detection of Quantum Systems via Particle Counting

Photon counting has been used as an important tool in quantum optics since its beginnings. Experimental access to the properties of a light field is typically achieved by measuring the number of photons that arrive at a photodetector during a given time interval.

The counting process is described by the interaction between the photons and the detector. One has to distinguish between counting in open and closed systems. In open systems, particles that are not absorbed at the detector typically propagate away, such that the back-action of the detector on the field is not relevant. For closed systems, the absorption of particles at the detector can significantly decrease the number of particles that is available for detection at later times and has to be taken into account.

Our aim is to use atom counting statistics for the detection of strongly correlated many-body systems, typically realized with atoms in optical lattices. In particular, we are interested in the detection of occupation patterns that could be used to realize a quantum neural network as discussed in the previous chapter. In order to describe experimentally relevant situations, we are interested in giving a full time- and space-dependent description of the counting process.

In the Sect. 4.1, we review some important results for the statistics of photon counting. In Sect. 4.2, we discuss the applicability of the formalism for photon

counting to describe atomic systems. In Sect. 4.3, we present our derivation of a formula for the counting distribution of time- and space-dependent fields.

4.1 Photon Counting

The detection of photons in a photodetector is based on the photoelectric effect: Light falls on the detector surface and the electrons that are released can be detected by placing a positively charged electrode near the photoemissive cathode and measuring the electric current that is generated in response to the incident light. The photoelectric current can be amplified by a photomultiplier. A similar process takes place in semiconductor detectors such as an avalanche photodiode. In order to give a theoretical description of the counting process, it is of fundamental interest to derive a formula for the probability of detecting a certain number m of photons during a time interval τ.

4.1.1 The Mandel Formula

A semiclassical formula for the probability $p(m)$ of counting m particles was first derived by Mandel, Sudarshan and Wolf in 1964 [Mandel et al., 1964], see also [W. E. Lamb and Scully, 1969]. The so called Mandel formula reads

$$p(m,t,\tau) = \langle \frac{1}{m!} (\int_t^{t+\tau} \mathcal{I}(t')dt')^m \exp(-\int_t^{t+\tau} \mathcal{I}(t')) \rangle, \tag{4.1}$$

where the intensity $\mathcal{I} = \int_\Omega \epsilon V^*(\mathbf{r},t)V(\mathbf{r},t)d\mathbf{r}$ is defined in terms of the analytic signal $V(\mathbf{r},t)$, where the integration is performed over the detector volume Ω and ϵ denotes the quantum efficiency of the detector. Here, the field is treated as classical and the photoelectrons are treated quantum mechanically. Essentially, the field can be seen as an external potential disturbing the bound electrons in the photocathode.

4.1.2 The Glauber-Mandel Formula

A quantum version of the formula for the photon counting distribution was first derived from semiclassical arguments by Mandel [Mandel, 1958, Mandel, 1959,

Mandel, 1963]. A full quantum mechanical derivation of the so called Glauber-Mandel formula was presented by Kelley and Kleiner in 1964 [Kelley and Kleiner, 1964] and by Glauber in 1965 [Glauber, 1965]:

$$p(m,t,\tau) = \langle \mathcal{T} : \frac{(\epsilon \int_t^{t+\tau} \hat{\mathcal{I}}(t')dt')^m \exp(-\epsilon \int_t^{t+\tau} \hat{\mathcal{I}}(t'))}{m!} : \rangle \tag{4.2}$$

Here $\mathcal{T}$ and :: stand for time and normal ordering, respectively. The intensity operator $\hat{\mathcal{I}}(t)$ is defined in terms of the positive and negative frequency parts $\hat{V}^{\pm}(\mathbf{r},t)$ of the field operators by $\hat{\mathcal{I}}(t) = \int_D \hat{V}^-(\mathbf{r},t)\hat{V}^+(\mathbf{r},t)d\mathbf{r}$. The normal ordering reflects the fact that the photons are annihilated at the detector. For a single mode field, the formula reads

$$p(m,\tau) = \sum_{n=m}^{\infty} \binom{n}{m} (\epsilon\tau)^m (\exp(-\lambda\tau))^{n-m} \langle n|\rho|n\rangle. \tag{4.3}$$

The derivation of the Glauber-Mandel formula is based on a perturbative approach for short detection intervals. The counting distribution for the full detection time τ is obtained by dividing it into small subintervals $\Delta\tau_i$ and treating the measurement in the full interval as a number of successive independent measurements in each interval. The approach thus describes a sequence of measurements, where the field evolves as in the absence of the detector. The method is based on the assumption, that the detection in one subinterval is independent of the detection in the previous subintervals. For the case of a light beam falling on a photo detector, it is argued [Mandel and Wolf, 1995, p. 723] that each element of the optical field interacts with the detector only briefly. The response time of the detector is short and the energy of the electron state is well defined (each electron is either free or bound) after an interaction time $\Delta\tau_i$. For such a system where the unabsorbed photons escape, there is no need to consider the measurement back-action.

The Glauber-Mandel formula does not apply to closed systems. In this case, the light interacts continuously with the detector and the back-action of the detector on the field has to be taken into account, as the total number of particles decreases due to the absorption process. There has been some confusion [Srinivas and Davies, 1981, Mandel, 1981, Srinivas and Davies, 1982] about the applicability of the Glauber-Mandel formula (4.2) and it is important to keep in mind, that it describes open quantum systems where the detector does not change the field. In particular, the Glauber-Mandel formula becomes meaningless if $\epsilon\tau \gg 1$, when it

can result in negative probabilities or unlimited mean number of counted photons as t tends to infinity. These limitations of the Glauber-Mandel formula were first pointed out by Mollow [Mollow, 1968]. However, note that ϵ denotes the efficiency per atom, which means that for systems with large numbers of particles the Glauber-Mandel formula typically gives a reasonably well approximation for the usual detection times.

4.1.3 The Back-action of the Detector on the Field

A formula taking into account the back-action of the detector on the field was derived by considering the evolution of the system composed of the detector and the field [Mollow, 1968, Scully and W. E. Lamb, 1969, Selloni et al., 1978]. Using different approaches, the authors arrive at the result of a photon counting formula for a single-mode free field,

$$p(m,t,\tau) = \sum_{n=m}^{\infty} \binom{n}{m} (1-e^{-\epsilon\tau})^m (\exp(-\epsilon\tau))^{n-m} \langle n|\rho|n\rangle. \tag{4.4}$$

The formula is formally equivalent to the Glauber-Mandel formula for a single-mode free field, eq. (4.3). However, the term $\epsilon\tau$ is substituted by $1-e^{\epsilon\tau}$. For $\epsilon\tau \ll 1$, the two formulas are equivalent. The formula in eq. (4.4) does not exhibit the problems that were outlined for the Glauber-Mandel formula. The mean number of photons counted is bounded for $\tau \to \infty$ and no negative probabilities occur.

In 1981, Srinivas and Davies present an approach to photon counting [Srinivas and Davies, 1981] based on continuous measurements over an extended period of time. In particular, they apply the theory of continuous measurement to the problem of photon counting of a single mode field and obtain the formula in eq. (4.4), which was previously derived in [Mollow, 1968, Scully and W. E. Lamb, 1969, Selloni et al., 1978]. In contrast to the former derivations, they derive the counting formula from a full quantum mechanical description of the measurement process at the detector. In their approach, the coupling is assumed to be sufficiently small, such that in an infinitesimal time interval, at most one photon is detected. They thus define a one-count superoperator to describe the absorption of photons at the detector,

$$J\rho = \beta a \rho a^\dagger, \tag{4.5}$$

where β characterizes the coupling between the detector and the field. Between the counts the density operator evolves according to the no-count superoperator S_t

$$S_t\rho = \exp\left(-i\omega + \frac{\beta}{2}a^\dagger a t\right)\rho \exp\left(i\omega - \frac{\beta}{2}a^\dagger a t\right) \tag{4.6}$$

After measuring an event corresponding to one of the operators J (one-count) or S (no-count), the density operator is $\rho(t') = J\rho(t)/\mathrm{Tr}(J)$ and $\rho(t') = S\rho(t)/\mathrm{Tr}(S)$, respectively. Here t denotes the time before the measurement, and t' the time after the measurement.

Whereas the operators J and S are postulated in the model by Srinivas and Davies (SD model), Imoto and coworkers derived a microscopic theory of the continuous measurement of the photon number [Imoto et al., 1990]. The no-count and one-count operators are derived microscopically, taking into account the interaction of the photons with the detector using the Jaynes-Cumming Hamiltonian for the field of a two-level atom. They identify the parameter β in (4.5) as $\beta = g^2(t-t')$, where g describes the atom-field coupling.

The dynamics of the counting process described by the one-count and no-count operators can be described by the master equation

$$\dot{\rho} = \varepsilon\hat{a}\rho\hat{a}^\dagger - \frac{\varepsilon}{2}\hat{a}^\dagger\hat{a}\rho - \frac{\varepsilon}{2}\rho\hat{a}^\dagger\hat{a}, \tag{4.7}$$

where $a^\dagger$ and a are the creation and annihilation operator of the particle to be counted. Performing a rotation of the density matrix, $\rho(t) = e^{-\frac{\varepsilon}{2}t\hat{a}^\dagger\hat{a}}\tilde{\rho}(t)e^{-\frac{\varepsilon}{2}t\hat{a}^\dagger\hat{a}}$, and using the relation

$$e^{\gamma A}Be^{-\gamma A} = B + \gamma[A,B] + \frac{\gamma^2}{2!}[A,[A,B]] + ..., \tag{4.8}$$

we obtain

$$\dot{\tilde{\rho}}(t) = \varepsilon\hat{a}e^{\frac{-\varepsilon}{2}t}\tilde{\rho}\hat{a}^\dagger e^{\frac{-\varepsilon}{2}t} = \varepsilon e^{-\varepsilon t}\hat{a}\tilde{\rho}\hat{a}^\dagger. \tag{4.9}$$

This equation can be solved using perturbation theory such that, after transforming back the rotation, we obtain

$$\rho(t) = e^{-\frac{\varepsilon}{2}t\hat{a}^\dagger\hat{a}}(\tilde{\rho}(0) + \int_0^t \varepsilon e^{-\varepsilon t'}\hat{a}\tilde{\rho}(0)\hat{a}^\dagger + ...)e^{-\frac{\varepsilon}{2}t\hat{a}^\dagger\hat{a}}.$$

Using the cyclic properties of the trace, the probability $p(m,\tau)$ of counting m particles in the time τ can be written as

$$p(m,\tau) = \mathrm{Tr}[\rho(0)a^{\dagger m}\frac{(\int_0^\tau dt'\varepsilon e^{-\varepsilon t'})^m}{m!}e^{-\varepsilon t a^\dagger a}a^m].$$

This is equal to the normally ordered expression

$$p(m,\tau) = \langle : (1-e^{-\varepsilon\tau})^m \frac{(\hat{a}^\dagger \hat{a})^m}{m!} e^{-(1-e^{-\varepsilon\tau})\hat{a}^\dagger\hat{a}} : \rangle, \tag{4.10}$$

which holds because

$$\begin{aligned} : (\hat{a}^\dagger\hat{a})^m e^{-(1-e^{-\varepsilon t})\hat{a}^\dagger\hat{a}} : &= \hat{a}^{\dagger m} : e^{-(1-e^{-\varepsilon t})\hat{a}^\dagger\hat{a}} : \hat{a}^m \\ &= \hat{a}^{\dagger m} e^{-\varepsilon t \hat{a}^\dagger\hat{a}} \hat{a}^m. \end{aligned}$$

For a single mode field, eq. (4.4) is recovered.

In 2007, Dodonov et. al proposed an alternative model for photon counting [Dodonov et al., 2007] based on the SD model. As opposed to the model in Ref. [Srinivas and Davies, 1981], they define a one-count operator which does decrease the mean number of photons by exactly one, whereas the no-count operator leaves the number of photons constant.

In Ref. [Häyrynen et al., 2010], the results of the SD model and the model by Dodonov, denoted by E model, are analyzed by considering a detection model consisting of three parts: The light field to be measured, an atom, and the detector. The field is coupled to the atom with coupling constant g and the atom is coupled to the detector with coupling constant λ.

They numerically solve the master equation that describes the coupling and compare the results to the SD model as well as to the model proposed by Dodonov et al. They show how each of them is obtained as an asymptotic limit of the detection probability: The SD model coincides exactly with the solution of the master equation for $\lambda \gg g$, whereas the E model describes the average behavior of the field correctly for $g \gg \lambda$. They point out that in most of the practically relevant situations (e.g. photon counting with photomultiplier tubes), a strong atom-detector coupling ($\lambda \gg g$) can be assumed, such that the SD model gives a correct description.

It is interesting to note that the one-count measurement does not necessarily reduce the mean number of photons in the field. The mean number of photons immediately after a one-count process is given by

$$\langle n(t')\rangle = \mathrm{Tr}(\rho(t')a^\dagger a) = \langle n(t)\rangle - 1 + \frac{[\Delta n(t)]^2}{\langle n(t)\rangle}, \tag{4.11}$$

where $\Delta n(t) = n(t) - \langle n(t)\rangle$. From eq. (4.11) it is clear that the mean number of photons after the measurement depends on the photon statistics of the state

before the measurement. For a system originally in a Fock state, the factor $\frac{[\Delta n(t)]^2}{\langle n(t)\rangle}$ vanishes and the mean number of photons is reduced exactly by one. For an initial Poissonian statistics, the mean number of photons after the one-count process is equal to the one before the measurement. For a thermal state, the mean number of photons after the measurement doubles the mean number of photons of the pre-measurement state. This result is to some extend counterintuitive and has been addressed in Ref. [Ueda et al., 1990]. The authors observe that the apparent paradoxe is removed when taking into account the back-action of the detector on the field. They illustrate this with the simple example of the initial state $\rho = 1/2(|0\rangle\langle 0| + |100\rangle\langle 100|)$, with an average photon number of 50. When one photon is detected, the probability that the initial state was $|0\rangle\langle 0|$ vanishes. It can thus be concluded that the original state was $|100\rangle\langle 100|$ and that the state after the one-count process is $|99\rangle\langle 99|$, such that the mean photon number has increased by 49.

Recently, the action of the annihilation operator on different states of light has been implemented and measured experimentally [Parigi et al., 2007]. It was shown that a substraction of one photon from a thermal field state can increase the expectation value of the number of photons, as was theoretically predicted in Ref. [Ueda et al., 1990] using the SD model. In [Häyrynen et al., 2009], it is pointed out that the experimental results of Ref. [Parigi et al., 2007] agree with the prediction of the SD model. Their discussion is based on the observation [Häyrynen et al., 2009], that the experiment in [Parigi et al., 2007] can be applied to test the SD model even though the experimental detection scheme is different.

The previous discussion suggests, that the SD model is a valid description for the photon counting process based on continuous measurements. However, a closed formula, eq. (4.4), is derived only for the case of a single mode field. The application of the formula to real experimental situation is therefore limited [Mandel, 1981,Fleischhauer and Welsch, 1991]. In 1987, Chmara derived a general formula for the photon counting distribution for a multimode field [Chmara, 1987] by applying the photon counting approach by SD to an open system. He derives the so called Chmara counting formula,

$$p(m,t,\tau) = \langle : \frac{(\int_t^{t+\tau} \tilde{\mathcal{I}}(t')dt')^m}{m!} \exp(-\int_t^{t+\tau} \tilde{\mathcal{I}}(t')dt') : \rangle. \tag{4.12}$$

The formula is formally very similar to the Glauber-Mandel formula. However,

the time dependent intensities $\tilde{\mathcal{I}}(t)$ do not evolve according to the Heisenberg equation, but to a non-Hamiltonian evolution. While the formula is in principle applicable to a wide class of systems, to our knowledge, no practical case where the time dependent intensities have been calculated has been reported.

4.2 Atom Counting Formalism

We apply the theory of particle counting to study strongly correlated systems of atoms in optical lattices. The counting statistics of atoms depend on the kind of particles that are considered and on the type of measurement that is performed. In order to formally transfer the results for photon counting to the case of the detection of massive particles, the actual detection process has to be taken into consideration.

As was outlined in Chapter 2.4, the detection of atoms is typically achieved either directly using microchannel plates [Schellekens et al., 2005, Jeltes et al., 2007], or through the interaction with light, where the light is detected on a charge-coupled device (CCD).

In typical experimental situations, the atoms are either detected inside the optical lattice or in a time of flight measurement after their expansion from the lattice. The on-site detection has recently become available through fluorescence spectroscopy [Bakr et al., 2010, Sherson et al., 2010]. For spins, an on-site detection can be achieved by using QNDPS (see Chapter 2.4) to measure the distribution of $\hat{S}_z$, or even its spatially resolved version $\hat{S}_z^{eff}$ [Eckert et al., 2008]. Particle counting after a time of flight period can be achieved by absorption imaging, or by letting the particles fall on a microchannel plate.

Both for atom and for spin counting, the detection process is analogous to the one of photodetection: For atoms, detectors based on "absorption" or "destruction" of an atom (at the multichannel plate) are sensitive to normally and apex ordered correlation function of atomic creation and annihilation fields. The situation is the same in the spin measurements using QNDPS, since the spin lowering and raising operators couple directly to the photon annihilation and creation operators, respectively, which then are measured by the standard photodetectors.

Furthermore, one has to distinguish between bosons and fermions. For the case

of bosons, the results for photon counting can be transferred almost immediately. For the case of fermions, a similar formalism was established in [Cahill and Glauber, 1999].

Throughout our work, we use the formalism of generating functions, which was developed for bosons in [Glauber, 1965] and for fermions in [Cahill and Glauber, 1999]. In this formalism, the counting distribution is described by the derivatives of a generating function $\mathcal{Q}$,

$$p(m) = \frac{(-1)^m}{m!} \frac{d^m}{d\lambda^m} \mathcal{Q}\Big|_{\lambda=1}, \tag{4.13}$$

where the generating function is given by

$$\mathcal{Q}(\lambda) = \mathrm{Tr}(\rho : e^{-\lambda \mathcal{I}} :). \tag{4.14}$$

Here, $\mathcal{I}$ is the intensity of particles that are detected. As was discussed in the previous section, the intensity depends on the counting process. In the Glauber-Mandel formula eq. (4.2), the intensity evolves as in the absence of the detector. In the formulations by Srinivas and Davies, the absorption of particles at the detector is taken into account, however, the counting formula (4.4) does not include time- and space dependence. In order to correctly describe a given experimental situation, it is important to understand both the effect of the back-action of the detector and the time and space dependence.

The formalism is easily generalized to the case of detection with multiple detectors [Arecchi et al., 1966]. For detection with M detectors, the generating function reads

$$\mathcal{Q}_M(\lambda_1, \lambda_2, .., \lambda_M) = \mathrm{Tr}(\rho : e^{-\sum_i \lambda_i \mathcal{I}_i} :), \tag{4.15}$$

where $\mathcal{I}_i$ denotes the single detector intensity for at the ith detector. The counting distribution at each detector is calculated using eq.(4.13) For a configuration with two detectors, the joint probability distribution of counting m atoms in detector 1 and n atoms in detector 2 is given by

$$p(m,n) = \frac{(-1)^{m+n}}{m!n!} \frac{d^{m+n}}{d\lambda_1^m d\lambda_2^n} \mathcal{Q}_2\Big|_{\lambda_1=1,\lambda_2=1}. \tag{4.16}$$

We study the correlations $\mathrm{corr}(m,n)$ between the counting events detected at each detector by observing the ratio between the covariance and the single detector variances σ^2,

$$\mathrm{corr}(m,n) = \frac{\mathrm{cov}(m,n)}{\sigma^2(m)\sigma^2(n)}, \tag{4.17}$$

where $\mathrm{cov}(m,n) = \sum_{m,n} mnp(m,n) - \bar{m}\bar{n}$.

4.3 Particle Counting of Time and Space Dependent Fields

The time- and space-dependent counting process can be described by a master equation similar to eq. (4.7), where the operators $a, a^\dagger$ are replaced by the time dependent field operators $\Psi(\mathbf{r},t)$. Furthermore, we take into account the finite size of the detector, such that the interaction between the detector and the field is restricted to a given volume, which we describe by a function $\Omega(\mathbf{r})$. The master equation then reads

$$\dot{\rho}(t) = \epsilon \int d\mathbf{r}\Omega(\mathbf{r})\Psi(\mathbf{r},t)\rho\Psi^\dagger(\mathbf{r},t)$$
$$-\frac{\epsilon}{2}\int d\mathbf{r}\Omega(\mathbf{r})\Psi(\mathbf{r},t)^\dagger\Psi(\mathbf{r},t)\rho - \frac{\epsilon}{2}\int d\mathbf{r}\Omega(\mathbf{r})\rho\Psi(\mathbf{r},t)^\dagger\Psi(\mathbf{r},t). \tag{4.18}$$

The first term of Eq. (4.18) corresponds to the number of quantum jumps in the detector volume. The two remaining terms represent the damping of the field due to the absorption at the detector.

In order to solve the master equation eq. (4.18) we first eliminate the damping terms proportional to $\frac{\epsilon}{2}$ by defining the operator $\tilde{\rho}$ through

$$\rho(t) = F(t)\tilde{\rho}(t)F^\dagger(t), \tag{4.19}$$

where the operator $F(t)$ is defined as

$$F(t) = \mathcal{T}e^{-\epsilon/2\int_0^t dt' \int d\mathbf{r}'\Omega(\mathbf{r}')\Psi^\dagger(\mathbf{r}',t')\Psi(\mathbf{r}',t')} \tag{4.20}$$

Here, the term $\mathcal{T}$ on the left side of the operator denotes time ordering, whereas it denotes opposite time ordering on the right side of the operator.

We use the relation eq. (4.8) and the commutation relations

$$[\Psi(\mathbf{r},t),\Psi^\dagger(\mathbf{r}',t)] = \delta(\mathbf{r},\mathbf{r}'),\ \ [\Psi(\mathbf{r},t),\Psi^\dagger(\mathbf{r}',t')] = G_0(\mathbf{r},\mathbf{r}'|t,t'),\ \ [\Psi(\mathbf{r},t),\Psi(\mathbf{r}',t')] = 0.$$

where G_0 is the propagator for the time evolution of in absence of a detector,

$$\Psi(\mathbf{r},t) = \int d\mathbf{r}' G_0(\mathbf{r},t|\mathbf{r}',t_0)\Psi(\mathbf{r}',t_0) \tag{4.21}$$

to get the time derivative

$$\dot{\tilde{\rho}}(\mathbf{r},t) = \epsilon \int d\mathbf{r}'\Omega(\mathbf{r}')\tilde{\Psi}(\mathbf{r},t)\tilde{\rho}\tilde{\Psi}^{\dagger}(\mathbf{r},t), \tag{4.22}$$

where we have defined

$$\tilde{\Psi}(\mathbf{r},t) = F^{-1}(t)\Psi(\mathbf{r},t)F(t). \tag{4.23}$$

Eq. (4.22) can be solved using perturbation theory (note that $\tilde{\rho}(0) = \rho(0)$).

$$\begin{aligned}\tilde{\rho}(t) = \tilde{\rho}(0) + \epsilon \textstyle\int_0^t dt' \int d\mathbf{r}'\Omega(\mathbf{r}')\tilde{\Psi}(\mathbf{r}',t')\rho(0)\tilde{\Psi}^{\dagger}(x',t') \\ +\epsilon^2 \textstyle\int_0^t dt' \int_0^{t'} dt'' \int d\mathbf{r}' \int d\mathbf{r}''\Omega(\mathbf{r}')\Omega(\mathbf{r}'')\tilde{\Psi}(x',t')\tilde{\Psi}(x'',t'')\rho(0)\tilde{\Psi}^{\dagger}(x'',t'')\tilde{\Psi}^{\dagger}(x',t') + ...\end{aligned} \tag{4.24}$$

It is important to note that the perturbation theory is applied to the operator $\tilde{\rho}$, which take into account the damping of the field due to the absorption at the detector. In contrast, the Glauber-Mandel formula performs perturbation theory in terms of the operator ρ [Mandel and Wolf, 1995, p. 724]. This means that in the Glauber-Mandel formula, time is divided into short intervals which are treated as independent. The alteration of the field due to the absorption at the detector is neglected. In our treatment, the operators $\tilde{\Psi}(x',t')$ take into account the absorption. In order to get the probability distribution, we use the inverse of eq. (4.19) to transform $\tilde{\rho}$ in eq. (4.25) back to ρ. We use the cyclic properties of the trace to calculate the probability $p(m,\tau)$ of finding m particles in the detector opening time τ and get

$$\begin{aligned}p(m,\tau) = \langle \epsilon \int_0^{\tau} dt' \int_0^{t'} dt'' \int d\mathbf{r}' \int d\mathbf{r}''\Omega(\mathbf{r}')\Omega(\mathbf{r}'')... \\ ...\tilde{\Psi}^{\dagger}(x',t')\tilde{\Psi}^{\dagger}(x'',t'')...F^{\dagger}(\tau)F(\tau)...\tilde{\Psi}(x'',t'')\tilde{\Psi}(x'',t')\rangle\end{aligned} \tag{4.25}$$

In eq. (4.25) we have normal ordering with respect to the operators $\tilde{\Psi}$. In general, this does not imply normal ordering with respect to the operators Ψ, however, in our case they are linear combinations of $\tilde{\Psi}$ so the normal order is conserved.

The term $F^{\dagger}(\tau)F(\tau)$ is not normally ordered. We define a function $g(\Psi,\Psi^{\dagger},\tau)$ such that

$$F^{\dagger}(\tau)F(\tau) =: g(\Psi,\Psi^{\dagger},\tau) : . \tag{4.26}$$

Inserting eq. (4.26) into eq. 4.25, and using the requirement that the sum over the probabilities $p(m,\tau)$ has to be one, we get $g(\tilde{\Psi},\tilde{\Psi}^{\dagger}) = e^{-\epsilon \int dt \int d\mathbf{r}\Omega(\mathbf{r})\tilde{\Psi}^{\dagger}(\mathbf{r},t)\tilde{\Psi}(\mathbf{r},t)dt}$ and the probability distribution is given by

$$p(m,\tau) = \langle : \frac{(\mathcal{I}(\tau))^m}{m!} e^{-\mathcal{I}(\tau)} : \rangle, \tag{4.27}$$

where the intensity is given by

$$\mathcal{I}(\tau) = \epsilon \int_0^\tau dt \int d\mathbf{r}\Omega(\mathbf{r})\tilde{\Psi}^\dagger(\mathbf{r},t)\tilde{\Psi}(\mathbf{r},t) \tag{4.28}$$

In eq. (4.27) together with eq. (4.28), we have thus derived a formula for the counting distribution which is formally equal to the Glauber-Mandel formula eq. (4.2). However, eq. (4.27) is expressed in terms of the modified field operators $\tilde{\Psi}(\mathbf{r},t)$, which are related to the system operators $\Psi(\mathbf{r},t)$ by eq. (4.23). The difference between our counting formula eqs. (4.27) and (4.28) and the Glauber-Mandel formula arises due to the damping terms in the master equation (4.18), which are implicit in the modified field operators $\tilde{\Psi}(\mathbf{r},t)$. In order to calculate the counting distribution, the time evolution of the operators $\tilde{\Psi}(\mathbf{r},t)$ has to be expressed in terms of the system operators $\Psi(\mathbf{r},t)$.

Let us now derive an expression for the modified field operators $\tilde{\Psi}(\mathbf{r},t)$ given by eq. (4.23). Defining $\Delta t = t/N$, the time integration in the operator $F(t)$ in Eq. 4.20 can be written as a sum, such that

$$F(t) = \prod_i F^i(t_i), \tag{4.29}$$

with $F^i(t_i) = e^{-\frac{\epsilon}{2}\Delta t \int d\mathbf{r}'\Omega(\mathbf{r}')\Psi^\dagger(\mathbf{r}',t_i)\Psi(\mathbf{r}',t_i)}$, and we get

$$\tilde{\Psi}(\mathbf{r},t) = F^1(t_1)...F^N(t_N)\Psi(\mathbf{r},t)F^N(t_N)...F^1(t_1). \tag{4.30}$$

We evaluate the expressions by using the commutation relations eq. (4.3), the properties of the propagator eq. (4.21) as well as the relation eq. (4.8). We start with the inner term,

$$F^N(t_N)\Psi(\mathbf{r},t)F^N(t_N) = e^{-\frac{\epsilon}{2}\Delta t\Omega(\mathbf{r})}\Psi(\mathbf{r},t_N). \tag{4.31}$$

The second term thus reads

$$\begin{aligned} &e^{-\frac{\epsilon}{2}\Delta t\Omega(\mathbf{r})}F^{N-1}(t_{N-1})\Psi(\mathbf{r},t_N)F^{N-1}(t_{N-1}) = \\ &e^{-\frac{\epsilon}{2}\Delta t\Omega(\mathbf{r})}\int d\mathbf{r}' e^{-\frac{\epsilon}{2}\Delta t\Omega(\mathbf{r}')}G(\mathbf{r},\mathbf{r}',t_N - t_{N-1})\Psi(\mathbf{r}',t_{N-1}) \end{aligned} \tag{4.32}$$

The successive terms are calculated analogously, and we get

$$\tilde{\Psi}(\mathbf{r},t) = \int d\mathbf{r}' \left\langle \mathbf{r} \right| e^{-i(t-t_0)(H_0 + i\frac{\epsilon}{2}\Omega(\mathbf{r}'))} \left| \mathbf{r}' \right\rangle \Psi(\mathbf{r}',t_0). \tag{4.33}$$

We have thus obtained an expression for the modified field operators $\tilde{\Psi}\mathbf{r}, t)$ in terms of the operators $\Psi(\mathbf{r}', t_0)$. Together with the counting formula eq. (4.27), this allows us, in principle, to calculate the counting distribution for time dependent systems with arbitrary detector geometries. However, solving eq. (4.33) is in general a highly non-trivial task.

In the following chapters, we will encounter various experimental situations, where the detection process is fast compared to the time evolution of the system. In this case, we can neglect the part corresponding to the Hamiltonian H_0 in eq. (4.33) and get

$$\begin{aligned}\tilde{\Psi}(\mathbf{r}, t) &= \int d\mathbf{r}' \, \langle \mathbf{r}| \, e^{-\frac{\epsilon}{2}\Omega(x'))(\tau - t_0)} \, |\mathbf{r}'\rangle \, \Psi(\mathbf{r}', t_0) \\ &= e^{-\frac{\epsilon}{2}\Omega(x)(t-t_0)}\Psi(\mathbf{r}', t_0). \end{aligned} \tag{4.34}$$

The intensity (4.28) thus reads

$$\mathcal{I}(\tau) = \lambda \int d\mathbf{r}(1 - e^{-\epsilon\Omega(\mathbf{r})\tau})\Psi^\dagger(\mathbf{r}, t_0)\Psi(\mathbf{r}, t_0), \tag{4.35}$$

which is a generalization of the formula eq. (4.10) considering finite detector volumes. For $\epsilon\tau \ll 1$, eq. (4.35) reduces to the Glauber-Mandel formula eq. (4.2) for time independent systems.

In the remaining part of the thesis we apply the counting formalism discussed in this chapter to a wide range of systems of atoms in optical lattices. Here, we distinguish between systems whose dynamics are on the time scale of the counting process and such systems, which evolve slowly compared to the counting process, such that they can be treated as time independent.

In Chapter 5, we consider the detection of strongly-correlated systems of fermions and spins in an optical lattice by particle counting. We show that the counting statistics allow for the detection of quantum-many-body effects such as a quantum phase transition and fermion pairing. We show that the method is successful even at finite temperature. Furthermore, we study the time evolution of the system when coupled to a heat bath. The dynamics of the thermalization are slow compared to the detection process, such that the counting distribution is described by the time formalism of Srinivas and Davies.

In Chapter 6, we consider the counting of particles after their expansion from the lattice. The particles are released and fall onto a spatially confined detector. We

show that by choosing appropriate detector geometries, the counting distribution in principle allows for the characterization of different metastable states of the system. The detection process is typically short compared to the dynamics of the expansion, such that the detection of the expanding atoms takes place momentarily and the generalization of the formalism of Srinivas and Davies to finite detectors can be applied.

In Chapter 7, we illustrate the full time dependent formalism developed in Sect. 4.3 by applying it to the detection of an expanding Bose-Einstein-condensate. We analyze the effect of the back-action of the detector on the field by comparing the counting distribution obtained by the applying the time-dependent formalism to the Glauber-Mandel formula.

Chapter 5

Counting of Fermions and Spins in Strongly Correlated Systems

In this chapter, we apply the method of particle counting to study the detection of the system of strongly correlated fermions in an optical lattice described by the Hamiltonian eq. (2.13),

$$\hat{H} = -J\sum_{j=1}^{N}(\hat{c}_j^\dagger\hat{c}_{j+1} + \gamma\hat{c}_j^\dagger\hat{c}_{j+1}^\dagger + h.c. - 2g\hat{c}_j^\dagger\hat{c}_j + g). \tag{5.1}$$

As was discussed in Sect. 2.3.4, the system exhibits rich many-body behavior such as a quantum phase transition and the formation of fermion Cooper-like pairs. The system is equivalent to the anisotropic XY-spin-model.

We consider the detection of the particles in-situ in the lattice. For the fermionic system, a detection process with single site resolution in the spirit of the experiments in [Sherson et al., 2010, Bakr et al., 2010] could be applied. For the spin system, the spin counting could be performed via quantum nondemolition polarization spectroscopy (see Sect. 2.4.5).

In Sect. 5.1, we consider the counting statistics of a system at zero temperature and show that particle counting allows for the detection of these many-body phenomena.

In real experimental situations, the detection of these many-body quantum properties is always obscured by unavoidable noise and thermal effects. The effects of temperature are of particular interest, as quantum phase transitions are only well

defined at zero temperature. Thermal fluctuations lead to an exponential decay of the order parameter and only a crossover between phases remain [Sachdev, 2001]. In Sect. 5.2, we analyze the effects of temperature on the system. We show that even at finite T, the counting statistics reflect the signature of the quantum phase transition. Furthermore, we show that the breaking of fermion pairs by thermal fluctuations is observed in the counting distribution.

In Sect. 5.3, we to study the dynamics of the system during the thermalization. The remarkably long time scales in ultracold atom experiments allow to monitor the dynamics of the system directly. We study the atom counting statistics during a dynamic evolution, where the system is subject to some perturbation and then approaches a stationary state. In this context various fundamental questions can be addressed. For instance, does the system, which can be very well regarded as closed, thermalize after initial perturbation (sudden quench) [Deng et al., 2010, Cramer et al., 2008, Manmana et al., 2007, Sengupta et al., 2004, Bañuls et al., 2010]? What is the difference between thermal and non thermal dynamics? What kinds of interesting dynamical processes involving a coupling to a specially designed heat bath can be realized? Can one realize state engineering using open system dynamics [Diehl et al., 2008, Kraus et al., 2008, Verstraete et al., 2009]? In particular, we compute the atom counting distributions as a function of time when the analyzed 1D system of fermions approaches the quantum Boltzmann-Gibbs thermal equilibrium state at certain $T > 0$. We show how the thermalization process can be monitored by observing the cumulants of the counting distribution. In principle, the methods allows thus to distinguish thermal dynamics from non-thermal one. The time evolution during thermalization is much slower than the counting process. This allows us to apply the formalism eq. (4.10) developed by Srinivas and Davies.

5.1 Counting Statistics at Zero Temperature

We consider a system of strongly correlated fermions described by the Hamiltonian eq. (5.1), which is equivalent to the anisotropic quantum XY-model eq. (2.11). The system exhibits a quantum phase transition at $T = 0$. Furthermore, the term proportional to γ in the Hamiltonian eq. (5.1) describes the formation of fermionic pairs between consecutive sites. In this section, we study these quan-

tum phenomena by particle counting for an ideal system at zero temperature. We show that that the counting distribution and its moments reflect the quantum phase transition as well as the pair formation. Finite temperature effects are discussed in the following section.

5.1.1 The Counting Distribution at T=0

Let us now derive the counting distribution for the system described by eq. (5.1). The Hamiltonian (5.1) does not depend on time, such that the counting distribution is obtained by eq. (4.10), which for a system of N fermions reads

$$p(m,\tau) = \langle : \frac{(\kappa \sum_{j=1}^{N} \hat{c}_j^\dagger \hat{c}_j)^m}{m!} e^{-\kappa \sum_{j=1}^{N} \hat{c}_j^\dagger \hat{c}_j} : \rangle, \tag{5.2}$$

The counting distribution eq. (5.2) can be written in a compact way using the formalism of generating functions eq. (4.13),

$$p(m) = \frac{(-1)^m}{m!} \frac{d^m}{d\lambda^m} \mathcal{Q}\Big|_{\lambda=1}, \tag{5.3}$$

where $\mathcal{Q}$ is given by

$$\mathcal{Q}(\lambda) = \mathrm{Tr}(\rho : e^{-\lambda \mathcal{I}} :) \tag{5.4}$$

and

$$\mathcal{I} = \kappa \sum_j \hat{c}_j^\dagger \hat{c}_j \tag{5.5}$$

The intensity $\mathcal{I}$ describes the intensity of fermions that are registered during the detection process. In the following, we express the local fermi operators $\hat{c}_l$ in terms of their Fourier transforms $\hat{c}_k$ and finally in terms of the Bogoliubov excitations $\hat{d}_k$. This way, the the system Hamiltonian eq. (5.1) is diagonal and the trace in eq. (5.4) can be calculated easily. However, note that the particles that are actually detected are the local fermions described by the operators $\hat{c}_l$.

Let us now write the generating function in terms of the operators $\hat{c}_k$ in momentum space and use the anticommutation relations for fermions to obtain

$$\mathcal{Q}(\lambda) \;=\; \mathrm{Tr}(\rho \prod_{k=1}^{N/2} (1 - \lambda\kappa \hat{c}_k^\dagger \hat{c}_k)(1 - \lambda\kappa \hat{c}_{-k}^\dagger \hat{c}_{-k})). \tag{5.6}$$

We express eq. (5.6) in terms of the fermionic excitations d_k defined in eq. (2.18). The dynamics mix only k and $-k$ fermionic excitations and the density matrix ρ can be written as $\rho = \prod_k \rho_k$, such that we obtain

$$\mathcal{Q}(\lambda) = \prod_{k=1}^{N/2} \big(1 - \lambda\kappa A_k + \lambda^2\kappa^2 B_k\big), \tag{5.7}$$

where

$$\begin{aligned} A_k &= \mathrm{Tr}(\rho_k \left[u_k^2 \hat{n}_k^d + v_k^2(\hat{d}_k\hat{d}_k^\dagger + \hat{d}_{-k}\hat{d}_{-k}^\dagger)\right]) \\ B_k &= \mathrm{Tr}(\rho_k \left[u_k^2 \hat{d}_k^\dagger\hat{d}_k\hat{d}_{-k}^\dagger\hat{d}_{-k} + v_k^2\hat{d}_{-k}\hat{d}_{-k}^\dagger\hat{d}_k\hat{d}_k^\dagger\right]). \end{aligned} \tag{5.8}$$

We have omitted the terms that do not conserve the particle number, as they do not appear in the trace.

Using (5.3), the counting distribution reads

$$p(m) = \frac{(-1)^m}{m!}\frac{d^m}{d\lambda^m}\Big[\prod_{k=1}^{N/2}\big(1 - \lambda\kappa A_k + \lambda^2\kappa^2 B_k\big)\Big]_{\lambda=1}. \tag{5.9}$$

We derive a recurrence relation to calculate the distribution for $(M+1)$ modes, given the distribution for M modes by using the generalized Leibniz rule,

$$\begin{aligned} &\frac{d^m}{d\lambda^m}\prod_{k=1}^{N} f_k(\lambda) \\ &= \sum_{n_1+\ldots+n_N=n} \binom{n}{n_1, n_2, ..., n_N} \prod_{k=1}^{N} \frac{d^{n_k}}{d\lambda^{n_k}} f_k(\lambda), \end{aligned}$$

where the generalized Newton's symbol is given by

$$\binom{n}{n_1, n_2, ..., n_N} = \frac{n!}{n_1!n_2!...n_N!}.$$

The distribution function $p(m, M)$ for M modes is given by

$$p(m,M) = \frac{(-1)^m}{m!}\sum \frac{m!}{l_1!l_2!...l_N!}\prod_{j=1}^{M/2}\frac{d^{l_j}}{d\lambda^{l_j}}(1 - 2\lambda\kappa v_k^2 + \lambda^2\kappa^2 v_k^2), \tag{5.10}$$

where the summation runs over $l_1, \ldots, l_M$ such that $l_1 + \cdots + l_M = m$, where $l_j = 0$, 1, or 2, for $j = 1, \ldots, M$. We can now derive the recursive relation

$$p(m, M+1) = \sum_{i=0}^{2} \mathcal{P}_i p(m-i, M) \tag{5.11}$$

where

$$\begin{aligned}\mathcal{P}_0 &= 1 - \kappa A_{M+1} + \kappa^2 B_{M+1},\\ \mathcal{P}_1 &= \kappa A_{M+1} - 2\kappa^2 B_{M+1},\\ \mathcal{P}_2 &= 1 - \mathcal{P}_0 - \mathcal{P}_1 \end{aligned} \tag{5.12}$$

are the probabilities of detecting 0,1, or 2 particles in the modes $M+1$ and $N-M-1$. Using the recursive relation eq. (5.11), the counting distribution for an arbitrarily large system can be calculated from the counting distributions of a two mode system. We thus only need to calculate the expressions A_k and B_k in eq. (5.8) and use Eqs. (5.11) and (5.12) to obtain the counting distributions of the fermionic system eq.(5.1) with an arbitrary number of sites.

We obtain a better understanding of the properties of the counting distributions by looking at the mean and variance. We derive a recurrence relation for the mean and variance from the recurrence relation given in eq. (5.11):

$$\overline{m_{M+1}} = \overline{m_M} + 2\kappa v_{M+1}^2, \tag{5.13}$$

$$\begin{aligned}\sigma_{M+1}^2 &= \overline{m_{M+1}^2} - \overline{m_{M+1}}^2\\ &= \sigma_M^2 + 4\kappa^2 v_{M+1}^2 (1 - v_{M+1}^2)\end{aligned} \tag{5.14}$$

The relation (5.13) is obtained by multiplying both sides of the recurrence (5.11) by m, summing over m, and performing some further simple algebraic manipulations. Relation (5.14) is obtained similarly by a multiplication of m^2 on both sides of eq. (5.11). Since $\overline{m_1}$ and σ_1^2 can be trivially calculated, the mean and variance can be obtained by these relations for an arbitrary number of modes. The recurrences imply that the mean $\overline{m_N} \leq \kappa N$; we find the typical value of $\overline{m_N}$ indeed to be of order of κN. On the other hand, the variance $\sigma_N^2 \leq \kappa^2 N$. Both quantities show singular behavior in the thermodynamical limit at criticality. In particular, for the transverse Ising model ($\gamma = 1$), near the critical point $g = g_c \equiv 1$, the mean $\overline{m}$ can be written in terms of elliptic integrals of first and second kind, and can be expressed as [Gradshteyn and Ryzhik, 2000] (see [Sachdev, 2001, Barouch et al., 1970] and references therein)

$$\overline{m} \approx -\frac{1}{2\pi}(g - g_c)\ln|g - g_c| - \frac{1}{\pi},$$

so that

$$d\overline{m}/dg \approx -(\ln|g - g_c| + 1)/2\pi.$$

Since all models with $\gamma \neq 0$ belong to the same universality class, they all present the same singular behavior [Sachdev, 2001]. This is contrasted with the case of XX model, which belongs to a different universality class.

As the fermionic operators are related to spin operators by the Jordan-Wigner transform, the fermion counting distribution is, up to a constant, equivalent to the counting distribution of the spins in z-direction in the transverse XY-model in eq. (2.11).

5.1.2 Detection of Quantum Many-Body Phenomena

We are mainly interested in the quantum phase transition as well as the formation of pairs.

In Fig. 5.1, both effects are illustrated for exemplary system parameters: In Fig. 5.1 a), we plot the counting probability distribution for the Ising model $\gamma = 1$ at zero temperature with no transverse field $g = 0$ and perfect detection efficiency. We consider a system with zero excitations and $N = 1000$ sites. The probability distribution is centered around a mean value $\bar{m} = 500 = N/2$ particles and its standard deviation $\sigma = 50$ such that $\sigma^2 = N/4$. For perfect detection efficiency, the pairing that is present in the system hamiltonian eq. (5.1) only allows for the detection of pairs of particles and thus leads to a zero probability of finding an odd number of particles. In this section, we discuss the detection of fermionic pairs for detectors with efficiency $\kappa < 1$.

In Fig. 5.1 b, we plot the mean $\bar{m}$ and variance σ^2 of the counting distribution as a function of the transverse field g. The mean number of particles increases with increasing transverse field g. The variance is constant with g up to the critical point, when it decreases with increasing g. The phase transition at $g = 1$ is clearly visible both in the mean and in the variance. We study the behavior of the counting distribution for different values of the anisotropy parameter γ.

In Sect. 5.1.3, we consider the counting statistics when the particles are counting particles with spatial resolution.

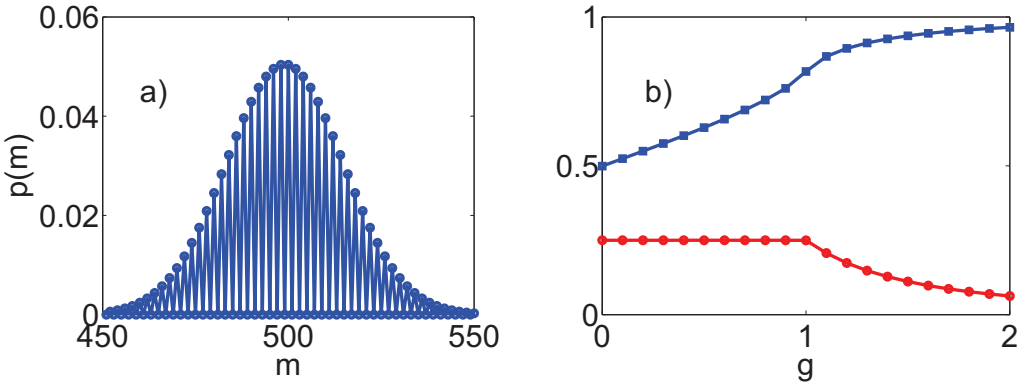

Figure 5.1: a) Counting probability distribution $p(m)$ of finding m particles as a function of m for the fermionic system eq. (5.1) with $\gamma = \kappa$=1, $g = 0$ and $N = 1000$. At $T = 0$ and unit efficiency, the fermion pairing is reflected in the counting distribution, as the probability of finding odd numbers of particles is zero. b) Mean $\bar{m}/N$ (blue squares) and variance σ^2/N (red circles) of the counting distribution as a function of the transverse field g. At $T = 0$, the quantum phase transition at $g = 1$ is clearly visible in the mean and variance.

Detection of Pairs

Let us consider the detection of fermion pairs. Fig. 5.1 a depicts the counting distribution for the detection with unit detection efficiency. In this ideal case, the counting distribution is exactly zero for odd numbers of particles. The pair formation is thus reflected in the counting distribution. However, in real experimental systems, the detection efficiency is typically limited. In Fig. 5.2, we show the counting distribution for a detection efficiency at 99.9%. We observe that the distributions oscillate between higher probabilities for even, and lower probabilities for odd number of counts. This behavior is very strongly affected by κ, since at finite efficiency, one may easily miss single atoms from the Cooper pairs, and obtain odd counts. Similarly, the even-odd asymmetry is strongly affected by the finite size effects - for a given value of $\kappa < 1$ it is visible only for N small enough. For the parameters shown in Fig 5.2, the splitting between the counting probabilities of even and odd counts is observed for a system of $N = 1000$ particles, whereas for $N = 5000$ it is no longer visible. Similar behavior has also been observed in [Cherng and Demler, 2007]. Note that the effect is determined by the counting process, and is not inherent to the system. In Chapter 5.2, we

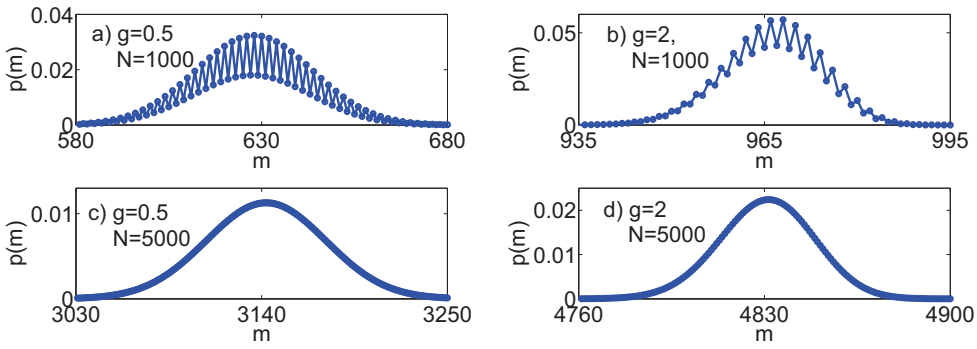

Figure 5.2: Finite size effects for the even versus odd splitting for $\kappa = 0.999$ in the Ising model $\gamma = 1$ at $T = 0$. For N=1000 (a) and (b) the probability distribution splits up, whereas for N=5000 (c) and (d), there is virtually no splitting.

consider the effect of temperature on the fermion pairs and show that the pairs are broken as temperature increases.

Detection of the Quantum Phase Transition

In Fig. 5.1 b, we showed that the phase transition is clearly visible in the mean and variance of the counting distribution for unit detection efficiency. In Fig. 5.3, we plot the mean and variance of the counting distribution as the efficiency decreases. We show that the curves smooth out as the detector efficiency decreases. However, the signatures of the singularities are clearly visible even for low detection efficiencies.

In Fig. 5.4 a-c, we plot the mean and variance for different values of γ. For finite values of γ, the variance shows a jump in the first derivative, while the first derivative of the mean tends to infinity at g_c. This behavior is seen more clearly in the derivatives of $\overline{m}$ and σ^2 (see Fig. 5.4 d-f). As $\gamma \to 0$, the variance tends to zero as the particle number is conserved in the symmetric XX model. The mean has a diverging derivative for $g < g_c$, and is constant for $g > g_c$.

Let us note that in all considered cases so far, the variance $\sigma^2 < \overline{m}$, i.e. all distributions are sub-Poissonian. It is interesting to note that going from the anti-ferromagnetic to the ferromagnetic case, we do observe a transition from sub-Poissonian behavior at small g, to super-Poissonian for large g. This is true

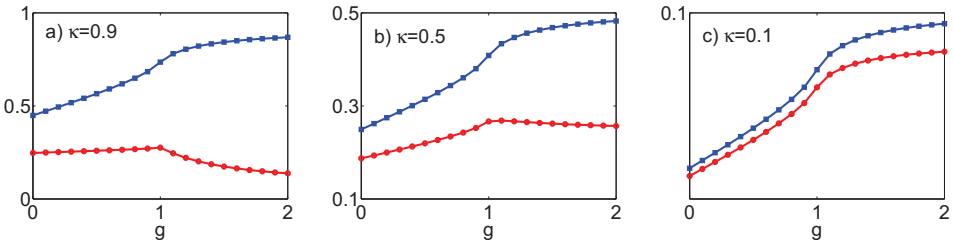

Figure 5.3: As the detection efficiency decreases, the kink in the mean and variance at the quantum phase transition becomes less pronounced. We plot the mean $\overline{m}/N$ (blue squares) and variance σ^2/N (red circles) of the fermion counting distribution at $T = 0$ as a function of g for $\gamma = 1$ (Ising model), and the indicated values of the detection efficiency κ. Even for low detection efficiencies, the phase transition is visible in the mean and variance.

because the variance remains equal to the anti-ferromagnetic case, whereas the mean is replaced by $\overline{m}/N \to (1/2 - \overline{m}/N)$.

5.1.3 Counting Spatial Fourier Components of the Fermion Density

Finally, let us point out that the methods proposed in [Eckert et al., 2008] allow for measurements of various kinds of Fourier components of the total spin. For the spatially resolved QNDPS, $\mathcal{I} = \kappa \sum_{j=0}^{N-1} \sigma_j^\dagger \sigma_j \cos^2(\mathbf{k}_L \mathbf{r}_j)$, where $\mathbf{k}_L$ is the wave vector of the standing wave used for detection, and $\mathbf{r}_j$ is the position of the j-th site. In terms of particle counting, these methods allow, for instance, the counting of particles in every second, every third site, etc. Our theory is easily generalized to such situations.

When we counting every second fermion, we express $b_{2j}^\dagger b_{2j} = c_{2j}^\dagger c_{2j}$ in terms of the quasiparticles d. A calculation analogue to the one in Sec. 5.1 leads to the generating function

$$\mathcal{Q}(\lambda) = \prod_{k=1}^{N/4} \left(1 - 2\lambda\kappa v_k^2 + \lambda^2 \kappa^2 v_k^2\right), \tag{5.15}$$

which is of the same form as eq. (5.4), with the product restricted to $N/4$ terms. We then easily derive analogous recurrences as in the cases considered so far. Fig.

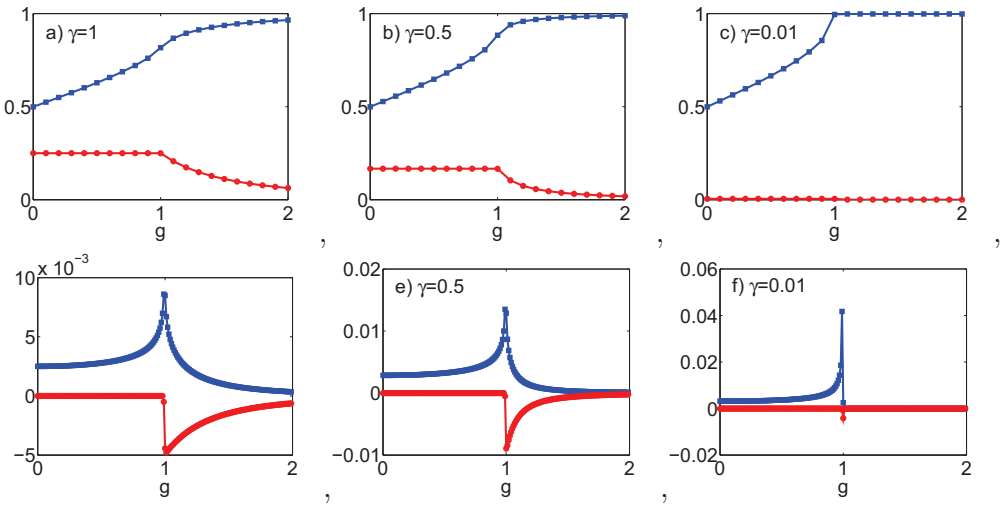

Figure 5.4: The behavior of the mean and variance depends on the anisotropy parameter γ. In graphs a)-c) we plot the mean $\overline{m}/N$ (blue squares) and variance σ^2/N (red circles) of the fermion counting distribution at $T = 0$ as a function of g for $\kappa = 1$, and the indicated values of the anisotropy parameter γ. The effect is more clearly seen from the derivatives of the mean (blue squares) and variance (red circles), plotted in the graphs d)-f).

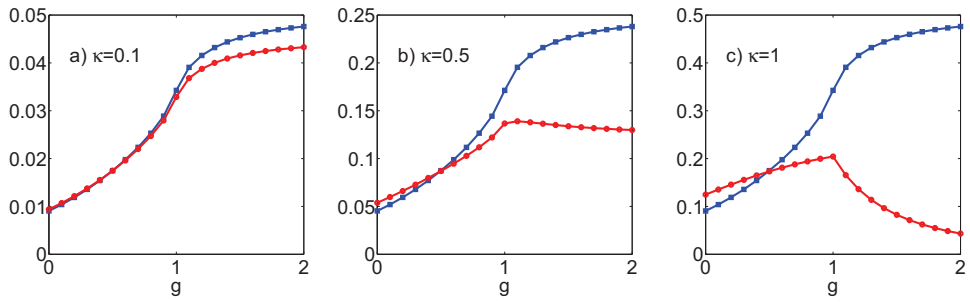

Figure 5.5: Particle counting allows for the detection with spatial resolution. We plot the mean $\overline{m}/N$ (blue squares) and variance σ^2/N (red circles) of the fermion counting distribution, where every second site is counted, as a function of g for $\gamma = 1$ (Ising model) and $T = 0$. The detection efficiencies are given by a) $\kappa = 0.1$, b) $\kappa = 0.5$ and c) $\kappa = 1$. For high detection efficiencies, a crossover from sub- to super-Poissonian behavior at $g = 0.5$ is clearly visible.

5.5 shows the behavior of the mean and the variance, when counting every second spin, in the transverse Ising model. Note that the traces of singular behavior at $g = g_c$ persist. Interestingly, there is a crossing from sub- to super-Poissonian behavior at $g = 0.5$. For $\gamma \to 0$ the point of crossing moves to zero as the variance approaches zero.

5.2 Finite Temperature Effects

Let us now study the properties of the system at finite temperatures at thermal equilibrium. The effect of thermal fluctuations is two-folded. On the one hand, thermal fluctuations induce the breaking of fermionic pairs. On the other hand, the quantum phase transition reduces to a crossover between different regions of the phase diagram. We will show that both effects are visible in the counting distribution functions.

5.2.1 Counting Statistics

In this section, we derive the counting distribution for a system at finite temperature T using the canonical ensemble, $\rho = \frac{1}{Z} e^{-\beta \hat{H}}$, where $\beta = \frac{1}{k_B T}$. The partition

function is given by $Z = \mathrm{Tr}\left(e^{-\beta\sum_k \hat{H}_k}\right)$. The finite temperature T determines the average number of quasiparticle excitations $\hat{d}_k$. In order to calculate the terms A_k and B_k defined in eq. (5.8), we write $\rho_k = \frac{1}{Z_k} e^{-\beta\hat{H}_k}$ where $Z_k = \mathrm{Tr}\left(e^{-\beta\hat{H}_k}\right)$ and we take the trace in the basis $\{|00\rangle|01\rangle|10\rangle|11\rangle\}$. We obtain

$$A_k = \frac{2\kappa}{Z_k}(v_k^2 + e^{-\beta E_k} + e^{-2\beta E_k} u_k^2)$$

$$B_k = \frac{\kappa^2}{Z_k}(v_k^2 + e^{-2\beta E_k} u_k^2) \tag{5.16}$$

$$Z_k = 1 + 2e^{-\beta E_k} + e^{-2\beta E_k} \tag{5.17}$$

For a given value of the transverse field g, we fix the temperature and obtain the number $N_d = \sum_{k=1}^{N/2} N_k^d$ of fermionic excitations

$$N_k^d = \mathrm{Tr}\left(\rho_k \hat{n}_k^d\right). \tag{5.18}$$

As explained above, we use A_k and B_k to obtain the recursive formula for the counting distribution.

5.2.2 Pair Breaking

Thermal fluctuations induce the breaking of pairs. For increasing temperature, the pairing of fermions, whose binding energy is proportional to γ in eq. (5.1), is suppressed. In Sect. 5.1.2, we discussed the splitting of the counting distribution between values with even and odd particle numbers. For perfect detection efficiency, the probability of finding an odd number of particles was shown to be zero at $T = 0$. The pair breaking due to temperature effects is reflected in the counting distribution, where the counting probability for odd numbers of particles becomes non-zero. In Fig. 5.6, we illustrate the effect of thermal fluctuations on the fermion pairing. We plot the probability of counting the exemplary odd value of $m = 499$ particles as a function of temperature. As temperature increases, the pairs are destroyed and we observe a transition from zero probability to a finite value. We compare a system with small interaction strength $\gamma = 0.01$ (Fig. 5.6 a) to the case of $\gamma = 1$ (Fig. 5.6 b). In the insets, we compare the counting distribution for each system at zero temperature and at higher temperatures. We observe that the splitting between even and odd particle numbers disappears as the temperature increases. Note that here we consider a perfect detection

process. For lower detection efficiency, the splitting is not visible, as was shown in Sect. 5.1.2. For small interaction strength γ, the counting distribution is narrower, while higher binding energies γ imply broader atom number distribution functions.

5.2.3 Criticality of the System

Let us now turn our discussion to the influence of temperature on the criticality of the system. As was seen above for the case of zero temperature, the phase transition is visible in the mean and variance of the distribution. This behavior is even more evident in the derivatives of the mean and variance. In Fig. 5.7, we plot the derivative of the means and variances with respect to g at different temperatures T. The criticality is no longer visible when the temperature is of the order of the energies of the system $k_B T \sim E_k$. At high temperature, the mean and variance become independent of the transverse field value g and take a constant value of $0.5N$ and $0.25N$, respectively.

5.3 Counting Statistics during Thermalization

The long decoherence times of experiments with ultracold atoms allow to study the real time quantum dynamics of the system. The dynamics of an open system coupled to a heat bath have recently aroused much interest [Diehl et al., 2008, Kraus et al., 2008, Verstraete et al., 2009] as one can use dissipation for quantum state engineering. By tuning the properties of the reservoir, thermalization can drive the system to a steady state which has the desired properties and can e.g. be used to encode quantum information. Here, we consider the thermalization of the system hamiltonian eq. (5.1), when it is coupled to a heat bath. We start from the ground state at $T = 0$ and let the system evolve to the thermal Boltzmann-Gibbs equilibrium state. In this sense, we analyze the counting statistics in a temperature quench. The coupling to the heat bath is described the quantum

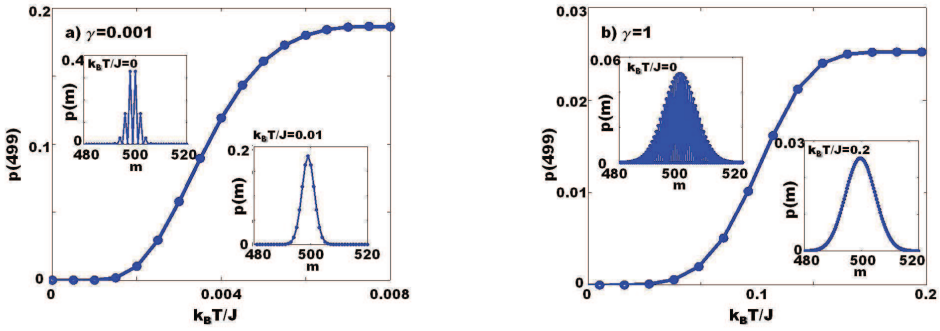

Figure 5.6: The formation of fermionic pairs is reflected in the counting distribution, as the probability of counting odd numbers of particles is zero for unit detection efficiency. We plot the exemplary value of m=499 of counting an odd number of particles as a function of the temperature T. As T increases, the pairs are broken, such that the probability of detecting odd particle numbers is no longer zero. The interaction strength γ determines the temperature at which the pairs are broken. For $\gamma = 0.001$ (Fig. a), the pairs are broken at temperatures around $0.002 k_B T/J$, at $\gamma = 1$ (Fig. b), the pairs are broken at around $0.05 k_B T/J$. The insets show the counting distribution for T=0 and T=0.01 in Fig. a) and for T=0 and T=0.2 in Fig. b).

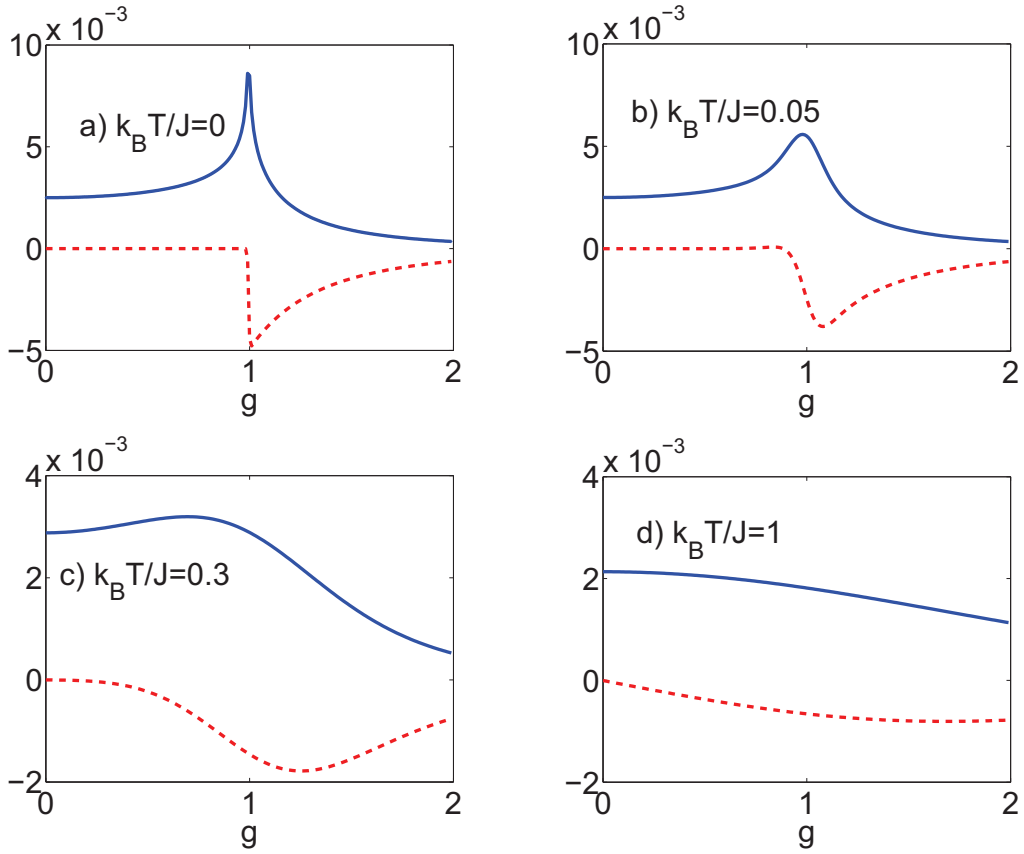

Figure 5.7: The signature of the quantum phase transition is reflected in the mean and variance of the counting distribution even at finite temperatures. We plot the derivatives of the mean $\bar{m}/N$ (blue squares) and the variance σ^2/N (red circles) of the counting distribution of the fermionic system eq.(5.1) with $\gamma = 1$ as a function of the transverse field g. When the temperature is comparable to the energies of the system (Fig. d), the quantum phase transition at $g = 1$ is no longer visible.

master equation [Breuer and Petruccione, 2002]

$$\begin{aligned}&\frac{d}{dt}\rho(t) = \\ &\gamma_0 \sum_k (\frac{N_k^d}{2} + 1)\left[\hat{d}_k \rho(t) \hat{d}_k^\dagger - \frac{1}{2}\hat{d}_k^\dagger \hat{d}_k \rho(t) - \frac{1}{2}\rho(t)\hat{d}_k^\dagger \hat{d}_k\right] \\ &+\gamma_0 \sum_k \frac{N_k^d}{2}\left[\hat{d}_k^\dagger \rho(t) \hat{d}_k - \frac{1}{2}\hat{d}_k \hat{d}_k^\dagger \rho(t) - \frac{1}{2}\rho(t)\hat{d}_k \hat{d}_k^\dagger\right], \end{aligned} \tag{5.19}$$

where γ_0 is the coupling strength and N_k^d in eq. (5.18) accounts for the mean number of fermions in the kth mode at a certain temperature T. This open system dynamics assures that the system approaches thermal equilibrium towards the Boltzmann-Gibbs state.

At this point, we would like to clarify an important point in relation to particle counting of a dynamical system. The system is governed by two different dynamic processes, one is the coupling to the heat bath described by eq. (5.19), the other one is the detection by particle counting described by eq. (4.7). We assume that the coupling of the system to the heat bath occurs on a time scale much slower than the counting process. The counting is thus performed in a time interval in which the coupling to the bath does not affect the system, so that it can be considered time independent. Below we show how the counting statistics change during thermalization of the system with the heat bath. However, each of the distributions is registered at the detector in a time interval in which no change occurs.

5.3.1 Coupling to the Excitations

In order to calculate the counting statistics of the system coupled to a heat bath, we calculate the terms A_k and B_k as given in eq. (5.8), which now depend on time. From the master equation (5.19), the time dependent mean excitation number is obtained as

$$\langle \hat{n}_k^d(t)\rangle = \mathrm{e}^{-\gamma_0 t}\langle \hat{n}_k^d(0)\rangle + N_k^d(1 - \mathrm{e}^{-\gamma_0 t}). \tag{5.20}$$

We start with the system initially in the vacuum state and use

$$\langle \hat{d}_k^\dagger \hat{d}_k \hat{d}_{-k}^\dagger \hat{d}_{-k}(t)\rangle = \langle \hat{d}_k^\dagger \hat{d}_k\rangle_t \langle \hat{d}_{-k}^\dagger \hat{d}_{-k}\rangle_t$$

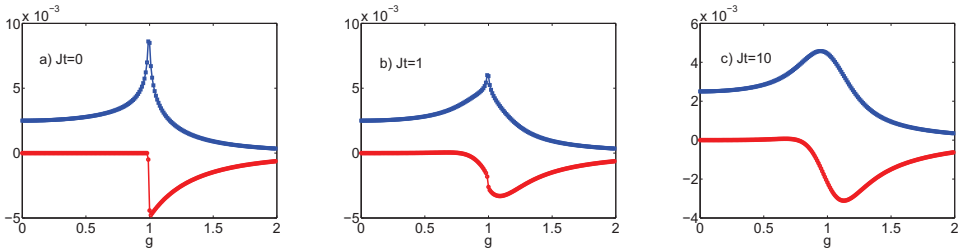

Figure 5.8: When the system is coupled to a heat bath, the criticality at $g = 1$ gets washed out in the counting distribution as the coupling time increases. We plot the derivatives with respect to g of the mean (blue squares) and variance (red circles) for $\gamma = 1$ for increasing coupling time with γ_0=1 and $k_BT = 0.1$. a) Initial time when the system is not coupled to the bath. b) $t/J = 1$ and c) $t/J = 10$.

to calculate the time dependent terms $A_k(t)$ and $B_k(t)$ for a system in a heat bath

$$\frac{A_k(t)}{\kappa} = u_k^2 N_k^d(1 - e^{-\gamma_0 t}) + v_k^2(2 - N_k^d(1 - e^{-\gamma_0 t}))$$

$$\frac{B_k(t)}{\kappa^2} = u_k^2 \frac{(N_k^d(1 - e^{-\gamma_0 t}))^2}{4}$$
$$+v_k^2(1 - N_k^d(1 - e^{-\gamma_0 t}) + \frac{(N_k^d(1 - e^{-\gamma_0 t}))^2}{4}).$$

In Fig. 5.8, we plot the derivatives of the mean and variance with respect to the transverse field g at different times t at a fixed coupling rate $\gamma_0 = 1$ and at fixed temperature of the bath $k_BT = 0.1$. At the initial time $t = 0$, the mean and variance correspond to those of the zero excitation state, ground state at zero temperature (Fig. 5.8 a). The phase transition is clearly visible in the derivative both of the mean and the variance. Due to the coupling of the system and the bath, already for intermediate times (see Fig. 5.8 b), the characteristic behavior of the mean and variance in the critical region washes out. For long coupling time, as shown in Fig. 5.8 c), the behavior is completely determined by the bath.

In Fig. 5.9, we plot the mean and variance as a function of time t for a system coupled to a heat bath at very high temperature $k_BT = 100$. Here, the transverse field g is fixed. For no transverse field $g = 0$ (Fig. 5.9 a), both the mean and the variance are constant as the coupling increases. At the critical point $g = 1$ (Fig. 5.9 b), the variance is constant and the mean decreases as the coupling time

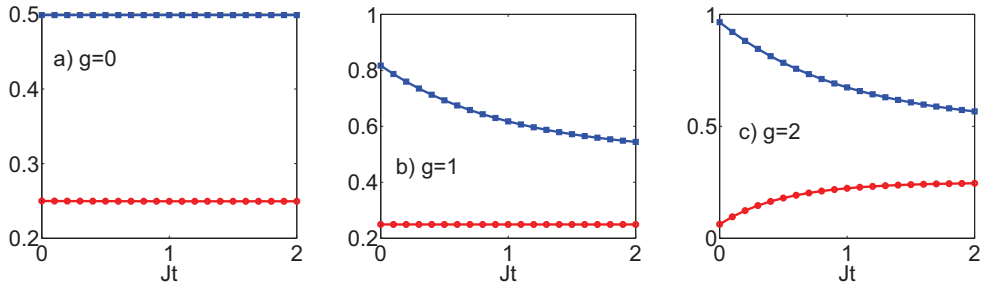

Figure 5.9: Mean (blue squares) $\bar{m}/N$ and variance σ^2/N (red circles) of the counting distribution as a function of the coupling time t/J ($\gamma = \gamma_0 = 1$). In Fig. a), $g = 0$. In Fig. b), $g = 1$ and in Fig. c), $g = 2$.

increases. For high transverse field $g = 2$ (Fig. 5.9 c), the mean decreases until reaching the value of $0.5N$ and the variance increases up to the value $0.25N$.

5.3.2 Local Representation of the Coupling

The master equation eq. (5.19) that we use to describe thermalization shows two aspects. On the one hand, it is physically meaningful to describe the coupling to the bath in terms of an exchange of quasiparticles $\hat{d}_k$, because the Hamiltonian eq.(5.1) conserves the number of quasiparticle excitations. On the other hand, it may look non-physical because the exchange between the system and the bath is non-local. The aim of this section is to show that the master equation can be rewritten in terms of local fermions $\hat{c}_l$ and in principle it could be realized using reservoir designs [Diehl et al., 2008, Kraus et al., 2008, Verstraete et al., 2009].

At high temperatures and in the absence of a transverse field ($g = 0$) at any temperature, the number of excitations N_k^d in the bath is constant with k. In

this case, the master equation (5.19) in terms of the local operators $\hat{c}_l$ reads

$$\begin{aligned}
&\frac{d}{dt}\rho(t) = \\
&\gamma_0(\frac{N_d}{N}+1)\sum_{l,m}[F_u(l-m)\hat{c}_l\rho\hat{c}_m^\dagger + F_v(l-m)\hat{c}_l^\dagger\rho\hat{c}_m - F_{uv}(l-m)(\hat{c}_l^\dagger\rho\hat{c}_m^\dagger - \hat{c}_l\rho\hat{c}_m) \\
&\quad -\frac{1}{2}(F_u(l-m)\hat{c}_l^\dagger\hat{c}_m\rho + F_v(l-m)\hat{c}_l\hat{c}_m^\dagger\rho - F_{uv}(l-m)(\hat{c}_l^\dagger\hat{c}_m^\dagger\rho - \hat{c}_l\hat{c}_m\rho)) \\
&\quad -\frac{1}{2}(F_u(l-m)\rho\hat{c}_l^\dagger\hat{c}_m + F_v(l-m)\rho\hat{c}_l\hat{c}_m^\dagger - F_{uv}(l-m)(\rho\hat{c}_l^\dagger\hat{c}_m^\dagger - \rho\hat{c}_l\hat{c}_m))] \\
&+\gamma_0\sum_k\frac{N_d}{N}\sum_{l,m}[F_u(l-m)\hat{c}_l^\dagger\rho\hat{c}_m + F_v(l-m)\hat{c}_l\rho\hat{c}_m^\dagger - F_{uv}(l-m)(\hat{c}_l^\dagger\rho\hat{c}_m^\dagger - \hat{c}_l\rho\hat{c}_m) \\
&\quad -\frac{1}{2}(F_u(l-m)\hat{c}_l\hat{c}_m^\dagger\rho + F_v(l-m)\hat{c}_l^\dagger\hat{c}_m\rho - F_{uv}(l-m)(\hat{c}_l^\dagger\hat{c}_m^\dagger\rho - \hat{c}_l\hat{c}_m\rho)) \\
&\quad -\frac{1}{2}(F_u(l-m)\rho\hat{c}_l\hat{c}_m^\dagger + F_v(l-m)\rho\hat{c}_l^\dagger\hat{c}_m - F_{uv}(l-m)(\rho\hat{c}_l^\dagger\hat{c}_m^\dagger - \rho\hat{c}_l\hat{c}_m))]
\end{aligned} \tag{5.21}$$

where we define the functions

$$\begin{aligned}
F_u(l-m) &= \frac{1}{N}\sum_k u_k^2 e^{i\Phi_k(l-m)} \\
F_v(l-m) &= \frac{1}{N}\sum_k v_k^2 e^{i\Phi_k(l-m)} \\
F_{uv}(l-m) &= \frac{i}{N}\sum_k u_k v_k e^{i\Phi_k(l-m)},
\end{aligned}$$

which depend on the distance $l-m$ between two sites l and m and are related to the correlation length of the quasiparticles and the pairs. In Fig. 5.10, we plot the behavior of the functions F_u, F_v and F_{uv} as the distance between the sites increases. We plot F_u, F_v and $\frac{1}{i}F_{uv}$ for different values of g and γ/J and show that the functions F_u, F_v have their maximum at zero distance and decay rapidly as the distance increases. The function F_{uv}, which corresponds to the pair correlations, has its maximum at the nearest neighbor term $l-m=1$. We observe that for large transverse field $g \gg 1$, and $\gamma/J \to 0$, the only non-zero term corresponds to $F_v(0)=1$. In this case, the XY model behaves like a free

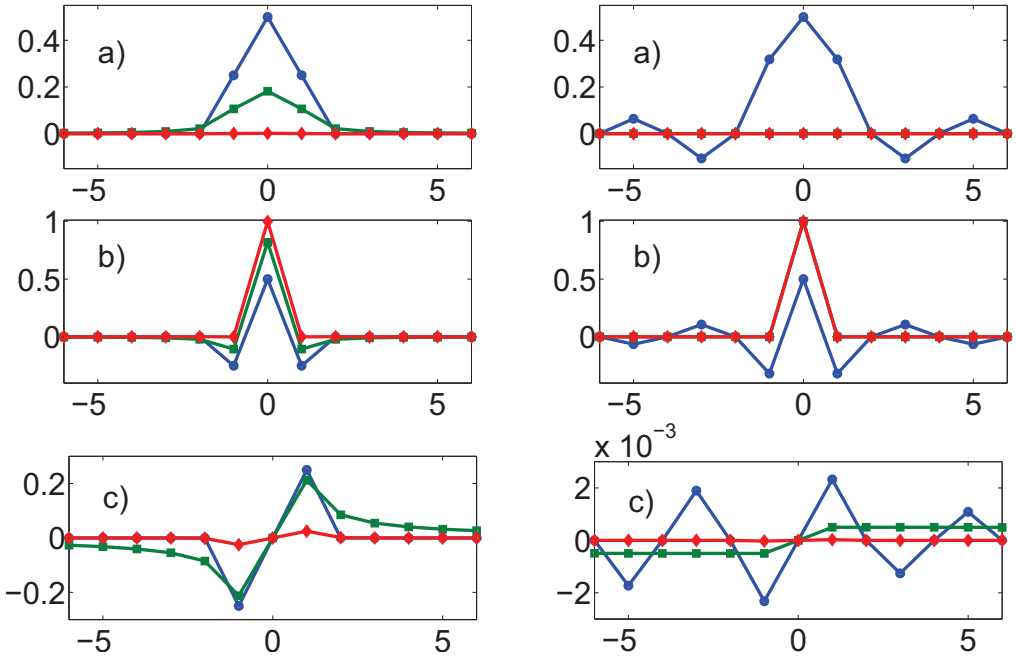

Figure 5.10: Locality of the coupling: F_u (a), F_v (b) and F_{uv} (c) as a function of distance between sites $(l-m)$ for $\gamma = 1$ and $g = 0$ (blue line/circles), $g = 1$ (green line/squares) and $g = 10$ (red line/diamands). The functions F_u, F_v and F_{uv} decay rapidly as the distance between the sites increases. From Eq. (5.21) it is clear that the coupling to the particles is practically local.

fermi gas and the master equation (5.19) reduces to

$$\frac{d}{dt}\rho(t) = \gamma_0(N_d/N+1)\sum_l [\hat{c}_l^\dagger \rho \hat{c}_l - \frac{1}{2}\hat{c}_l\hat{c}_l^\dagger\rho - \frac{1}{2}\rho\hat{c}_l\hat{c}_l^\dagger] + \gamma_0 N_d/N \sum_l [\hat{c}_l \rho \hat{c}_l^\dagger - \frac{1}{2}\hat{c}_l^\dagger\hat{c}_l\rho - \frac{1}{2}\rho\hat{c}_l^\dagger\hat{c}_l].$$

Note that for these parameters, the quasiparticles $\hat{d}_k \to \hat{c}_k^\dagger$. Thus at high T and high transverse field g the bath and the system exchange fermionic particles.

Another interesting limit occurs at any T when $g \to 0$ and $\gamma/J = 1$. We see in figure 5.10, that in this case, the functions F_u, F_v are of order 0.5 for the same site and F_u, F_v and F_{uv} are of the order of ± 0.25 for neighboring sites. The master equation eq. (5.21) has contributions from exchange of on-site fermions and an additional term that corresponds to neighboring particles. Also, there is

exchange of not only on-site particles and holes but also fermionic pairs. This is expected as in this regime $g \ll \gamma, J$ the pair creation dominates in Hamiltonian eq. (5.1).

For low temperatures and at $g \neq 0$, the number of quasiparticles N_k^d is not constant with k and the master equation cannot be written in the form eq. (5.21). However, as N_k^d is small for low temperatures, the non-local terms are negligible and the equation as a whole remains local.

5.4 Summary

We have studied a strongly correlated system of fermions in an optical lattice by using particle counting. At zero temperature, the quantum phase transition of the model is clearly visible in the mean and variance of the counting distribution. Furthermore, we have shown that for high detection efficiencies, the formation of fermionic pairs is visible in the counting distribution. For lower efficiencies the effect is obscured.

We have analyzed the effects of temperature on the counting distribution. Thermal fluctuations induce pair breaking in the superfluid fermionic system. We show that this is reflected in the particle number distribution function, which becomes non-zero for odd numbers of particles for a temperature proportional to the pair formation strength. Also, thermal fluctuations reduce the quantum phase transition into a crossover between different regions of the phase diagram. We have found that at low temperatures, the mean and variance of the counting distribution reflect the critical behavior at the crossover between different phases. This effect is obscured with increasing temperature and when the temperature is comparable to the eigenergies of the system, the cumulants of the counting distribution no longer reflect the critical behavior.

Furthermore, we have shown that the number distribution functions can be used to monitor the quantum dynamics of the system. We have studied the thermalization of the system, initially at zero temperature, when it is coupled to a heat bath at finite temperature. This process is analogous to a temperature quench. The temperature determines the number of delocalized excitations in the system at equilibrium. For high temperatures and high transverse fields, the exchange of

excitations between system and bath can be mapped into the exchange of local fermions. For zero transverse field, we have shown that the exchange of local excitations corresponds to the exchange of local particles and nearest neighbor pairs. We have assumed that the counting process occurs at a different time scale, much faster than the exchange of excitations between the system and the bath. We have shown that the mean and variance of the counting distribution can be used to map the thermalization process.

Chapter 6

Instantaneous Detection of Atoms Falling from a Lattice

In this Chapter, we study the particle counting statistics for the detection of a system of bosons after time-of-flight expansion from the lattice. Here, the particles are released from the lattice and fall onto a detector such as a microchannel plate (see Sect. 2.4.4). In such a setup, the geometry of the detector is controlled by post-selecting the desired region of the microchannel plate after the detection process. We are interested in detecting the initial correlations between particles at different sites after the expansion from the lattice. Propagation in the gravitational field mixes the initial modes of the atoms, such that the counting statistics in the lattice, and after propagation are not expected to be the same. We show that the mixing of the initial modes during the expansion becomes evident in the counting distribution when the detector is small compared to the size of the expanded wave function. Interestingly, in this case metastable states with different occupation patterns that appear in systems of dipolar atoms or molecules in optical lattices can be distinguished. We consider initial Mott insulator (MI) and superfluid (SF) states, as well as states with different occupation patterns in the insulating regime and supersolid states with different density distributions. We calculate both the counting probabilities at a single detector and the joint probabilities at two detectors as a function of the horizontal distance between them. We show that a SF and MI state can be readily distinguished from their counting statistics. The detection of the short range correlations appearing in insulating states is more challenging and requires detector sizes of the order of

the correlation length, which is enlarged due to propagation in the gravitational field. We show that a suitable choice of the detector geometry allows for the detection of different occupation patterns in the insulating regime and different supersolid states.

In Sect. 6.1 we review the propagation of the atomic wave functions when the atoms are released from the optical lattice. In Sect. 6.2 we discuss the effect of expansion on the counting distribution and analyze the intensities of particles arriving at the detector. We show that the detection of long-range correlations can be achieved with detectors whose size is of the order of the expanded wave function. In contrast, the detection of different occupation patterns requires small detector sizes. In Sect. 6.3, we show that particle counting with large detectors allows for the detection a SF and MI states. We further show that using appropriately chosen detector geometries, states with different occupation patterns in the insulating regime as well as different supersolid states can be detected.

6.1 Description of the System

We consider neutral bosonic atoms trapped in an optical lattice. The system can be described using the Bose-Hubbard model eq. (2.8), which includes the hopping of the particles between neighbouring sites and the on-site two-body interactions. At zero temperature, the two limiting cases of the phase diagram are the superfluid state, where the hopping term dominates, and the Mott insulator state, where local interactions are dominant. The field operator of the many-body system $\Psi(\mathbf{r}, t)$ can be expanded into the N modes a_i

$$\Psi(\mathbf{r}, t) = \sum_i \phi_i(\mathbf{r}, t) a_i. \tag{6.1}$$

For atoms trapped in an optical lattice, a_i describes the destruction of a particle on site i. The corresponding initial wave functions are Wannier functions which can be approximated by Gaussian functions centered at $\mathbf{r}_i$

$$\phi_i(\mathbf{r}, t = 0) = \frac{1}{(\pi\omega^2)^{3/4}} e^{-(\mathbf{r}-\mathbf{r}_i)^2/2\omega^2}, \tag{6.2}$$

where the width ω is chosen such that the initial wave functions at different sites i do not overlap. Throughout this work, we consider a lattice spacing of $a_0 = 266$

nm.

The atoms are released from the optical lattice and expand in the gravitational field. The expansion is illustrated in Fig. 6.1. At finite t, we can apply the single-particle expansion

$$\phi(\mathbf{r},t) = \int d\mathbf{r}' K(\mathbf{r},\mathbf{r}',t)\phi_i(\mathbf{r}',0) \tag{6.3}$$

where the propagator for the free expansion in the gravitational field reads [Kramer et al., 2002]

$$K(\mathbf{r},\mathbf{r}',t) = \Big(\frac{m}{2\pi i\hbar t}\Big)^{3/2} e^{\frac{im(\mathbf{r}-\mathbf{r}')^2}{2\hbar t} - \frac{imgt(z+z')}{2\hbar} - \frac{im^2g^2t^3}{24m\hbar}}. \tag{6.4}$$

The full propagated wave function is then written as

$$\phi_i(\mathbf{r},t) = \frac{e^{-\frac{im^2g^2t^3}{24m\hbar}}}{\pi^{3/4}(i\omega_t+\omega)^{3/2}} e^{-\frac{(\mathbf{r}-\mathbf{r}_i)^2}{2(\omega_t^2+\omega^2)}} e^{-i\frac{(\mathbf{r}-\mathbf{r}_i)^2\omega_t}{2\omega(\omega_t^2+\omega^2)}}, \tag{6.5}$$

where and $\mathbf{r}_t = \mathbf{r}+\mathbf{z}_t$, with $\mathbf{z}_t = (0,0,gt^2/2)$ and we have used that $|\mathbf{r}_t-\mathbf{r}_i| \gg \omega$. Note that in the limit of $\omega_t >> \omega$, the expanded wave function is, up to a phase factor, a Gaussian function centered around $\mathbf{z}_t$ with a width $\omega_t = \hbar t/(m\omega)$.

6.2 Effect of Expansion on the Counting Distribution

Let us now discuss the counting process for the detection of atoms expanding in the gravitational field. We consider a momentary detection process, such that the dynamics of the measurement are fast in comparison to the dynamics. For simplicity and with no loss of generality, we consider the detection time $t_d = \sqrt{2z_0/g}$ which is the time when the center of the cloud arrives at the detector. For a detector located at a distance z_0 from the lattice, the intensity $\mathcal{I}$ of atoms registered at the detector, eq. (4.35), is determined by the expanded field operator $\Psi(z_0,t_d)$ of the atoms at the time t_d of detection and takes the form

$$\mathcal{I} = \sum_{ij} A_{ij} a_i^\dagger a_j, \tag{6.6}$$

where

$$A_{ij}(z_0,\Omega,\kappa) = \kappa \int_\Omega d\mathbf{r}\phi_i^*(t_d)\phi_j(t_d). \tag{6.7}$$

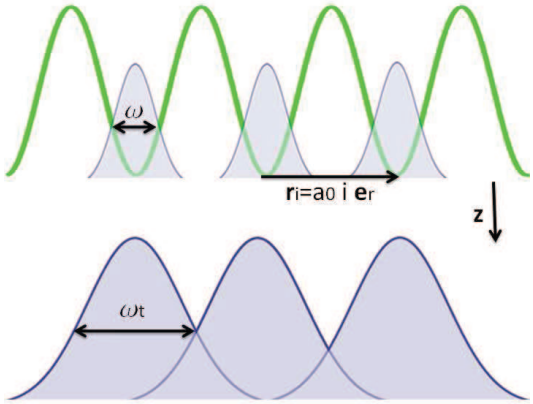

Figure 6.1: The initial Wannier functions of the atoms in the lattice are approximated by Gaussian functions of width ω. Initially, the wave functions do not overlap. During the expansion, the wave functions spread and are described by Gaussian functions of width ω_t that overlap. As this chapter will show, the interference between the initially separated modes plays an important role for the detection of different occupation patterns of atoms in the lattice.

The elements of the correlation matrix A_{ij} defined in eq. (6.7) describe the interference and auto-correlation terms between different modes registered at the detector. The diagonal terms represent the on-site correlations, whereas the off-diagonal terms represent the crossed-correlations between single particle modes initially located at different sites with distance $|i-j|$.

Before studying the full counting distribution, let us consider the correlations given by the matrix elements A_{ij}. Using eq. (6.5) and assuming $\omega_{t_d} \gg \omega$, the auto-correlation elements are given by

$$A_{ii} = \kappa \int_\Omega d\mathbf{r} \frac{1}{\pi^{3/2}\omega_{t_d}^3} e^{-\frac{(\mathbf{r}-\mathbf{r}_i)^2}{\omega_{t_d}^2}} . \tag{6.8}$$

For expanded wave functions at $\mathbf{r} \gg \mathbf{r}_i$, the auto-correlations become all equal and independent of the original lattice site i. The crossed-correlations are given by

$$A_{ij} = \kappa \int_\Omega d\mathbf{r} \frac{1}{\pi^{3/2}\omega_t^3} e^{-\frac{(\mathbf{r}-\mathbf{r}_i)^2}{\omega_t^2}} e^{-i\frac{\mathbf{r}(\mathbf{r}_i-\mathbf{r}_j)}{\omega\omega_t}} \tag{6.9}$$

The ratio between the crossed correlations and the auto-correlations depend crucially on the geometry of the detector.

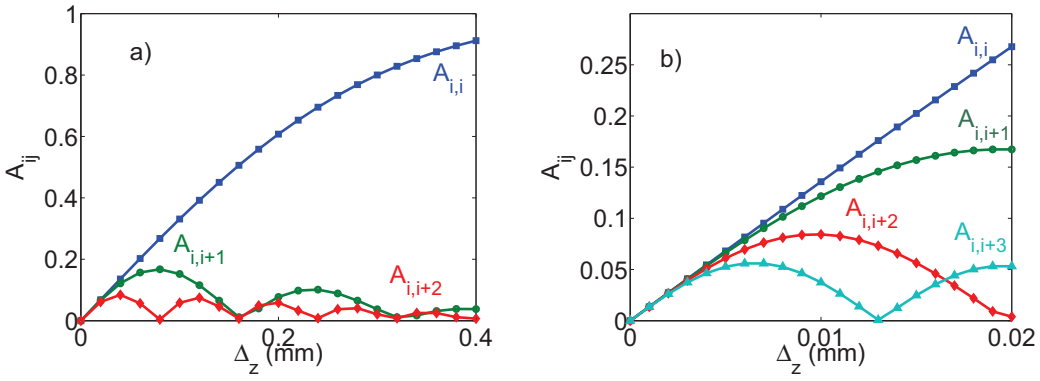

Figure 6.2: The ratio between the on-site-correlations and interference terms depend on the size of the detector. We plot the on-site-correlations (blue squares) and the interference terms with respect to the detector size Δ_z. For detectors of size comparable to the expanded wave function $\Delta_z \simeq \omega_t$ (Fig. a), the on-site correlations are dominant. For $\Delta_z \ll \omega_t$ (Fig. b), the interference terms are of the order of the on-site correlations. The interference terms are plotted as $A_{i,i+1}$ (green circles), $A_{i,i+2}$ (red diamonds), and $A_{i,i+3}$ (light blue triangles). Parameters used: $z_0 = 1$cm, $\Delta_x = \Delta_y = 1$cm and $\kappa = 1$.

In Fig. 6.2, we show the on-site correlations eq. (6.8) and the interference terms eq. (6.9) in function of the size of the detector. We consider a one dimensional array in z-direction and plot the correlations registered by a cubic detector with edges $\Delta_x, \Delta_y, \Delta_z$ located at a distance z_0 from the lattice center. We consider a fixed detector size in the x-y-plane, $\Delta = \Delta_x = \Delta_y$ and vary its width Δ_z in z-direction. Depending on the geometry of the detector, the whole cloud or a fraction of it is registered. For $z_0 = 1$ cm, the size of the expanded single-particle wave function at the detector is $\omega_{t_d} = 0.8$ mm. In Fig. 6.2 a, we show that for detectors of size $\Delta_z > 0.2$ mm, the interference terms are negligible. This is easily understood from eq. (6.8), as the auto-correlations are given by an integral over the detector volume around the center of a Gaussian function. For detectors that are large compared to the size of the cloud, the on-site correlations approach unity. In contrast, the interference terms eq. (6.9) are given by the integral over a Gaussian function multiplied by a highly oscillating phase, such that they approach zero as the size of the detector increases. Therefore, for on-site counting and for detectors which are larger than the size of the cloud, the crossed correlations disappear, $A_{ij} \simeq 0$ for $i \neq j$, while the auto-correlations

approach $A_{ii} \simeq \kappa$.

As we show in the following section, the detection of the auto-correlations between different modes is sufficient to distinguish the long-range correlations in the system. In particular, we show that a MI state can be distinguished from a SF.

On the contrary, as the auto-correlation terms for different sites are equal, distinguishing states with different occupation patterns cannot be achieved in this limit. Fig. 6.2 b shows that for small detector sizes, the interference terms are of the order of the on-site correlations. We will show that in this limit, different occupation patterns are distinguishable from the counting distribution.

6.3 Detection of Initial States by Particle Counting after Expansion

Let us now consider the counting distributions measured at the detector after the expansion for different initial states of the system of atoms in the lattice.

6.3.1 Superfluid state

First, we focus on a SF state, ground state of the Bose-Hubbard model for very shallow lattices. We derive the counting distribution using the Gutzwiller ansatz [Krauth et al., 1992] for the wave function which assumes that it is a product of on-site coherent states. The initial state of the atoms in the lattice with N sites then reads:

$$|\psi\rangle = \prod_{i}^{N} |\alpha_i\rangle_i \,, \tag{6.10}$$

where $|\alpha_i\rangle_i$ is the coherent state on site i,

$$|\alpha_i\rangle_i = e^{-|\alpha_i|^2/2} \sum_{n=0}^{\infty} \frac{\alpha_i^n}{\sqrt{n!}} |n\rangle_i \tag{6.11}$$

and $|n\rangle_i = (a_i)^n |0\rangle$ is a Fock state with n particles. Note that $|\psi\rangle$ is an eigenstate of the annihilation operator $\Psi(\mathbf{r}, t)$ of the expanded atoms,

$$\Psi(\mathbf{r}, t) |\psi\rangle = \sum_i \phi_i(\mathbf{r}, t)\alpha_i |\psi\rangle , \tag{6.12}$$

where ϕ_i is given by eq. (6.2). The state $|\psi\rangle$ is thus an eigenstate of the expanded field operator $\Psi(\mathbf{r}, t)$ and we can write the generating function as $\mathcal{Q}(\lambda) = e^{-\lambda \sum_{ij} \alpha_i^* \alpha_j A_{ij}}$. Using eq. (4.13) the counting distribution $p(m)$ reads

$$p(m) = \frac{\left(\sum_{ij} \alpha_i^* \alpha_j A_{ij}\right)^m}{m!} e^{-\sum_{ij} \alpha_i^* \alpha_j A_{ij}}, \tag{6.13}$$

where A_{ij} is given by eq. (6.7).

For a homogeneous superfluid with equal mean number of particles per sites, $\alpha_i = \alpha$ for all i, and in the limit of large detectors, where the diagonal elements of the matrix A_{ij} are much bigger than the off-diagonal elements, the counting distribution of the SF simplifies to

$$p(m) = \frac{(N|\alpha|^2 A_d)^m}{m!} e^{-N|\alpha|^2 A_d}, \tag{6.14}$$

which corresponds to a Poissonian distribution with mean (and thus also variance) $\bar{m} = \sigma^2(m) = N|\alpha|^2 A_d$.

6.3.2 Mott Insulator state with one particle per site

Let us now consider the Mott insulating regime. We first study a Mott insulator state with one particle per site, $|\psi\rangle = |11..11\rangle$. In this case, the generating function eq. (4.14) reads

$$\begin{aligned} \mathcal{Q}(\lambda) &= \langle 11..11| : e^{-\lambda\kappa \int_\Omega d\mathbf{r} \Psi^\dagger(\mathbf{r},t_d)\Psi(\mathbf{r},t_d)} : |11..11\rangle \\ &= 1 - \lambda \sum_i A_{ii} + \lambda^2 \sum_{i<j} (A_{ii}A_{jj} + |A_{ij}|^2) - .... \end{aligned} \tag{6.15}$$

We can rewrite eq. (6.15) using the minors of the matrix A,

$$\mathcal{Q}(\lambda) = 1 + \sum_{k=1}^{N} (-1)^k \lambda^k \mathrm{M}_+(A, k), \tag{6.16}$$

where $\mathrm{M}_+(A,m)$ denotes the permanent $\mathrm{perm}(A) = \sum_{\sigma\epsilon S_n} \Pi_{i=1}^n A_{i,\sigma(i)}$ of the corner blocks of size m of the matrix A. Note that $\mathrm{M}_+(A,k)$ is closely related to the principal minors of the matrix, which are defined as the determinant of the respective block matrices. The counting distribution $p(m)$ can then be calculated using Eqs. (4.13) and (6.16).

As was outlined above, in typical experimental situations the detector is far away from the lattice and much larger than the cloud, such that the off-diagonal elements of A_{ij} are negligible and the diagonal elements A_{ii} are equal for all i. In this case the generating function $\mathcal{Q}$ for the Mott insulator state with unit filling is given by

$$\mathcal{Q}_{MI}(\lambda) = \sum_{k=0}^{N} \binom{N}{k} (-\lambda A_d)^k = (1 - A_d\lambda)^N, \tag{6.17}$$

where A_d denotes any of the (equal) diagonal elements. The counting distribution $p(m)$ is then given by

$$p(m) = \binom{N}{m} A_d^m (1 - A_d)^{N-m} \tag{6.18}$$

This corresponds to the distribution of a fock state. The mean $\bar{m}$ and variance $\sigma^2(m)$ of the distribution are given by

$$\bar{m} = NA_d \quad \sigma^2(m) = NA_d(1 - A_d) \tag{6.19}$$

6.3.3 Detection of a Mott Insulator and Superfluid State

In Fig. 6.3, we plot the counting distributions for a SF and a MI state at different distances between the detector and the lattice. We show that the two states can be distinguished by observing their counting distributions. With increasing distance from the detector, a smaller fraction of the expanded wave function is registered. The difference between the MI and the SF becomes less visible, and the mean decreases. In Fig. 6.4, we plot the normalized mean and the variance of the counting distributions for the SF and the MI state registered at a detector with fixed size at different distances z_0 from the lattice.

Let us further consider the counting statistics of the MI and SF state using two detectors and study the correlations between the counting events. For the MI state, the joint counting distribution $p_{MI}(m,n)$ of counting m particles at one

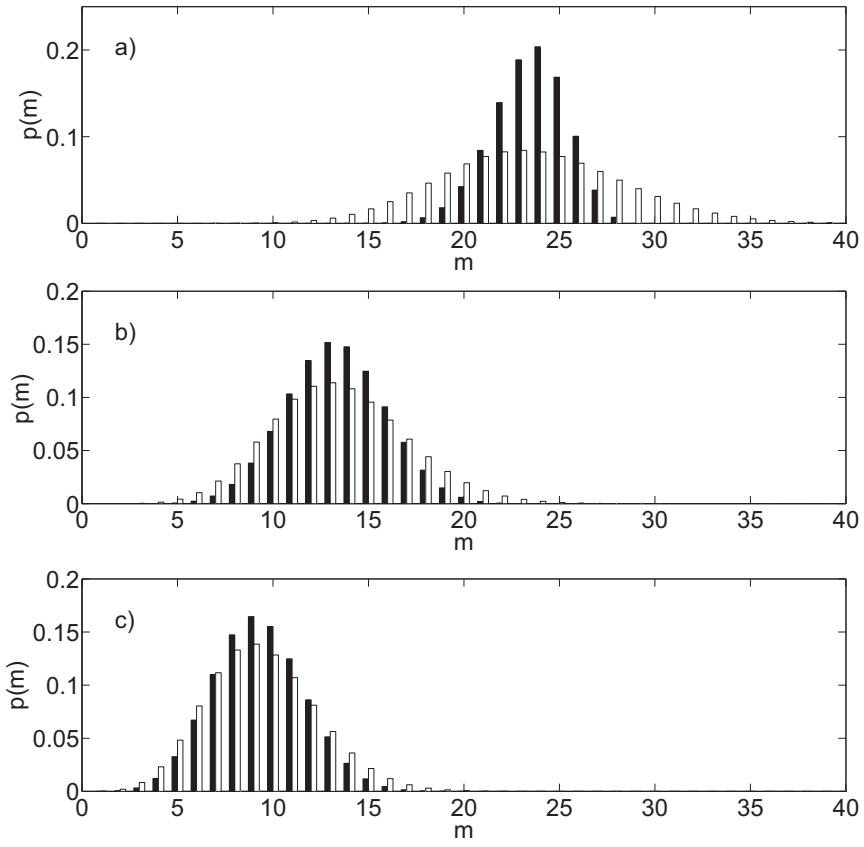

Figure 6.3: The probability distributions for a Mott insulator (black bars) and superfluid (white bars) state released from a 3x3x3 are clearly distinguishable. The particles are registered after expansion at a detector of fixed size at a distance of a) $z_0 = 1cm$, b) $z_0 = 3$ cm, and c) $z_0 = 5$ cm. Parameters used: $\Delta_x = \Delta_y = 2$ mm, $\Delta_z = 2$ cm, $\kappa = 1$.

detector and n particles at the other is given by eq. (4.16), where the generating function for two detectors is given by

$$\mathcal{Q}_2 = \sum_{k=1}^{N} (-1)^k \text{Minors}^*{}_{\pm}(\lambda_1 A^{(1)} + \lambda_2 A^{(2)}, k). \tag{6.20}$$

For detectors that are located symmetrically with respect to the origin in the x-y-plane, in typical experimental situations the off-diagonal elements of A_{ij} are neglected and the diagonal elements A_d are all equal for both detectors, $A_d^{(1)} =$

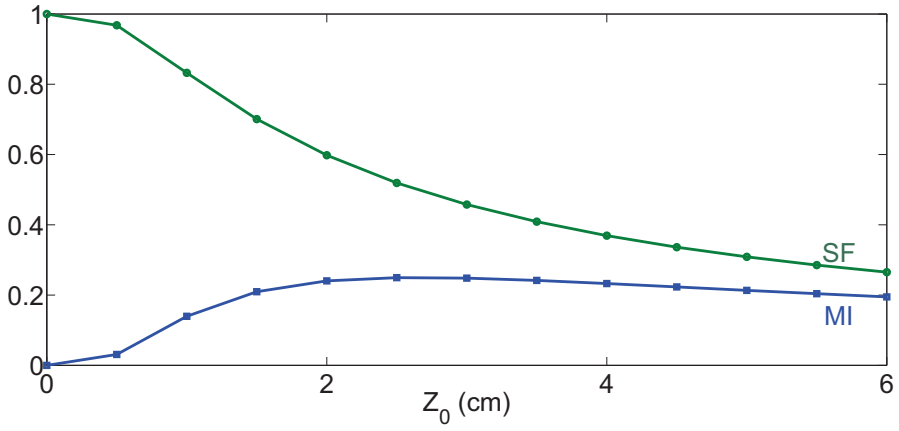

Figure 6.4: Mean $\bar{m}$ and variance $\sigma^2(m)/N$ of the counting distribution for an expanded MI and SF state with respect to the distance from the detector z_0. For the SF state, the mean and variance are equal and are given by the green circles. For the MI state, the mean (green circles) and variance (blue squares) are different. $\Delta_x = \Delta_y = 2$ mm, $\Delta_z = 2$ cm, $\kappa = 1$.

$A_d^{(2)} = A_d$. The generating function thus simplifies to

$$\begin{aligned} \mathcal{Q}_{MI}(\lambda_1, \lambda_2) &= \sum_{k=0}^{N} \binom{N}{k} (-A_d)^k (\lambda_1 + \lambda_2)^k \\ &= (1 - A_d(\lambda_1 + \lambda_2))^N, \end{aligned} \tag{6.21}$$

and the counting distribution is given by

$$\begin{aligned} p_{MI}(m,n) = (-1)^{n+m}(1-2A_d)^{Np-m-n} \times \\ (-A_d)^{m+n} \tfrac{Np!}{m!n!(Np-m-n)!} \end{aligned} \tag{6.22}$$

For the SF state, the joint counting distribution $p_{SF}(m,n)$ is the product of the two single detector distributions $p(m)$ and $p(n)$ given by Eq. (6.13). The counting events are thus not correlated.

We consider two detectors of the same size that are placed symmetrically at a distance $\mathbf{x}_1 = (x_d, 0, z)$ and $\mathbf{x}_2 = (-x_d, 0, z)$ from the lattice center. Fig. 6.5 shows the counting distributions for two overlapping detectors (left column) and for two detectors separated by $2x_d = 1$cm (right column). For the MI state, shown in the upper row in fig. 6.5, we observe a squeezed distribution, indicating the correlations of the atoms counted at the two detectors. Note that the squeezing

is less pronounced when increasing the distance between the detectors. For the SF state, shown in the lower row of fig. 6.5, the joint counting distribution is Gaussian for both cases. This is expected, as the joint counting distribution Eq. (6.13) is a product of the single detector counting distributions.

The correlations in the system can be seen more clearly when looking at the correlation function eq. (4.17). Note that for the superfluid state, there is no difference between the joint counting distribution and the product of the single particle distributions. For the Mott state, we study the correlations for varying distance between the two detectors x_d. In Fig. 6.6, we show how the correlations decrease when increasing the distance between detectors x_d. Note that the distance x_d denotes the distance between the center of the tow detectors. For $x_d = 0$, the detectors fully overlap, and for $x_d > \Delta$ the detectors are completely separated.

6.3.4 Detection of Insulating States with Different Occupation Patterns

Let us now consider the different occupation patterns that arise in the strongly correlated regime. In particular, we focus on such states where at most one particle occupies each site. The generating function is then calculated by eq. (6.16), with a correlation matrix A', composed of the elements of the correlation matrix A in eq. (6.7) multiplied by the occupation numbers n_i and n_j of the involved sites,

$$A' = n_i n_j A_{ij}. \tag{6.23}$$

As discussed above, in order to detect the different patterns, the crossed-correlations have to be of the order of the auto-correlations. This is clear as away from the lattice, all the on-site correlation terms become equal. Let us discuss the example of a checkerboard state, where every second site is occupied, and a state with stripes, where every second line is occupied. For the striped state, the leading crossed-correlation terms eq. (6.9) are the ones that correspond to the nearest neighbors. For the checkerboard state, where neighboring sites are not occupied, the leading terms are the ones that correspond to diagonally adjacent sites. In order to distinguish the different patterns, it is thus essential that these two leading crossed-terms are sufficiently different and at the same time comparable to

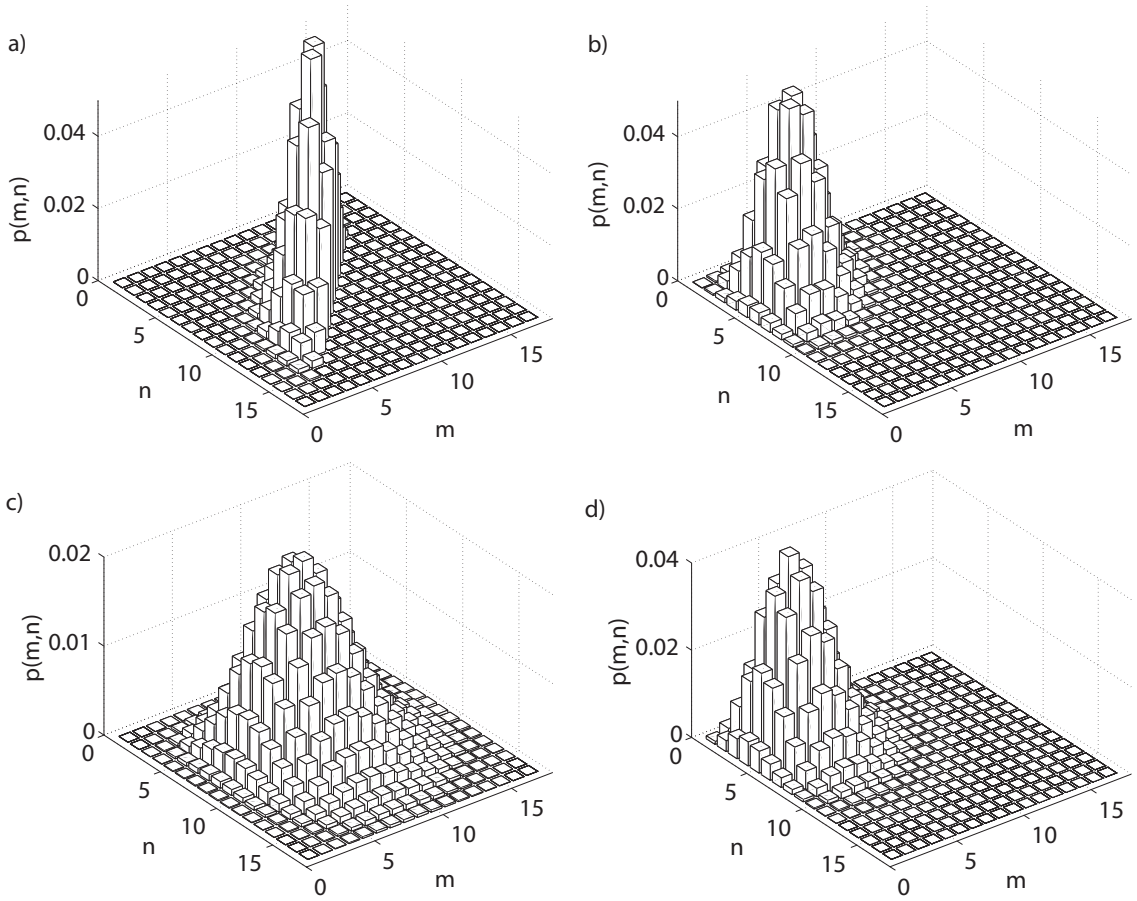

Figure 6.5: Joint probability distribution of an expanded Mott insulator (upper row) and a superfluid state (lower row) in a 4x4 lattice with two symmetrically placed detectors. In fig. a) and c), the two detectors overlap at the center of the lattice in x-y direction. The joint probability distribution for the MI state is squeezed, indicating the correlations the detection events at the two detectors, whereas for the SF states the events are uncorrelated. In fig. b) and d) the detectors are separated by $d = 1$ cm. The squeezing of the distribution for the MI state is less pronounced. Parameters used: $z_0 = 1cm$, $\Delta_z = 2$ mm, $\Delta_x = \Delta_y = 2$ cm, $\kappa = 0.5$.

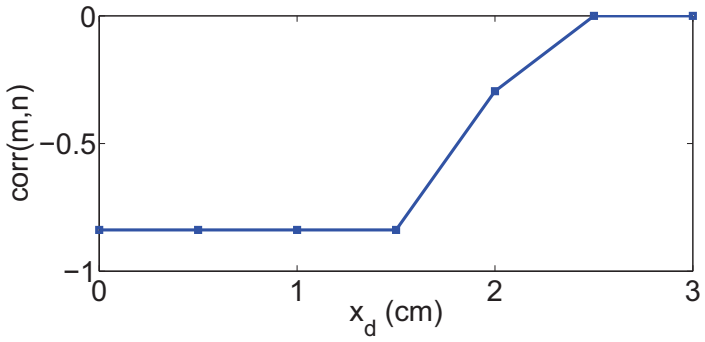

Figure 6.6: Correlations of the joint probability distribution of an expanded MI (upper row) and a SF (lower row) in a 4x4 lattice with two symmetrically placed detectors. The correlations between detection events at the two detectors decrease as the distance between the detectors increases. $z_0 = 1cm$, $\Delta_z = 2$ mm, $\Delta_x = \Delta_y = 2$ cm, $\kappa = 0.5$

the on-site correlations. From Fig. 6.2, we see that this implies that the limit of small detectors has to be considered. However, if the detector is very small, all the terms are equal and the patterns are not distinguishable. One should thus consider an intermediate detector size.

In Fig. 6.7, we illustrate the effect for a 1D system of $N = 12$ particles. We compare the counting distributions of a checkerboard-like state, where every second site is occupied, and a state where a block of six sites is occupied and a block of six sites is empty. In order to distinguish the two states, from Fig. 6.2, we choose a detector size of $\Delta = 0.02$ mm, such that the ratio of the crossed-correlation terms between neighboring sites and the auto-correlations is 0.6. Fig. 6.7 shows that the different occupation patterns are reflected in the counting distribution.

Finally, let us consider a symmetric superposition of all possible states with filling factor N_p/N_s, where N_p is the number of particles, N_s denotes the number of sites and $N_p \leq N_s$, the generating function reads

$$\mathcal{Q} = 1 + \sum_m (-1)^m \lambda^m \mathcal{F}_{MI}(A, m, N_p, N_s), \tag{6.24}$$

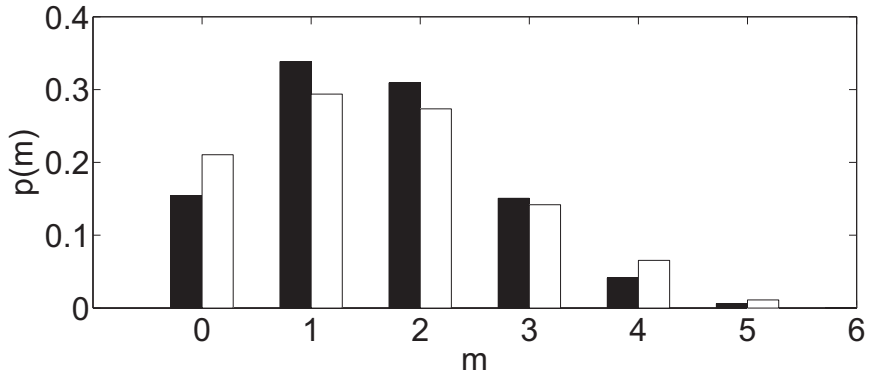

Figure 6.7: The counting distribution of an expanded one dimensional checkerboard (black bars) and striped insulating pattern (white bars) can be clearly distinguished. Parameters used: $z_0 = 1$ cm, $\Delta = 0.1$ cm, $\Delta_z = 0.02$ mm, $\kappa = 1$

where

$$\mathcal{F}_{MI}(A, m, N_p, N_s) = \frac{\binom{N_s-m}{N_p-m}}{\binom{N_s}{N_p}} M^+(A, m) + \frac{\binom{N_s-2m}{N_p-m}}{\binom{N_s}{N_p}} 2^m \mathcal{K}(m), \tag{6.25}$$

where $\mathcal{K}(m)$ is defined as the $m$fold product over the sum with non-repeated indices of the real part of A_{ij}, $\sum_{i<j} \mathrm{Re}(A_{ij})$. For $m = 2$, e.g. $M_+ = \sum_{i<j}(A_{ii}A_{jj} + |A_{ij}|^2)$ and $\mathcal{K}(m) = \mathrm{Re}(A_{ij})\mathrm{Re}(A_{kl})$ with $k, l \neq i, j$.

6.3.5 Detection of a Supersolid state

As for the detection of states with different occupation patterns in the insulating regime, the detection of supersolid states requires the limit where the crossed-correlation terms for neighboring sites are comparable to the auto-correlation terms. We consider a supersolid state with N sites and mean density $\alpha_{2i} = \beta$ and $\alpha_{2i-1} = \gamma$. For the limit where the crossed-correlation terms for neighboring sites are the only non-negligible interference terms, the counting distribution eq. (6.13) is given by a Poissonian distribution with mean

$$\bar{m} = \frac{N}{2} A_d(\beta^2 + \gamma^2) + 2N A_{NN} \beta\gamma, \tag{6.26}$$

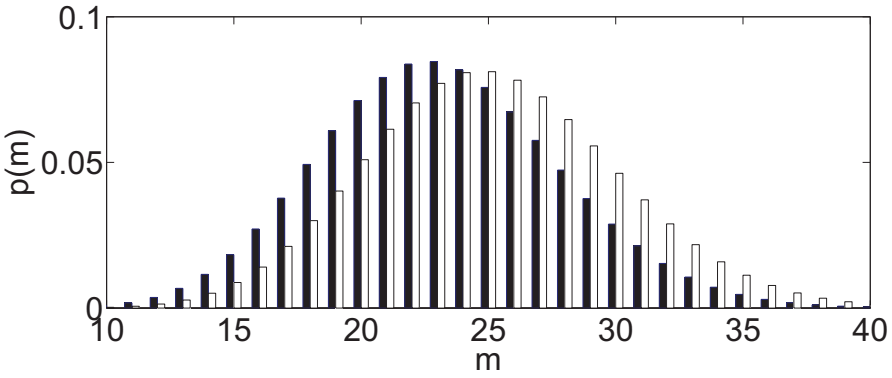

Figure 6.8: The counting distribution of an expanded supersolid state with $|\beta|^2 = 0.5$ and $|\gamma|^2 = 1.5$ (black bars) and an expanded superfluid state $|\alpha|^2 = 1$ (white bars) can be clearly distinguished. Parameters used: $z_0 = 1$ cm, $\Delta = 1$ cm, $\Delta_z = 0.02$ mm, $\kappa = 1$

where A_d denotes the diagonal elements corresponding to the on-site correlations and A_{NN} denotes the nearest neighbor crossed-correlation terms. Let us compare this to a superfluid state with a homogeneous density per site, $|\alpha_i|^2 = \frac{|\beta|^2+|\gamma^2|}{2}$ for all i. The counting distribution eq. (6.13) is thus given by a Poissonian distribution with mean

$$\bar{m} = \frac{N}{2} A_d(\beta^2 + \gamma^2) + N A_{NN}(\beta^2 + \gamma^2). \tag{6.27}$$

From eqs. (6.26) and (6.27) it is clear that a supersolid state can be distinguished from a superfluid state by particle counting. In Fig. 6.8 we illustrate this by comparing a supersolid state with $|\beta|^2 = 0.5$ and $|\gamma|^2 = 1.5$ to a superfluid state with $|\alpha|^2 = 1$.

6.4 Summary

We have studied the counting distributions of atoms falling from an optical lattice and propagating in the gravitational field. The intensity of atoms recorded at a detector located far away from an optical lattice can be decomposed into auto-correlation and crossed-correlations between the expanding modes. The ratio between these terms depends crucially on the geometry of the detector. In the limit when the detector is large compared to the expanded modes, the crossed-correlation terms are negligible and only long-range correlations of different states

can be distinguished. In this limit a SF state has a poissonian number distribution while a MI has subpoissonian number distribution for a detector of finite size located at a distance z_0 from the lattice. Only in the limit of very far detection for a finite sized detector both number distributions become equal. The two states can also be readily distinguished from the joint probability distribution of counting the particles at two detectors. In the SF regime, the joint probability distribution is a product of the two independent number distributions while in the MI regime, the distributions are highly correlated.

When the detector is small compared to the expanded wave function, the crossed-correlation terms for adjacent sites are of the order of the auto-correlations. We have shown that by choosing the size of the detector in an appropriate way, different occupation patterns can be distinguished by particle counting after expansion both in the insulating as well as in the superfluid regime.

Chapter 7

Detection of an Expanding BEC: Effect of Absorption at the Detector

In the preceding chapters, we considered the detection of different strongly-correlated systems by particle counting. We observed that for a wide range of experimental situations, the system dynamics are short compared to the counting process and the counting distribution is obtained from standard methods. In this chapter, we consider the detection of an expanding bose-einstein condensate, where the detector is located on-site or at some distance from the BEC. The atoms are counted while during the expansion of the cloud, such that the dynamics of the system are of the same order as the dynamics of the detection process.

We apply the formalism developed in Chapter 4.3, which gives a time- and space-dependent description of the counting process, taking into account the back-action of the detector on the field. Let us recall that in the Glauber-Mandel formula (4.2), the intensity at the detector is not affected by the absorption of particles at the detector. In this chapter, we illustrate the effect of the absorption by considering the counting distribution for an expanding BEC.

In Sect. 7.1, we describe the system and derive the counting distributions in the time and space dependent formalism. In Sect. 7.2, we discuss an approximate solution using the Born approximation. In Sect. 7.3, we present our results.

7.1 Description of the System

We study the counting statistics of a freely expanding Bose Einstein condensate. For simplicity, we consider a one dimensional system with a point-like detector located at a distance z_0 from the condensate. The detection time is of the order of the system dynamics, such that we calculate the full time- and space dependent generating function given by eq. (4.14), where the intensity is given by eq. (4.28). For a point-like detector modeled by a delta-function $\delta(z - z_0)$, the intensity eq. (4.28) reads

$$\mathcal{I} = \int_0^t dt' \tilde{\Psi}^\dagger(z_0, t')\tilde{\Psi}(z_0, t'), \tag{7.1}$$

where the time evolution of the operators $\tilde{\Psi}(\mathbf{r}, t)$ is described by eq. (4.33). For the detection of a BEC at a point-like detector, the time evolution is given by

$$\tilde{\phi}(z, t) = \int dz' G_S(z, z', t, t_0)\phi(z', t_0), \tag{7.2}$$

where $\tilde{\Psi}(z, t) = N\phi(z, t)a$, N denotes the number of particles and a is the annihilation operator.

$$G_S(z, z', t, t_0) = \langle z| \, e^{-i(t-t_0)(H_0 + i\frac{\epsilon}{2}\delta(z-z_0))} \, |z'\rangle \tag{7.3}$$

The counting distribution is then obtained from eq. (6.13), which for the case of a condensate with N particles is given by

$$p(m) = \frac{\left(N\epsilon \int dt \tilde{\phi}^\dagger(z_0, t)\tilde{\phi}(z_0, t)\right)^m}{m!} e^{-N\epsilon \int dt \tilde{\phi}^\dagger(z_0,t)\tilde{\phi}(z_0,t)}, \tag{7.4}$$

In order to calculate the counting distribution eq. (7.4), we solve eq. (7.2). We approximate the initial wave function $\tilde{\phi}(z, 0)$ by a Lorentzian function,

$$\tilde{\phi}(z, 0) = \sqrt{\Gamma} e^{-\Gamma|z|}, \tag{7.5}$$

In Sect. 7.1.1, we directly solve the time dependent Schrödinger equation to get an analytic solution for the time evolved function $\tilde{\phi}(z, t)$. In Sect. 7.1.2, we solve eq. 4.33 for detectors that are placed at a distance z_0 from the condensate.

7.1.1 On-site Detection of an Expanding BEC

In this section, we calculate the counting distribution $p(m)$ for an expanding BEC, where the detector is located in the center of the cloud at $z_0 = 0$. To this end, we solve the time dependent Schrödinger equation ($\hbar = m = 1$),

$$i\dot{\tilde{\phi}}(z,t) = -\frac{1}{2}\frac{\partial^2}{\partial z^2}\tilde{\phi}(z,t) - i\frac{\epsilon}{2}\delta(z)\tilde{\phi}(z,t) \tag{7.6}$$

with the initial condition given by eq. (7.5).

We write Eq. (7.6) in terms of the fourier transform. From eq. (7.1) is is clear that for a detector placed at $z_0 = 0$, we are only interested in $\tilde{\phi}(0,t) = \frac{1}{2\pi}\int_{-\infty}^{\infty} dk\phi(k,t)$, which we denote by $S(t)$. The fourier transformed equation is a differential equation with variable coefficients and can be integrated by standard methods [Bronstein et al., 2002]. We get

$$S(t) = S_0(t) - \frac{\epsilon}{2}\int_0^t \kappa(t-t')S(t')dt', \tag{7.7}$$

where $S_0(t) = \frac{1}{2\pi}\int dke^{-ik^2t/2}\phi(k,0)$ and $\kappa(t,t') = \frac{1}{2\pi}\int_{-\infty}^{\infty} dke^{-ik^2(t-t')/2} = \frac{(1-i)}{2\sqrt{\pi}\sqrt{t-t'}}$ We take the Laplace transform of eq. (7.7) and use the convolution theorem [Abramowitz and Stegun, 1965, 29.2.8] to obtain

$$S(s) = \frac{S_0(s)}{1 + \frac{\epsilon}{2}\kappa(s)}. \tag{7.8}$$

The term $S_0(s)$ is calculated by using the residue theorem and using the method of partial fractions the expression for $S(s)$ is written in the form $\frac{A}{\sqrt{s}+a_1}$, such that the inverse Laplace transform is given by.

$$S(t) = \tilde{\phi}(0,t) = \frac{\sqrt{\Gamma}(e^{\frac{1}{2}i\Gamma^2 t}\Gamma\mathrm{Erfc}(\frac{1+i}{2}\Gamma\sqrt{t}) + \frac{i}{2}e^{-\frac{1}{8}it\epsilon^2}\epsilon\mathrm{Erfc}(\frac{(1-i)\epsilon}{4}\sqrt{t}))}{(\Gamma + i\frac{\epsilon}{2})} \tag{7.9}$$

The probability distribution $p(m)$ can then be calculated by eq. 7.4.

7.1.2 Detection at a Distance z_0

In this section, we solve eq. (7.2) for a detector placed at a distance z_0 from the condensate. We follow the treatment in [Kleber, 1994] to derive an exact solution for the propagator eq. (7.3) that describes the whole system evolution including

the absorption at the detector. The effective Hamiltonian $H_{eff} = H_0 + H_1$ is composed of two parts: the free particle Hamiltonian H_0 and a part $H_1 = i\frac{\epsilon}{2}\delta(z - z_0)$ corresponding to the detection process, which acts as an imaginary potential. The propagator $G_S(z, z', t)$ can be written in an iterative way using the Lippmann-Schwinger equation, which for a point-like detector $\Omega(z') = \delta(z' - z_0)$ reads

$$G_S(z, z', t) = G_0(z, z', t) - \frac{\epsilon}{2}\int_0^t dt' G_0(z, z_0, t - t')G(z_0, z', t'). \tag{7.10}$$

The propagator $G_0(z, z', t)$ for the free expansion is known to be

$$G_0(z, z', t) = \sqrt{\frac{1}{2\pi i t}}\exp(\frac{i|z - z'|^2}{2t}). \tag{7.11}$$

We perform a Laplace transform of eq. (7.10) and use the convolution theorem to get

$$\tilde{G}(z, z', s) = \tilde{G}_0(z, z', t) - \frac{\epsilon}{2}\tilde{G}_0(z, z_0, s)\tilde{G}(z_0, z', s) \tag{7.12}$$

From eq. 7.1, we observe that we are only interested in the propagator at $z = z_0$, such that

$$\tilde{G}(z_0, z', s) = \frac{\tilde{G}_0(z_0, z', t)}{1 - \frac{\epsilon}{2}\tilde{G}_0(z_0, z_0, s)}. \tag{7.13}$$

The Laplace transform of the free propagator $G(z_0, z', s)$ is given by

$$\tilde{G}(z_0, z', s) = \sqrt{\frac{1}{2is}}\exp(-\sqrt{\frac{2s}{i}}|z_0 - z'|). \tag{7.14}$$

The inverse Laplace transform of $\tilde{G}(z, z', s)$ can be performed by standard methods [Abramowitz and Stegun, 1965], such that the propagator is given by

$$G(z_0, z', t) = G_0(z_0, z't) + \frac{i\epsilon}{4}e^{i(\frac{\epsilon}{2}d + (\frac{\epsilon}{2})^2\frac{t}{2})}\mathrm{erfc}(\sqrt{\frac{1}{2i}}(d/\sqrt{t} - \frac{\epsilon\sqrt{t}}{2})), \tag{7.15}$$

with $d = |z - z_0| + |z_0 - z'|$.

The function $\tilde{\phi}(z_0, t)$ is then calculated by eq. (7.2). The result can be written in a simple form using the Moshinsky function [Kramer and Moshinsky, 2005] $M(k = -i\Gamma, t, z = 0)$, where

$$\begin{aligned} M(k, t, z) &= \int_{-\infty}^{0} dz' \frac{1}{\sqrt{2\pi i t}}\exp\left(ikz' + i\frac{(z - z')^2}{2t}\right) \\ &= \frac{1}{2}\exp\left(ikz - \frac{1}{2}k^2 t\mathrm{erfc}(e^{-i\pi/4}\frac{z - kt}{\sqrt{2t}})\right) \end{aligned} \tag{7.16}$$

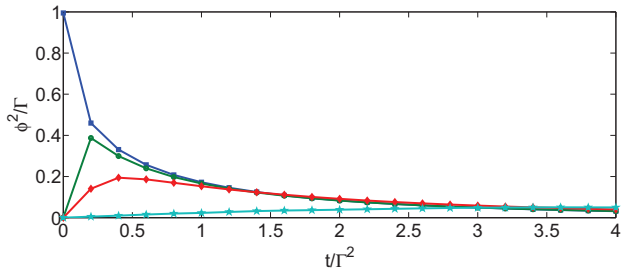

Figure 7.1: $|\tilde{\phi}(z_0,t)|^2$ with respect to time for $z_0 = 0$ (blue squares), $z_0 = 0.1/\Gamma$ (green circles), $z_0 = 1/\Gamma$ (red diamonds), $z_0 = 10/\Gamma$ (light blue stars). As the distance z_0 between the center of the cloud and the detector increases, the wave function spreads and long detector opening times are required to achieve non-trivial intensities. $\epsilon = 1$.

We thus get

$$\tilde{\phi}(z_0,t) = \sqrt{\Gamma}[M(-i\Gamma,t,z_0) + \frac{\epsilon}{2(2i\Gamma-\epsilon)}M(-i\Gamma,t,z_0) - \frac{\epsilon}{2(2i\Gamma+\epsilon)}M(-i\Gamma,t,-z_0) + \frac{2i\Gamma\epsilon}{4\Gamma^2+\epsilon^2}M(-\frac{\epsilon}{2},t,z_0) + \frac{\epsilon^2 e^{-\Gamma z_0}}{4\Gamma+\epsilon^2}M(-\frac{\epsilon}{2},t,0) - \frac{2i\epsilon e^{-\Gamma z_0}}{\sqrt{\Gamma}(4\Gamma^2+\epsilon^2)}M(-i\Gamma,t,0)]. \quad (7.17)$$

Using eq. (7.17), we can calculate the counting distribution $p(m)$ given in eq. (7.4). The counting statistics are determined by the time integral over the square of the wave function, $\tilde{\phi}^*(z_0,t)\tilde{\phi}(z_0,t)$. Fig. 7.1 shows the square of the wave function with respect to time for different distances z_0. As the distance increases, the wave function spreads in time. In order to obtain non-trivial results, long opening times are required.

7.2 Born Approximation

In the previous section, we solved the exact Lippmann-Schwinger equation (7.10). In this section, we use the Born approximation in order to derive an expression for $\tilde{\Psi}(z,t)$ in terms of the known propagator G_0. In the second order approximation, we obtain

$$G_S(z,z',t) = G_0(z,z',t) - i\frac{\epsilon}{2}\int_0^t dt' G_0(z,z_0,t-t')G_0(z_0,z',t'). \quad (7.18)$$

This implies that up to second order, the solution to eq. (7.2) is given by

$$\tilde{\Psi}(z,t) = \Psi(z,t) - i\frac{\epsilon}{2}\int_0^t dt' \int dz' G_0(z,z_0,t-t')G_0(z_0,z',t')\phi(z',t_0).$$
$$= \sqrt{\Gamma}(M(-i\Gamma,t,z_0) - \frac{\epsilon}{2}\int_0^t dt' \sqrt{\frac{1}{2\pi i t'}} M(-i\Gamma,t',z_0)) \quad (7.19)$$

Eq. (7.19) describes the evolution of the wave function, where the absorption at the detector is taken into account up to second order. In Sect. 7.3, we show that the second order approximation describes the situation more accurately than the Glauber-Mandel formula. However, the effect of the absorption is underestimated.

We get the higher order Born approximation by writing eq. (7.19) in exponential form,

$$\tilde{\phi}(\mathbf{z},t) = \sqrt{\Gamma} M(-i\Gamma,t,z_0) e^{-\epsilon/2 \int_0^t dt' \sqrt{\frac{m}{2\pi i t'}} M(-i\Gamma,t',z_0)/M(-i\Gamma,t,z_0)} \quad (7.20)$$

7.3 Comparison of the Approximate and Exact Solutions

Let us now analyze the effect of the back-action of the detector on the field. From eq. (7.4) it is clear that the important quantities to study are the square of the wave function, $\tilde{\phi}^*(z_0,t)\tilde{\phi}(z_0,t)$, its time integral, as well as the full counting distribution. We discuss the limits in which the Glauber-Mandel formula and the Born approximation give valid results, and study the limits of the approximative solutions.

In Fig. 7.2 a, we plot the square of the wave function with respect to time, and compare the exact solution to the solutions obtained by the born approximation and the Glauber-Mandel formula. We chose an exemplary value of $\epsilon = 0.5$. Note that the exact solution decays more rapidly, as the absorption at the detector is considered. The Born approximation underestimates the decay of the wave function and thus the absorption, however, it describes the behavior more accurately than the Glauber-Mandel formula, where absorption is not considered.

The effect is seen more clearly when studying the time integral $\int_0^\tau dt \tilde{\phi}^*(z_0,t)\tilde{\phi}(z_0,t)$. In Fig. 7.2 b, we plot the the integral with respect to the detection time τ. For

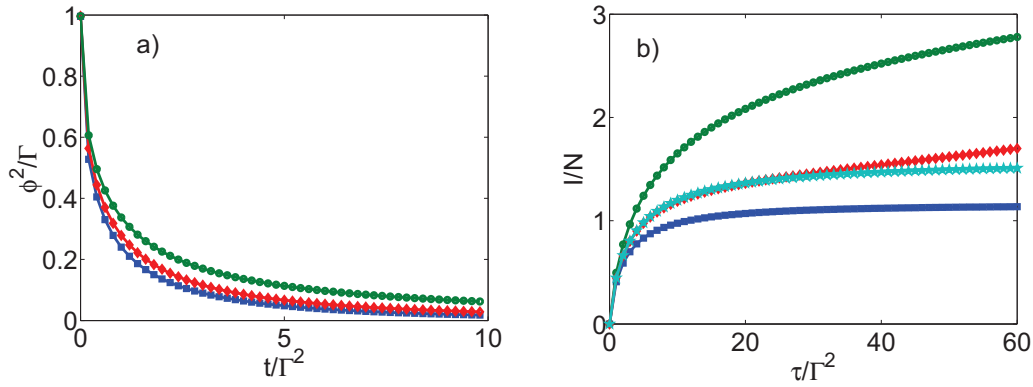

Figure 7.2: a) $|\phi(0,t)|^2$ with respect to t. b) $\int_0^\tau dt|\phi(0,t)|^2$ with respect to τ. We compare the exact solution (blue squares), Born approximation (red diamonds) and the Glauber-Mandel formula (green circles). Note that for long detection times, the exponential Born approximation (light blue stars) reaches an asymptotic value, whereas the second order approximation (red diamonds) diverges. $\epsilon = 0.5$

short detection times, the exact solution and the approximate solutions coincide. As the detection time increases, the intensity of particles is overestimated both for the Born approximation and for the Glauber-Mandel formula. Note that for long detection time, it is seen that second order Born approximation diverges, whereas the exponential Born approximation reaches an asymptotic value.

Finally, we compare the counting distributions obtained by the exact solution eq. (7.2) to the solution obtained by the Glauber-Mandel formula and the Born approximation. The effect of absorption is clearly visible in the counting distribution, where the approximate solutions deviate increasingly from the exact solution as the measurement time increases (Fig. 7.3). Let us note that the time is given in units of $m/(\hbar\Gamma^2)$. For a BEC with initial size of the order of $10\mu m$, the counting distributions in Fig. 7.3 correspond to timescales of the order of milliseconds. The effect of absorption at the detector can be estimated from Fig. 7.2 b, where the typical time scales of expanding BECs of around $20ms$ correspond to a value of around 5. The counting distribution calculated with the full formalism including detection is clearly different from the approximated solution.

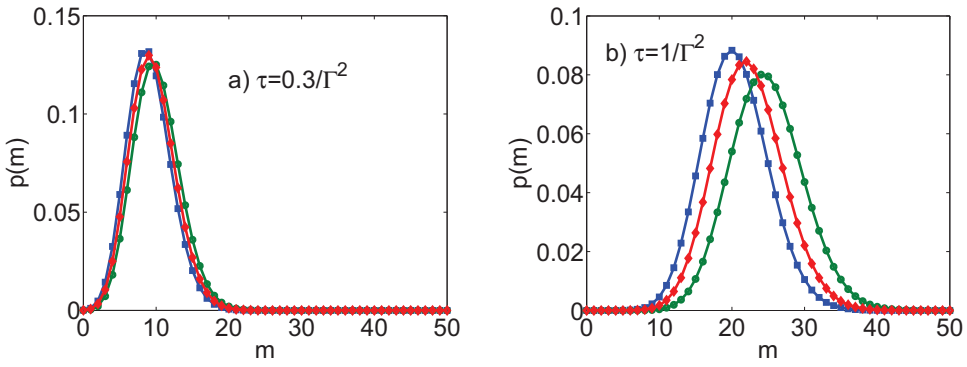

Figure 7.3: Counting distribution p(m) obtained from exact solution (blue squares), Born approximation (red diamonds) and the Glauber-Mandel formula (green circles). For short detection times (Fig. a) the approximations agree reasonably well with the exact solution. For longer detection times (Fig. b), the approximations are no longer valid. $z_0 = 0, \epsilon = 0.5$.

7.4 Summary

We have illustrated the effect of the back-action of the detector on the field for the free expansion of a Bose Einstein condensate. We showed that for typical experimental situations, the full time- and space dependent formalism has to be applied. An approximate solution using the Born approximation describes the behavior of the system more accurately than the Glauber-Mandel formula. However, for typical detection times of expanding BECs, the effect of absorption is under-estimated significantly both by the Glauber-Mandel formula, as well as the Born approximation.

Chapter 8

Conclusions and Outlook

We have explored the possibility of using many-body features of complex quantum systems for quantum technological applications. In particular, in analogy to classical neural networks, we focused on strongly correlated systems with a large number of metastable states to achieve robust storage and processing of information. Such complex quantum systems with many metastable states can be achieved with trapped ions or using atoms or molecules in optical lattices. Let us summarize our main findings:

The first part of the thesis shows that a quantum neural network model can be implemented with a system of trapped ions. The system allows for the processing of quantum information with high error resistance. The error resistance is achieved by distributing the information over the whole system.

The second part of the thesis addresses the scalability to larger systems and develops a formalism for the detection of many-body systems of atoms in optical lattices by particle counting. Our work is based on the formalism for photon counting, which has been used extensively since its development in the 1960s. We analyze the possibilities and limits of the formalism when applied to atoms in optical lattices. In particular, we have shown that particle counting allows for the detection of characteristic many-body features like quantum phase transitions and fermionic pair formation in strongly correlated systems. The formalism allows for the detection of the signatures of these effects at finite temperature. Furthermore, we have considered particle counting after a time of flight expansion for bosons that are released from an optical lattice. We have shown that

in the insulating regime, the occupation patterns of different metastable states can be distinguished from the counting distribution with detectors that are small compared to the expanded wave function. Likewise, supersolid states with different density distributions can be detected by particle counting after expansion from the lattice. The existing formalism for particle counting fails to describe experimental situations, in which the timescale of the system dynamics is comparable to the timescale of the counting process. We have derived a formula for the counting distribution of time- and space dependent fields, taking into account the back-action of the detector on the field. For the detection of an expanding condensate, the effect is visible at typical time-scales, such that the Glauber-Mandel formula does not fully describe the situation.

Making use of the many-body properties of complex quantum systems can result in advantages for quantum information processing. Based on our findings for quantum computing with ions, we are confident that further applications for quantum state engineering can be developed in complex quantum systems. In this context, dipolar atoms or molecules in optical lattices are promising candidates. The detection of such systems is of primary importance for the development of useful applications of quantum technologies. In order to use particle counting as a detection method, it would be of great interest to further study the effect of the back-action of the detector in time- and space dependent fields.

Bibliography

[Abramowitz and Stegun, 1965] Abramowitz, M. and Stegun, I. (1965). *Handbook of Mathematical Functions*. Dover, New York.

[Aharonov et al., 2007] Aharonov, D., van Dam, W., Kempe, J., Landau, Z., Lloyd, S., and Regev, O. (2007). Adiabatic quantum computation is equivalent to standard quantum computation. *SIAM Journal on Computing*, 37(1):166–194.

[Altman et al., 2004] Altman, E., Demler, E., and Lukin, M. D. (2004). Probing many-body states of ultracold atoms via noise correlations. *Phys. Rev. A*, 70(013603).

[Amit, 1989] Amit, D. (1989). *Modeling Brain Functions: The World of Attractor Neural Networks*. Cambridge University Press.

[Amit et al., 1985] Amit, D., Gutfreund, H., and Sompolinsky, H. (1985). Storing infinite number of patterns in a spin-glass model of neural networks. *Phys. Rev. Lett.*, 55:1530–1533.

[Anderlini et al., 2007] Anderlini, M., Lee, P., Brown, B. L., Sebby-Strabley, J., Phillips, W., and Porto, J. (2007). Controlled exchange interaction between pairs of neutral atoms in an optical lattice. *Nature*, 448(452).

[Arecchi et al., 1966] Arecchi, F. T., Berné, A., and Sona, A. (1966). Measurement of the time evolution of a radiation field by joint photocount distributions. *Phys. Rev. Lett*, 17(260-263).

[Auerbach, 1994] Auerbach, A. (1994). *Interacting Electrons and Quantum Magnetism*. Springer, New York.

[Bakr et al., 2009] Bakr, W. S., Jonathon, G. I., Peng, A., Fölling, S., and Greiner, M. (2009). A quantum gas microscope for detecting single atoms in a hubbard-regime optical lattice. *Nature*, 462:74–77.

[Bakr et al., 2010] Bakr, W. S., Peng, A., Tai, M. E., Ma, R., Simon, J., Gillen, J. I., Fölling, S., Pollet, L., and Greiner, M. (2010). Probing the superfluid-to-mott insulator transition at the single-atom level. *Science*, 329:547–550.

[Barouch and McCoy, 1971a] Barouch, E. and McCoy, B. (1971a). Statistical mechanics of the xy model ii. spin-correlation functions. *Phys. Rev. A*, 3(786).

[Barouch and McCoy, 1971b] Barouch, E. and McCoy, B. (1971b). Statistical mechanics of the xy model iii. *Phys. Rev. A*, 3(2137).

[Barouch et al., 1970] Barouch, E., McCoy, B., and Dresden, M. (1970). Statistical mechanics of the x-y model i. *Phys. Rev. A*, 2(1075).

[Batrouni and Scalettar, 2000] Batrouni, G. G. and Scalettar, R. T. (2000). Phase separation in supersolids. *Phys. Rev. Lett.*, 84:1599.

[Bañuls et al., 2010] Bañuls, M. C., Cirac, J. I., and Hastings, M. B. (2010). Strong and weak thermalization of infinite non-integrable quantum systems. *arXiv:1007.3957*.

[Berry, 1984] Berry, M. (1984). Quantal phase factors accompanying adiabatic changes. *Proc. R. Soc. Lond. A*, 84(392).

[Bloch, 2008] Bloch, I. (2008). Quantum coherence and entanglement with ultracold atoms in optical lattices. *Nature*, 453:1016–1022.

[Born and Fock, 1928] Born, M. and Fock, V. (1928). Beweis des adiabatensatzes. *Zeitschrift für Physik*, 51:165.

[Braungardt et al., 2011a] Braungardt, S., Rodríguez, M., Sen(De), A., Sen, U., Glauber, R. J., and Lewenstein, M. (2011a). Counting of fermions and spins in strongly correlated systems in and out of thermal equilibrium. *Phys. Rev. A*, 83:013601.

[Braungardt et al., 2011b] Braungardt, S., Rodríguez, M., Sen(De), A., Sen, U., and Lewenstein, M. (2011b). Atom counting in expanding ultracold clouds. *arXiv:1103.1868v1 [quant-ph]*.

[Braungardt et al., 2008] Braungardt, S., Sen, A., Sen, U., Glauber, R. J., and Lewenstein, M. (2008). Fermion and spin counting in strongly correlated systems. *Phys. Rev. A*, 78:063613.

[Braungardt et al., 2007] Braungardt, S., Sen, A., Sen, U., and Lewenstein, M. (2007). Noise-resistant distributed quantum computation in trapped ion chain. *Phys. Rev. A*, 76:042307.

[Breuer and Petruccione, 2002] Breuer, H. and Petruccione, F. (2002). *The Theory of Open Quantum Systems*. Oxford University Press, Oxford.

[Briegel et al., 2009] Briegel, H. J., Browne, D. E., Dür, W., Raussendorf, R., and Van den Nest, M. (2009). Measurement-based quantum computation. *Nature Phys.*, 5:19–26.

[Bronstein et al., 2002] Bronstein, I. N., Semendjajew, K. A., Musiol, G., and Muehlig, H. (2002). *Handbook of Mathematics*. Springer.

[Buluta and Nori, 2009] Buluta, I. and Nori, F. (2009). Quantum simulators. *Science*, 326:108–111.

[Cahill and Glauber, 1999] Cahill, K. and Glauber, R. (1999). Density operators for fermions. *Phys. Rev. A*, 59(1538).

[Campbell et al., 2006] Campbell, G. K., Mun, J., Boyd, M., Medley, P., Leanhardt, A. W., Marcassa, L. G., Pritchard, D. E., and Ketterle, W. (2006). Imaging the mott insulator shells by using atomic clock shifts. *Science*, 313(5787):649–652.

[Cheinet et al., 2008] Cheinet, P., Trotzky, S., Feld, M., Schnorrberger, U., Moreno-Cardoner, M., Fölling, S., and Bloch, I. (2008). Counting atoms using interaction blockade in an optical superlattice. *Phys. Rev. Lett.*, 101(090404).

[Cherng and Demler, 2007] Cherng, R. and Demler, E. (2007). Quantum noise analysis of spin systems realized with cold atoms. *New J. Phys.*, 9(7).

[Chiaverini and Lybarger, Jr., 2008] Chiaverini, J. and Lybarger, Jr., W. E. (2008). Laserless trapped-ion quantum simulations without spontaneous scattering using microtrap arrays. *Phys. Rev. A*, 77:022324.

[Chin et al., 2006] Chin, J., Miller, D., Liu, Y., Stan, C., Setiawan, W., Sanner, C., Xu, K., and Ketterle, W. (2006). Evidence for superfluidity of ultracold fermions in an optical lattice. *Nature*, 443(961).

[Chmara, 1987] Chmara, W. (1987). A quantum open-systems theory approach to photodetection. *J. Mod. Opt.*, 34(455-467).

[Cramer et al., 2008] Cramer, M., Flesch, A., McCulloch, I. P., Schollwöck, U., and Eisert, J. (2008). Exploring local quantum many-body relaxation by atoms in optical superlattices. *Phys. Rev. Lett.*, 101:063001.

[Deng et al., 2010] Deng, S., Ortiz, G., and Viola, L. (2010). Anomalous non-ergodic scaling in adiabatic multicritical quantum quenches. *Phys. Rev. B*, 80:241109.

[Deng et al., 2004] Deng, X.-L., Porras, D., and Cirac, J. (2004). Effective spin quantum phases in systems of trapped ions. *Phys. Rev. A*, 72(063407).

[Deutsch, 1985] Deutsch, D. (1985). Quantum theory, the church-turing principle and the universal quantum computer. *Proc. R. Soc. London A*, 400:97–117.

[Deutsch et al., 1995] Deutsch, D., Barenco, A., and Ekert, A. (1995). Universality in quantum computation. *Proc. R. Soc. London A*, 449(669).

[Deutsch and Jozsa, 1992] Deutsch, D. and Jozsa, R. (1992). Rapid solution of problems by quantum computation. *Proc. R. Soc. London A*, 439:553–558.

[Diehl et al., 2008] Diehl, S., Micheli, A., Kantian, A., Kraus, B., Büchler, H. P., and Zoller, P. (2008). Quantum states and phases in driven open quantum systems with cold atoms. *Nat. Phys.*, 4:878.

[DiVincenzo, 1995] DiVincenzo, D. P. (1995). Two-bit gates are universal for quantum computation. *Phys. Rev. A*, 51(1015-1022).

[Dodonov et al., 2007] Dodonov, A. V., Mizrahi, S. S., and Dodonov, V. V. (2007). Inclusion of nonidealities in the continuous photodetection. *Phys. Rev. A*, 75(013806).

[Dorner et al., 2003] Dorner, U., Fedichev, P., Jaksch, D., Lewenstein, M., and Zoller, P. (2003). Entangling strings of neutral atoms in 1d atomic pipeline structures. *Phys. Rev. Lett*, 91(073601).

[Dür et al., 2000] Dür, W., Vidal, G., and Cirac, J. I. (2000). Three qubits can be entangled in two inequivalent ways. *Phys. Rev. A*, 62:062314.

[Eckert et al., 2008] Eckert, K., Romero-Isart, O., Rodriguez, M., Lewenstein, M., Polzik, E., and Sanpera, A. (2008). Quantum non-demolition detection of strongly correlated systems. *Nature Physics*, 4(50-54).

[Eckert et al., 2007] Eckert, K., Zawitkowski, L., Sanpera, A., Lewenstein, M., and Polzik, E. S. (2007). Quantum polarization spectroscopy of ultracold spinor gases. *Phys. Rev. Lett.*, 98:100404.

[Ernst et al., 2010] Ernst, P. T., Götze, S., Krauser, J. S., Pyka, K., Lühmann, D.-S., Pfannkuche, D., and Sengstock, K. (2010). Probing superfluids in optical lattices by momentum-resolved bragg spectroscopy. *Nature Phys.*, 6:56–61.

[Farhi et al., 2000] Farhi, E., Goldstone, J., Gutmann, S., and Sipser, M. (2000). Quantum computation by adiabatic evolution. quant-ph/0001106.

[Farhi and Gutmann, 1998] Farhi, E. and Gutmann, S. (1998). Analog analogue of a digital quantum computation. *Phys. Rev. A*, 57(2403).

[Feynman, 1982] Feynman, R. (1982). Simulating physics with computers. *Int. J. Theor. Phys.*, 21:467–488.

[Fisher et al., 1989] Fisher, M., Weichman, P., Grinstein, G., and Fisher, D. (1989). Boson localization and the superfluid-insulator transition. *Phys. Rev. B*, 40:546.

[Fleischhauer and Welsch, 1991] Fleischhauer, M. and Welsch, D. G. (1991). Nonperturbative approach to multimode photodetection. *Phys. Rev. A*, 44(1):747–755.

[Fölling, 2008] Fölling, S. (2008). Probing strongly correlated states of ultracold atoms in optical lattices. *PhD Thesis, University of Mainz, Germany.*

[Friedenauer et al., 2008] Friedenauer, A., Schmitz, H., Glueckert, J. T., Porras, D., and Schaetz, T. (2008). Simulating a quantum magnet with trapped ions. *Nature Phys.*, 4:757–761.

[Gemelke et al., 2009] Gemelke, N., Zhang, X., Hung, C.-L., and Chin, C. (2009). In situ observation of incompressible mott-insulating domains in ultracold atomic gases. *Nature*, 460:995–998.

[Gericke et al., 2008] Gericke, T., Würtz, P., Reitz, D., Langen, T., and Ott, H. (2008). High-resolution scanning electron microscopy of an ultracold quantum gas. *Nature Phys.*, 4:949–953.

[Glauber, 1965] Glauber, R. J. (1965). Optical coherence and photon statistics. page 65, New York. Gordon & Breach.

[Gottesman, 1997] Gottesman, D. (1997). *Stabilizer Codes and Quantum Error Correction*. PhD thesis, California Institute of Technology, Pasadena, CA, U.S.A.

[Gradshteyn and Ryzhik, 2000] Gradshteyn, I. and Ryzhik, I. (2000). *Table of Integrals, Series, and Products*. Academic Press, San Diego.

[Góral et al., 2002] Góral, K., Santos, L., and Lewenstein, M. (2002). Quantum phases of dipolar bosons in optical lattices. *Phys. Rev. Lett.*, 88:170406.

[Greiner et al., 2002] Greiner, M., Mandel, O., Esslinger, T., Hänsch, T. W., and Bloch, I. (2002). Quantum phase transition from a superfluid to a Mott insulator in a gas of ultacold atoms. *Nature*, 415:39–44.

[Grover, 1997] Grover, L. (1997). Quantum mechanics helps in searching for a needle in a haystack. *Phys. Rev. Lett.*, 78:325–328.

[Hanbury-Brown and Twiss, 1956a] Hanbury-Brown, R. and Twiss, R. Q. (1956a). Correlation between photons in two coherent beams of light. *Nature*, 177:27–29.

[Hanbury-Brown and Twiss, 1956b] Hanbury-Brown, R. and Twiss, R. Q. (1956b). The question of correlation between photons in coherent light rays. *Nature*, 178:1447–1448.

[Hauke et al., 2010] Hauke, P., Cucchietti, F. M., Müller-Hermes, A., Bañuls, M.-C., Cirac, J. I., and Lewenstein, M. (2010). Complete devil's staircase and crystal-superfluid transitions in a dipolar xxz spin chain: a trapped ion quantum simulation. *New. J. Phys.*, 12(113037).

[Häyrynen et al., 2009] Häyrynen, T., Oksanen, J., and Tulkki, J. (2009). Exact theory for photon subtraction for fields from quantum to classical limit. *Eur. Phys. Lett.*, 78(44002).

[Häyrynen et al., 2010] Häyrynen, T., Oksanen, J., and Tulkki, J. (2010). Derivation of generalized quantum jump operators and comparison of the microscopic single photon detector models. *Eur. Phys. J. D*, 56:113–121.

[Hebb, 1949] Hebb, D. (1949). *The organization of behavior*. Wiley & Sons, New York.

[Häffner et al., 2008] Häffner, H., Roos, C. F., and Blatt, R. (2008). Quantum computing with trapped ions. *Physics Reports*, 469(4):155–203.

[Hopfield, 1982] Hopfield, J. (1982). Neural networks and physical systems with emergent collective computational abilities. *Proc. Natl. Acad. Sci. USA*, 79:2554–2558.

[Horodecki et al., 1999] Horodecki, M., Horodecki, P., and Horodecki, R. (1999). General teleportation channel, singlet fraction, and quasidistillation. *Phys. Rev. A*, 60(1888).

[Imoto et al., 1990] Imoto, N., Ueda, M., and Ogawa, T. (1990). Microscopic theory of continuous measurement of photon number. *Phys. Rev. A*, 41(7):4127–4129.

[Jaksch et al., 1998] Jaksch, D., Bruder, C., Cirac, J. I., Gardiner, C. W., and Zoller, P. (1998). Cold bosonic atoms in optical lattices. *Phys. Rev. Lett*, 81(3108-3111).

[James, 1998] James, D. (1998). Quantum dynamics of cold trapped ions with application to quantum computation. *Appl. Phys. B*, 66:181–190.

[Jeltes et al., 2007] Jeltes, T., McNamara, J. M., Hogervorst, W., Vassen, W., Krachmalnicoff, V., Schellekens, M., Perrin, A., Chang, H., Boiron, D., Aspect, A., and Westbrook, C. I. (2007). Comparison of the hanbury brown-twiss effect for bosons and fermions. *Nature*, 445:402–405.

[Jordan and Wigner, 1928] Jordan, P. and Wigner, E. (1928). Über das paulische Äquivalenzverbot. *Z. Phys.*, 47(631).

[Jördens et al., 2008] Jördens, R., Strohmaier, N., Günter, K., Moritz, H., and Esslinger, T. (2008). A mott insulator of fermionic atoms in an optical lattice. *Nature*, 455(204).

[Julsgaard, 2003] Julsgaard, B. (2003). *Entanglement and Quantum Interactions with Macroscopic Gas Samples*. Phd thesis, Center for Quantum Optics, University of Aarhus, Denmark.

[Katsura, 1962] Katsura, S. (1962). Statistical mechanics of the anisotropic linear heisenberg model. *Phys. Rev.*, 127(1508).

[Kelley and Kleiner, 1964] Kelley, P. L. and Kleiner, W. H. (1964). Theory of electromagnetic field measurement and photoelectron counting. *Phys. Rev.*, 136(A316-A334).

[Kielpinski et al., 2002] Kielpinski, D., Monroe, C., and Wineland, D. J. (2002). Architecture for a large-scale ion-trap quantum computer. *Nature*, 417:709–711.

[Kitaev, 1997] Kitaev, A. (1997). Fault-tolerant quantum computation by anyons. quant-ph/9707021.

[Kleber, 1994] Kleber, M. (1994). Exact solutions for time-dependent phenomena in quantum mechanics. *Physics Reports*, 236:331–393.

[Kollath et al., 2006] Kollath, C., Iucci, A., McCulloch, I., and Giamarchi, T. (2006). Modulation spectroscopy with ultracold fermions in an optical lattice. *Phys. Rev. A*, 74(041604).

[Kovrizhin et al., 2005] Kovrizhin, D. L., Pai, G. V., and Sinha, S. (2005). Density wave and supersolid phases of correlated bosons in an optical lattice. *Europhys. Lett.*, 72:162.

[Kramer et al., 2002] Kramer, T., Bracher, C., and Kleber, M. (2002). Matter waves from quantum sources in a force field. *J. Phys A*, 35(8361).

[Kramer and Moshinsky, 2005] Kramer, T. and Moshinsky, M. (2005). Tunnelling out of a time-dependent well. *J. Phys. A*, 38:5993–6003.

[Kraus et al., 2008] Kraus, B., Büchler, H. P., Diehl, S., Kantian, A., Micheli, A., and Zoller, P. (2008). Preparation of entangled states by quantum markov processes. *Phys. Rev. A*, 78:042307.

[Krauth et al., 1992] Krauth, W., Caffarel, M., and Bouchard, J.-P. (1992). Gutzwiller wave function for a model of strongly interacting bosons. *Phys. Rev. B*, 45(3137).

[Lahaye et al., 2009] Lahaye, T., Menotti, C., Santos, L., Lewenstein, M., and Pfau, T. (2009). The physics of dipolar bosonic quantum gases. *Rep. Prog. Phys.*, 72:126401.

[Leggett, 2006] Leggett, A. J. (2006). *Quantum Liquids*. Oxford University Press, New York.

[Lewenstein, 2007] Lewenstein, M. (2007). Atomic physics: The social life of atoms. *Nature*, 445:372–375.

[Lewenstein et al., 2007] Lewenstein, M., Sanpera, A., Ahufinger, V., Damski, B., Sen(De), A., and Sen, U. (2007). Ultracold atomic gases in optical lattices: Mimicking condensed matter physics and beyond. *Adv. in Phys.*, 56(243).

[Lewenstein et al., 2004] Lewenstein, M., Santos, L., Baranov, M., and Fehrmann, H. (2004). Atomic bose-fermi mixtures in an optical lattice. *Phys. Rev. Lett.*, 92(050401).

[Mandel, 1958] Mandel, L. (1958). Fluctuations of photon beams and their correlations. *Proc. Phys. Soc (London)*, 72:1037.

[Mandel, 1959] Mandel, L. (1959). Fluctuations of photon beams - the distribution of the photo electrons. *Proc. Phys. Soc (London)*, 74:233.

[Mandel, 1963] Mandel, L. (1963). Fluctuations of light beams. *in: Progress in Optics*, page 181. ed. E. Wolf (North-Holland, Amsterdam).

[Mandel, 1981] Mandel, L. (1981). Comment on 'photon counting probabilities in quantum optics'. *Opt. Acta*, 28:1447–1450.

[Mandel et al., 1964] Mandel, L., Sudarshan, E. C. G., and Wolf, E. (1964). Theory of photoelectric detection of light fluctuations. *Proc. Phys. Soc (London)*, 84:435.

[Mandel and Wolf, 1995] Mandel, L. and Wolf, E. (1995). *Optical Coherence and quantum optics*. Cambridge University Press, Cambridge.

[Manmana et al., 2007] Manmana, S. R., Wessel, S., Noack, R. M., and Muramatsu, A. (2007). Strongly correlated fermions after a quantum quench. *Phys. Rev. Lett.*, 98:210405.

[Menotti et al., 2007] Menotti, C., Trefzger, C., and Lewenstein, M. (2007). Metastable states of a gas of dipolar bosons in a 2d optical lattice. *Phys. Rev. Lett.*, 98:235301.

[Messiah, 1958] Messiah, A. (1958). *Quantum Mechanics*. John Wiley & Sons, New York.

[Micheli et al., 2006] Micheli, A., Brennen, G. K., and Zoller, P. (2006). A toolbox for lattice-spinmodels with polar molecules. *Nature Phys.*, 2:341–347.

[Mintert and Wunderlich, 2001] Mintert, F. and Wunderlich, C. (2001). Ion-trap quantum logic using long-wavelength radiation. *Phys. Rev. Lett.*, 87(25).

[Mollow, 1968] Mollow, B. R. (1968). Quantum theory of field attenuation. *Phys. Rev.*, 168(1896).

[Moritz, 2010] Moritz, H. (2010). Atomic superfluids see the light. *Nature*, 6:10–1.

[Osterloh et al., 2002] Osterloh, A., Amico, L., Falci, G., and Fazio, R. (2002). Scaling of entanglement close to a quantum phase transition. *Nature*, 416:608–610.

[Öttl et al., 2005] Öttl, A., Ritter, S., Köhl, M., and Esslinger, T. (2005). Correlations and counting statistics of an atom laser. *Phys. Rev. Lett.*, 95(090404).

[Pancharatnam, 1956] Pancharatnam, S. (1956). Generalized theory of interference, and its applications. part i. coherent pencils. *Proc. Indian Acad. Sci.*, 44(247).

[Parigi et al., 2007] Parigi, V., Zavatta, A., Kim, M., and Bellini, M. (2007). Probing quantum commutation rules by addition and subtraction of single photons to/from a light field. *Science*, 317(1890-1893).

[Pereira Dos Santos et al., 2001] Pereira Dos Santos, F., Léonard, J., Wang, J., Barrelet, C. J., Perales, F., Rasel, E., Unnikrishnan, C. S., Leduc, M., and Cohen-Tannoudji, C. (2001). Bose-einstein condensation of metastable helium. *Phys. Rev. Lett.*, 86:3459–3462.

[Pfeuty, 1970] Pfeuty, P. (1970). The one-dimensional ising model with a transverse field. *Ann. Phys. (N.Y.)*, 57(79).

[Plenio and Virmani, 2007] Plenio, M. and Virmani, S. (2007). Spin chains and channels with memory. *Phys. Rev. Lett.*, 99:120504.

[Pons et al., 2007] Pons, M., Ahufinger, V., Wunderlich, C., Sanpera, A., Braungardt, S., Sen, A., Sen, U., and Lewenstein, M. (2007). Trapped ion chain as a neural network: Fault-tolerant quantum computation. *Phys. Rev. Lett.*, 98:023003.

[Porras and Cirac, 2004a] Porras, D. and Cirac, J. (2004a). Bose-einstein condensation and strong-correlation behaviour of phonons in ion traps. *Phys. Rev. Lett.*, 93(263602).

[Porras and Cirac, 2004b] Porras, D. and Cirac, J. (2004b). Effective quantum spin systems with trapped ions. *Phys. Rev. Lett.*, 92(207901).

[Rey et al., 2005] Rey, A. M., Blair Blakie, P., Pupillo, G., Williams, C. J., and Clark, C. W. (2005). Bragg spectroscopy of ultracold atoms loaded in an optical lattice. *Phys. Rev. A*, 72(023407).

[Rom et al., 2006] Rom, T., Best, T., van Oosten, D., Schneider, U., Fölling, S., Paredes, B., and Bloch, I. (2006). Free fermion antibunching in a degenerate atomic fermi gas released from an optical lattice. *Nature*, 444:733–736.

[Sachdev, 2001] Sachdev, S. (2001). *Quantum Phase Transitions*. Cambridge University Press, Cambridge.

[Schellekens et al., 2005] Schellekens, M., Hoppeler, R., Perrin, A., Gomes, J. V., Boiron, C., Aspect, A., and Westbrook, C. I. (2005). Hanbury brown twiss effect for ultracold quantum gases. *Science*, 310(5748):648–651.

[Schmied et al., 2009] Schmied, R., Wesenberg, J. H., and Leibfried, D. (2009). Optimal surface-electrode trap lattices for quantum simulation with trapped ions. *Phys. Rev. Lett.*, 102:233002.

[Schollwöck et al., 2004] Schollwöck, U., Richter, J., Farnell, D., and Bishop, R. (2004). Quantum magnetism. *Lecture Notes in Physics*, 645. Springer, Berlin.

[Scully and W. E. Lamb, 1969] Scully, M. O. and W. E. Lamb, J. (1969). Quantum theory of an optical maser. iii. theory of photoelectron counting statistics. *Phys. Rev.*, 179(368).

[Selloni et al., 1978] Selloni, A., Schwendimann, P., Quattropani, P., and Baltes, H. P. (1978). Open system theory of photodetection: dynamics of field and atomic moments. *J. Phys. A*, 11(1427).

[Sengupta et al., 2004] Sengupta, K., Powell, S., and Sachdev, S. (2004). Quench dynamics across quantum critical points. *Phys. Rev. A*, 69:053616.

[Sengupta et al., 2005] Sengupta, P., Pryadko, L. P., Alet, F., Troyer, M., and Schmid, G. (2005). Supersolids versus phase separation in two-dimensional lattice bosons. *Phys. Rev. Lett.*, 94:207202.

[Shapere and Wilczek, 1998] Shapere, A. and Wilczek, F. (1998). *Geometric Phases in Physics*. World Scientific, Singapore.

[Sherson et al., 2010] Sherson, J. F., Weitenberg, C., Endres, M., Cheneau, M., Bloch, I., and Kuhr, S. (2010). Single-atom-resolved fluorescence imaging of an atomic mott insulator. *Nature*, 467:68–72.

[Shor, 1996] Shor, P. (1996). Fault-tolerant quantum computation. *37th Symposium on Foundations of Computing, IEEE Computer Society Press*, pages 56–65.

[Shor, 1995] Shor, P. W. (1995). Scheme for reducing de- coherence in quantum computer memory. *Phys. Rev. A*, 52(4):R2493–R2496.

[Shor, 1997] Shor, P. W. (1997). Polynomial-time algorithms for prime factorization and discrete logarithms on a quantum computer. *SIAM Journal on Computing*, 26:1484–1509.

[Sørensen et al., 1998] Sørensen, J. L., Hald, J., and Polzik, E. S. (1998). Quantum noise of an atomic spin polarization measurement. *Phys. Rev. Lett.*, 80(3487).

[Srinivas and Davies, 1981] Srinivas, M. D. and Davies, E. B. (1981). Photon counting probabilities in quantum optics. *Opt. Acta*, 28:981–996.

[Srinivas and Davies, 1982] Srinivas, M. D. and Davies, E. B. (1982). What are the photon counting probabilities for open systems: A reply to mandel's comments. *Opt. Acta*, 29:235–238.

[Steane, 1996] Steane, A. M. (1996). Error correction codes in quantum theory. *Phys. Rev. Lett*, 77(5):793–797.

[Trefzger et al., 2008] Trefzger, C., Menotti, C., and Lewenstein, M. (2008). Ultracold dipolar gas in an optical lattice: The fate of metastable states. *Phys. Rev. A*, 78:043604.

[Trotzky et al., 2008] Trotzky, S., Cheinet, P., Fölling, S., Feld, M., Schnorrberger, U., Rey, A., Polkovnikov, A., Demler, E., Lukin, M., and Bloch, I. (2008). Time-resolved observation and control of superexchange interactions with ultracold atoms in optical lattices. *Science*, 319(295).

[Ueda et al., 1990] Ueda, M., Imoto, N., and Ogawa, T. (1990). Quantum theory for continuous photodetection processes. *Phys. Rev. A*, 41(7):3891–3904.

[van Dam et al., 2001] van Dam, W., Mosca, M., and Vazirani, U. (2001). How powerful is adiabatic quantum computation? *Proceedings of the 42nd Annual Symposium on Foundations of Computer Science*, 57:279–287. quant-ph/0206003.

[van Oosten et al., 2005] van Oosten, D., Dickerscheid, D. B. M., Farid, B., van der Straten, P., and Stoof, H. T. C. (2005). Inelastic light scattering from a mott insulator. *Phys. Rev. A*, 71(021601).

[Verstraete et al., 2009] Verstraete, F., Wolf, M. M., and Cirac, J. I. (2009). Quantum computation, quantum state engineering, and quantum phase transitions driven by dissipation. *Nat. Phys.*, 5:633.

[W. E. Lamb and Scully, 1969] W. E. Lamb, J. and Scully, M. O. (1969). The photoelectric effect without photons. *in: Polarization: Matiere et Rayonnement*, pages 363–369. Presses Universitaires de France, Paris.

[Wehr et al., 2006] Wehr, J., Niederberger, A., Sanchez-Palencia, L., and Lewenstein, M. (2006). Disorder versus the mermin-wagner-hohenberg effect: From classical spin systems to ultracold atomic gases. *Phys. Rev. B*, 74(224448).

[Wootters and Zurek, 1982] Wootters, W. K. and Zurek, W. H. (1982). A single quantum cannot be cloned. *Nature*, 299(5886):802–803.

[Wunderlich, 2002] Wunderlich, C. (2002). *in Laser Physics at the Limit*. Springer, Heidelberg. quant-ph/0111158.